PROCESSING AND MICROSTRUCTURAL CHARACTERIZATION OF ALUMINA-DISPERSED ZIRCONIA FIBERS

BY

SOO-MAN SIM

A DISSERTATION PRESENTED TO THE GRADUATE SCHOOL
OF THE UNIVERSITY OF FLORIDA IN
PARTIAL FULFILLMENT OF THE REQUIREMENTS
FOR THE DEGREE OF DOCTOR OF PHILOSOPHY

UNIVERSITY OF FLORIDA

1990

ACKNOWLEDGMENTS

I would like to express my sincere appreciation to Dr. D. E. Clark for his support, guidance and advice during the course of this work. I am also grateful to the members of my supervisory committee, Drs. J. M. Boncella, R. T. DeHoff, J. H. Simmons and E. D. Whitney for their helpful discussion and suggestions.

I would like to thank Mr. G. P. LaTorre for technical assistance with FT-IR and Dr. M. D. Sacks for the use of his experimental instruments. Special thanks go to Dr. A. Morrone for providing invaluable transmission electron micrographs. Appreciation is also extended to Ms. Foltz and Ms. Stapler for their help in editing this dissertation.

My deepest gratitude goes to my family, especially my wife and daughter for their sacrifice and understanding in supporting me throughout this study.

I would also like to acknowledge the financial support of the DARPA, Contract No. 972-B5-J-1006.

TABLE OF CONTENTS

	Page
ACKNOWLEDGMENT	ii
LIST OF TABLES	vi
LIST OF FIGURES	vii
ABSTRACT	viii
CHAPTERS	
I. INTRODUCTION	1
II. LITERATURE SURVEY	7
Introduction	7
Sol-Gel Processing of Oxide Fibers	9
Fabrication Process	9
Extrusion of Slips	16
Spinning of Viscous Solutions	17
Relic Process	21
Unidirectional Freezing of Gel	21
Chemical Behavior of Precursors	22
Inorganic Solutions of Metals	23
Alkoxide-Derived Sols	28
Rheology of Spinning Sols	33
Fiber Spinning	33
Shear Flow of Colloidal Dispersion	38
Spinnability	44
Rheological Behavior of Spinning Sols	50
Properties and Microstructures of Oxide Fibers	56
Zirconia-Yttria System	61
Polymorphism of Zirconia	61
Phase Equilibria in the Zirconia-Yttria System	64
Yttria-Stabilized Tetragonal Zirconia Polycrystals	67

Influence of Alumina Addition to Yttria-Stabilized Tetragonal Zirconia 68

III. RESEARCH OBJECTIVES AND ACCOMPLISHMENTS 72

IV. EXPERIMENTAL PROCEDURE 76

Starting Materials 76
Fiber Fabrication 79
Sol Preparation 79
Fiber Spinning 81
Heat Treatments 82
Characterization 83
Infrared Spectroscopy 83
Rheological Measurements 85
Thermal Analysis 86
Phase Identification and Crystallite Size Measurements 87
Electron Microscopy 89
Grain Size Measurements 90
Density Measurements 90

V. RESULTS AND DISCUSSION 92

Rheological Behavior of Zirconia-Based Sols 92
Concentration and Aging Effects 94
Effect of Alumina Content on Spinnability 100
Effect of Shear on Viscosity of Spinnable Sol 104
FT-IR Analysis of Zirconia-Based Sols and Fibers 112
Thermal Behavior of Zirconia in Y-TZP/Al_2O_3 Fibers 119
Thermal Analysis 119
Phase Analysis 127
Effect of Alumina on Growth of Zirconia Crystallites 131
Microstructural Characterization of Y-TZP/Al_2O_3 Fibers 138
Fiber Morphology 138
Coarsening of Alumina Particles in the Y-TZP Matrix 145
Effect of Alumina on Densification 160
Grain Growth of Zirconia on Y-TZP/Al_2O_3 Fiber Surfaces 165
Effect of Alumina Content on Grain Size of Zirconia 173
Effect of Alumina Inclusions on Grain Growth of Zirconia 178
High-Temperature Stability of Y-TZP/Al_2O_3 Fibers 188

VI. CONCLUSIONS 201

VII. SUGGESTIONS FOR FUTURE WORK 204

APPENDIX 206

A. SHEAR AND ELONGATIONAL FLOW BEHAVIORS 206

REFERENCES 217

BIOGRAPHICAL SKETCH 234

LIST OF TABLES

Table		Page
2.1	Commercially Prepared Ceramic Fibers	8
2.2	Sol-Gel Processes for Preparation of Oxide Fiber Preforms	12
2.3	Room-Temperature Mechanical Properties of Oxide Fibers	59
4.1	Characteristics of Zirconia Sol	77
4.2	Typical Analysis of Zirconia Sol	78
5.1	Infrared Peak Assignments for Zirconia Sol	114
5.2	Phases Present in Y-TZP and Y-TZP/Al_2O_3 Fibers	128
5.3	Phases Present in Y-TZP Fibers Containing 3 mol% Y_2O_3 and Various Amounts of Alumina	132
5.4	Chemical Analysis of Y-TZP/Al_2O_3 Fibers Containing 3 mol% Y_2O_3 and 15 wt% Al_2O_3	158
5.5	Average Zirconia Grain Size in Y-TZP and Y-TZP/Al_2O_3 Fibers	168
5.6	Activation Energies for Zirconia Systems	186

LIST OF FIGURES

Figure		Page
1.1	Current status of research activity and trend of commercialization of sol-gel technology	6
2.1	Schematic representation for the production of continuous and discontinuous fibers:(a) process for continuous fibers by extrusion and (b) process for discontinuous fibers by centrifugal spinning . . .	15
2.2	Structure of aluminum monoacetate: (a) possible aluminum monoacetate species and (b) hydrogen bonding interaction between aluminum species [Eve88]	25
2.3	Structural representation of zirconyl chloride, $ZrOCl_2.8H_2O$: (a) tetrameric zirconyl cation and (b) its hydrolysis and polymerization products [Clo85]	27
2.4	Schematic illustration of polymeric species and gel formation in (a) acid-catalyzed and (b) base-catalyzed TEOS sols [Bri85]	30
2.5	Schematic of continuous spinning process	34
2.6	Take-up force as a function of draw ratio, D_R, for a Newtonian liquid and a non-Newtonian liquid of almost equal viscosity	36
2.7	Reduced viscosity versus volume fraction for a dispersion of glass spheres in 65 μm diameter [Hie86]	40
2.8	Relative viscosity versus volume fraction for monodispersed latices . .	42
2.9	Thread length (x^*) as a function of the product of extrusion velocity and viscosity ($V\eta$). (a) Experimentally determined x^* for solutions of cellulose acetate in an acetone and water mixture. (b) Theoretically determined x^*	46
2.10	Schematic illustration of liquid thread breakup mechanisms. (a)	

Cohesive fracture of a steady-state liquid thread. (b) Capillary breakup of a steady-tate liquid thread [Zia67] 47

2.11 Viscosity as a function of shear rate for spinnable and non-spinnable TEOS sols. (a) Spinnable sol in an open system allowing evaporation of solvents. (b) Non-spinnable sol in a closed systems not allowing evaporation of solvents 53

2.12 Flow behavior of an acid-catalyzed TEOS sol hydrolyzed with a low water content at various aging times. (a) Shear stress versus shear rate. (b) Viscosity versus shear rate 54

2.13 Tensile strength (a) and elastic modulus (b) as function of temperature for oxide fibers [Pys89] 60

2.14 Crystal structures of three stable polymorphs of zirconia [Heu87] . . . 62

2.15 Phase diagram for the zirconia rich portion of the zirconia-yttria system [Sco75] 66

2.16 Strength as a function of temperature for TZP and TZP/Al_2O_3 composites [Tsu87] 69

4.1 Processing flow diagram for preparation of Y-TZP/Al_2O_3 fibers 80

4.2 Typical micrographs of (a) Y-TZP fibers containing 3 mol% Y_2O_3 drawn by centrifugal spinning and dired at room temperature and (b) Y-TZP/Al_2O_3 fibers containing 2 mol% Y_2O_3 and 10 wt% Al_2O_3 fired at 1200°C for 1 hour 84

5.1 Plot of viscosity versus reduced vol% of zirconia sols containing yttrium and aluminum nitrates 95

5.2 Plot of viscosity versus reduced vol% of zirconia sols with PVA 97

5.3 Plot of viscosity versus aging time for zirconia sols without PVA . . . 99

5.4 Plot of viscosity versus aging time for zirconia sols containing 2 wt% PVA 101

5.5 Plot of viscosity versus alumina content in zirconia sol containing yttrium nitrate (2 mol% Y_2O_3) and 2 wt% PVA 102

5.6 Plot of viscosity versus shear rate for zirconia sol without aluminum nitrate 105

5.7 Casson plot of shear stress versus shear rate for zirconia sol without aluminum nitrate 107

5.8 Plot of viscosity versus shear rate for zirconia sol containing aluminum nitrate 108

5.9 Plot of shear stress versus shear rate for zirconia sol containing aluminum nitrate 109

5.10 Casson plot of shear stress versus shear rate for zirconia sol containing aluminum nitrate 110

5.11 FT-IR spectra of zirconia sol stabilized with acetic acid 113

5.12 FT-IR spectra of zirconia sols and fibers containing yttrium nitrate (3 mol% Y_2O_3) and PVA (2 wt%). The spectra (a), (b) and (c) correspond to the sol without volume reduction, the sol with 60.8% of reduced volume, and the fibers dried at room temperature, respectively 116

5.13 FT-IR spectra of zirconia sols and fibers containing yttrium nitrate (3 mol% Y_2O_3), aluminum nitrate (10 wt% Al_2O_3) and PVA (2 wt%). The spectra (a), (b) and (c) correspond to the sol without volume reduction, the sol with 60.3% of reduced volume, and the fibers dried at room temperature, respectively 118

5.14 DSC and TGA curves of zirconia gel at a heating rate of 10°C/min in air 120

5.15 DTA and TGA curves of aluminum nitrate, $Al(NO_3)_3{\cdot}9H_2O$, at a heating rate of 5°C/min in air 122

5.16 DTA and TGA curves of (a) Z2Y gel containing yttrium nitrate (2 mol% Y_2O_3) and PVA (2 wt%) and (b) Z2Y16.7A gel containing yttrium nitrate (2 mol% Y_2O_3), aluminum nitrate (16.7 wt% Al_2O_3) and PVA (2 wt%) at a heating rate of 5°C/min in air 124

5.17 DTA and TGA curves of (a) Z3Y fibers containing yttrium nitrate (3 mol% Y_2O_3) and PVA (2 wt%) and (b) Z3Y15A fibers containing yttrium nitrate (3 mol% Y_2O_3), aluminum nitrate (15 wt% Al_2O_3) and PVA (2 wt%) at a heating rate of 5°C/min in air 126

5.18 X-ray diffraction patterns of Y-TZP/Al_2O_3 fibers (a) containing 2 mol% Y_2O_3 and 16.7 wt% Al_2O_3 (Z2Y16.7A) and (b) containing 3 mol% Y_2O_3 and 15 wt% Al_2O_3 (Z3Y15A) fired at 1400°C for 1 hour in air 130

5.19 Crystallite size of tetragonal zirconia in Y-TZP fibers containing 3 mol% Y_2O_3 and various amounts of alumina 133

5.20 Effect of alumina on intensities of X-ray diffraction patterns of Y-TZP/Al_2O_3 samples fired at 700°C 135

5.21 Temperature dependence of crystallite size of tetragonal zirconia in Y-TZP/Al_2O_3 fibers 136

5.22 Scanning electron micrographs of Y-TZP/Al_2O_3 fibers containing 2 mol% Y_2O_3 and 10 wt% Al_2O_3 fired at 1200°C showing (a) surface and (b) fracture surface 139

5.23 Scanning electron micrographs of Y-TZP/Al_2O_3 fibers containing 2 mol% Y_2O_3 and 10 wt% Al_2O_3 fired at 1400°C showing (a) surface and (b) fracture surface 140

5.24 Scanning electron micrographs of Y-TZP/Al_2O_3 fibers containing 2 mol% Y_2O_3 and 16.7 wt% Al_2O_3 fired at 1500°C showing (a) surface and (b) fracture surface 141

5.25 Scanning electron micrographs of Y-TZP fibers containing 2 mol% Y_2O_3 fired at 1500°C showing (a) surface and (b) fracture surface . . . 142

5.26 Polished surface (a) and EDS spectra (b) of bulk Y-TZP/Al_2O_3 sample containing 2 mol% Y_2O_3 and 16.7 wt% Al_2O_3 fired at 1500°C for 2 hours 144

5.27 Polished surfaces of Y-TZP/Al_2O_3 (3 mol% Y_2O_3 and 15 wt% Al_2O_3) fibers sintered at (a) 1200°C, (b) 1300°C, (c) 1400°C, and (d) 1500°C 146

5.28 Polished surface of Y-TZP/Al_2O_3 (3 mol% Y_2O_3 and 15 wt% Al_2O_3) fibers sintered at 1500°C, showing coalescence of elongated alumina particles 149

5.29 Transmission electron micrographs of Y-TZP/Al_2O_3 (3 mol% Y_2O_3 and 15 wt% Al_2O_3) fibers at 1200°C, showing (a) alumina particles embedded in the zirconia matrix, (b) faceted zirconia grains (dark

areas are zirconia grains and light areas are alumina particles), (c) a triple joint of zirconia and alumina having clean interfaces, and (d) EDS spectrum at the triple joint in (c) 150

5.30 Transmission electron micrographs of Y-TZP/Al_2O_3 (3 mol% Y_2O_3 and 15 wt% Al_2O_3) fibers at 1400°C, showing (a) faceted zirconia grains (b) pockets formed between zirconia grains 152

5.31 Transmission electron micrographs of Y-TZP/Al_2O_3 (3 mol% Y_2O_3 and 15 wt% Al_2O_3) fibers at 1500°C: (a) elongated alumina particles with an aspect ratio >3 (A, B, C, D, and E grains)(insets are microdiffraction patterns of tetragonal zirconia and α-Al_2O_3), (b) a pocket formed between zirconia grains, (c) a triple joint of zirconia and alumina showing thin, continuous intergranular amorphous phases formed after sintering for 2 hours), and (d) EDS spectrum of the pocket in (b) including matrix grains 153

5.32 Plot of relative density versus sintering temperature for Y-TZP and Y-TZP/Al_2O_3 fibers at a heating rate of 5°C/min and held for 1 hour 161

5.33 Polished surfaces of Y-TZP (3 mol% Y_2O_3) fibers sintered at (a) 1200°C and (b) 1400°C 163

5.34 Scanning electron micrographs of Y-TZP (3 mol% Y_2O_3) fibers sintered at (a) 1200°C, (b) 1300°C and (c) 1500°C 170

5.35 Scanning electron micrographs of Y-TZP/Al_2O_3 (3 mol% Y_2O_3 and 15 wt% Al_2O_3) fibers sintered at (a) 1200°C, (b) 1300°C and (c) 1500°C 171

5.36 Plot of zirconia grain size versus temperature for the Y-TZP and Y-TZP/Al_2O_3 fibers sintered for 1 hour 172

5.37 Plot of zirconia grain size versus alumina content in Y-TZP/Al_2O_3 fibers sintered at 1400° and 1500°C for 1 hour 174

5.38 Scanning electron micrographs of Y-TZP/Al_2O_3 fibers sintered at 1400°C for 1 hour containing (a) 0, (b) 5, (c) 10, and (d) 15 wt% Al_2O_3 176

5.39 Plot of zirconia grain size versus sintering time for Y-TZP (3 mol% Y_2O_3) fibers sintered at 1400° and 1500°C 179

5.40 Plot of zirconia grain size versus sintering time for Y-TZP/Al_2O_3 (3 mol% Y_2O_3 and 15 wt% Al_2O_3) fibers sintered at 1400° and 1500°C 180

5.41 Scanning electron micrographs of Y-TZP/Al_2O_3 (3 mol% Y_2O_3 and 15 wt% Al_2O_3) fibers sintered at 1500°C for (a) 0.1, (b) 0.5, (c) 1, and (d) 2 hours 181

5.42 Temperature dependence of growth of zirconia grain on surfaces of Y-TZP (3 mol% Y_2O_3) and Y-TZP/Al_2O_3 (3 mol% Y_2O_3 and 15 wt% Al_2O_3) fibers 185

5.43 X-ray diffraction patterns of (a) Y-TZP (3 mol% Y_2O_3) and (b) Y-TZP/Al_2O_3 (3 mol% Y_2O_3 and 15 wt% Al_2O_3) fibers after maintaining at 1400°C for 24 hours in air 190

5.44 X-ray diffraction patterns of (a) Y-TZP (3 mol% Y_2O_3) and (b) Y-TZP/Al_2O_3 (3 mol% Y_2O_3 and 15 wt% Al_2O_3) fibers after maintaining at 1500°C for 6 hours in air 191

5.45 Distribution of grain intercept size of zirconia in (a) Y-TZP (3 mol% Y_2O_3) and (b) Y-TZP/Al_2O_3 (3 mol% Y_2O_3 and 15 wt% Al_2O_3) fibers after maintaining at 1400°C for 24 hours in air 192

5.46 Distribution of grain intercept size of zirconia in (a) Y-TZP (3 mol% Y_2O_3) and (b) Y-TZP/Al_2O_3 (3 mol% Y_2O_3 and 15 wt% Al_2O_3) fibers after maintaining at 1500°C for 6 hours in air 193

5.47 Scanning electron micrographs of (a) Y-TZP (3 mol% Y_2O_3) and (b) Y-TZP/Al_2O_3 (3 mol% Y_2O_3 and 15 wt% Al_2O_3) fibers maintained at 1400°C for 24 hours in air 195

5.48 Scanning electron micrographs of (a) Y-TZP (3 mol% Y_2O_3) and (b) Y-TZP/Al_2O_3 (3 mol% Y_2O_3 and 15 wt% Al_2O_3) fibers maintained at 1500°C for 6 hours in air 196

5.49 Transmission electron micrographs of Y-TZP/Al_2O_3 fibers containing 3 mol% Y_2O_3 and 15 wt% Al_2O_3 after maintaining at 1500°C for 6 hours in air, showing (a) pockets formed between zirconia grains, and zirconia and alumina grains and (b) an intergranular film between zirconia and alumina grains 198

A.1 Schematic plots of shear stress τ versus shear rate $\dot{\gamma}$ for (a) Bingham body, (b) shear-thinning (pseudoplastic) fluid and (c)

shear-thickening (dilatant) fluid 208

A.2 Schematic illustration of shear stress τ versus shear rate $\dot{\gamma}$ for thixotropic behavior. (a) The curved arrow indicates the direction of increasing time that the sample has been recovering after a large shear rate was applied. (b) Hysteresis loops for Newtonian type (curve A) and non-Newtonian type (curve B) of thixotropy 210

A.3 Elongational viscosity (η_E) and shear viscosity (η) as a function of stress for the low-density polyethylene [Bar89] 213

A.4 The elongational flow and spinning behavior for branched and linear polyethylene. (a) The elongational viscosity versus tensile stress. (b) Illustration of the way in which tension-thickening liquids can be drawn without necking [Cog81] 216

Abstract of Dissertation Presented to the Graduate School
of the University of Florida in Partial Fulfillment of the
Requirements for the Degree of Doctor of Philosophy

PROCESSING AND MICROSTRUCTURAL CHARACTERIZATION
OF ALUMINA-DISPERSED ZIRCONIA FIBERS

By

SOO-MAN SIM

December, 1990

Chairman: David E. Clark
Major Department: Materials Science and Engineering

Ceramic fiber-reinforced composites are attracting considerable interest for use in high-temperature structural applications. However, applications are generally limited to temperatures below 1200°C due to degradation of the mechanical properties of the fibers, resulting from grain growth, creep and thermal instability. The objective of this research was to investigate processing variables affecting the fabrication of Al_2O_3-dispersed ZrO_2 fibers, which are potentially capable of withstanding high temperatures.

Variables affecting rheological properties of colloidal ZrO_2 sols containing yttrium and aluminum nitrates and poly(vinyl alcohol) were investigated by viscometry. Fourier transform infrared spectroscopy was used to characterize the sols.

Spinnability was obtained by adding the polymer which increases viscosity to a range of optimum values for spinning. Flow behavior of the sols progressively changed from Newtonian to shear-thinning with increasing sol concentration and exhibited spinnability.

Yttria-stabilized tetragonal ZrO_2 fibers with dispersed Al_2O_3 were prepared by centrifugal spinning. The effects of Al_2O_3 on the microstructure and the thermal stability of the fibers heat treated up to 1500°C were investigated by X-ray diffraction, thermal gravimetric/differential thermal analysis, scanning and transmission electron microscopy.

Fibers of fine-grained tetragonal ZrO_2 containing 15 wt% Al_2O_3 were obtained with >99% density. The distribution and shape of Al_2O_3 particles were determined by the thermal history of the fibers. The Al_2O_3 particles were uniformly distributed in the ZrO_2 matrix at low sintering temperatures (<1400°C). As sintering temperatures increased, the Al_2O_3 particles grew with the ZrO_2 grains and became elongated due to the presence of an intergranular liquid phase. Coarsening of Al_2O_3 diminished its retarding effect on grain growth of ZrO_2 on the fiber surfaces. The Al_2O_3 inclusions suppressed exaggerated grain growth (formation of large cubic ZrO_2 grains) on the surfaces at 1400° and 1500°C.

CHAPTER I
INTRODUCTION

The demand for high-temperature structural materials for use in devices such as gas turbine engines, supersonic vehicles and energy conversion systems has generated considerable interest in ceramic fibers. The use of ceramic parts in gas turbine engines has many advantages over conventional metal parts, such as higher operating temperatures, improved fuel efficiency, reduced weight and greater thrust-to-weight ratio. However, problems associated with ceramics include low fracture toughness, poor creep resistance and susceptibility to subcritical crack growth. These characteristics can lead to catastrophic failure of the ceramic parts. Such problems can be overcome by suitable fiber reinforcement which provides large increases in strength and, particularly, work of fracture (toughness) [Don76].

Applications of ceramic fiber-reinforced composites are generally limited to temperatures below 1200°C due to the degradation of fibers. In fact, there is no reinforcement material currently available for use above 1200°C. Commercially available ceramic fibers are SiC-, Al_2O_3- and mullite-based with tensile strengths ranging from 1 to 2 GPa. However, strengths of all these fibers decrease significantly above 1200°C. The high-temperature strengths of the SiC-based fibers deteriorate as a result of oxidation, internal void formation, and chemical and microstructural changes.

In an oxidizing atmosphere, the oxide fibers are more thermodynamically stable than the non-oxide fibers. However, their high-temperature strengths are limited by softening of an intergranular glassy phase and excessive grain growth [Mah87, Pys89]. Until recently, oxide fibers received less attention for use in ceramic-matrix composites due to their tendency to chemically bond to ceramic matrices. However, with the aid of fiber coatings to control interfacial properties, oxide fibers are receiving new interest [Ric84, Fitz86].

Successful composite performance requires fiber properties such as a high length/diameter ratio, high tensile strength and stiffness, low density (perhaps of these properties density is the least important from the point of view of high-temperature performance) and high refractoriness [DiC85]. More importantly, fibers should possess long-term thermal stability so that high strength is retained, allowing for extended use of the composites.

In order to prepare oxide fibers with the desired properties, the following approaches are suggested: (1) eliminate processing flaws such as internal voids and surface flaws, (2) eliminate amorphous grain boundary phases, and (3) disperse non-reactive, high-modulus, creep-resistant, second-phase materials which act as grain growth inhibitors.

Eliminating processing flaws depends on the fabrication process. Care should be taken not to introduce defects during fiber processing. Fiber failure can initiate from inhomogeneous inclusions, pores, large grains and grain boundaries. The

strength of continuous ceramic fibers is highly sensitive to both the population of flaws and the maximum flaw size.

Eliminating amorphous grain boundary phases requires high-purity fiber precursors and a clean processing environment. This precaution will help to avoid any contamination from sources other than the precursors.

Introducing grain growth inhibitors can be the most effective methods for improving high-temperature properties. A fine and uniformly dispersed second phase in a fine-grained matrix can inhibit the grain growth of the matrix phase and thus maintain this microstructure during sintering and service.

Zirconia ceramics are of great importance in many engineering applications. This is due to the ability of ZrO_2 to strengthen and toughen ceramics through the martensitic transformation of the tetragonal to monoclinic phase [Gul80, Dwo84, Garv84]. Among ZrO_2 ceramics, of particular interest is Y_2O_3-stabilized tetragonal ZrO_2 polycrystals (Y-TZP) exhibiting very high strength (1-1.2 GPa) and toughness (8-10 $MPam^{1/2}$) which can be attributed to a uniform and fine-grained microstructure containing almost 100% tetragonal phase. Nevertheless, their high-temperature properties are poor because of their fine-grain size and residual glassy phases at grain boundaries causing creep, and a loss of transformation toughening effect with increasing temperature. Attempts to improve the high-temperature strength have been made by Tsukuma and coworkers [Tsuk85, Tsu87], who used Al_2O_3 as a second phase inclusion. The strength of the Y-TZP/Al_2O_3 containing 2 mol% Y_2O_3 and 40 wt%

Al_2O_3 was reported to be 1 GPa at 1000°C, which is nearly four times higher than that of the Al_2O_3-free Y-TZP.

Zirconia fibers are potentially useful as reinforcement for composites. This is particularly true if the high-temperature strength and thermal stability can be improved using the suggested fiber fabrication approaches. The current use of ZrO_2 fibers is mainly for thermal insulation. Owing to the high refractoriness, chemical resistance and low thermal conductivity of ZrO_2, ZrO_2 fibers in the form of textiles, felts, boards and shaped articles provide highly efficient thermal protection in many applications requiring high operating temperatures and corrosive environments. They are useful in energy technology as diaphragm cells in electrolysis of brine and in water electrolysis for hydrogen production, as separators in NiH_2 batteries, and as protection membranes. Another possible application is as a thermal barrier placed beneath the core of a nuclear reactor in the event of a nuclear meltdown [Ste86].

Sol-gel processing is especially useful for preparing oxide fibers of Al_2O_3 and ZrO_2. These fibers can not be formed into fibers by the melt-spinning process because of their very high melting points and low melt viscosities. Sol-gel processing is a method for producing ceramics from solutions of metal-organic or inorganic compounds through a series of chemical reactions, gelation, drying and densification. Such a technology offers enormous opportunity for preparing crystalline ceramics and glasses with high purity, chemical homogeneity, and novel compositions and microstructures at relatively low temperatures. Applications for sol-gel materials include optical, electronic and structural ceramics [Uhl84], and recently discovered

ceramic superconductors in the form of fibers, thin films, coatings, powders and shaped monolithic parts [Bet88].

As indicated in Figure 1.1, ceramic fibers are among the most successful applications of sol-gel technology [Sow88a]. Other applications remain at the research and development level. Although sol-gel materials have been extensively investigated [Bet84, Bet86, Bet88, Ult84, Sci86, Ult88], there are still many technological barriers to be overcome. For example, large amounts of shrinkage during drying, resulting in cracking of monolithic parts, has made commercial production of large bodies very difficult [Zar82]. In fiber processing, most shrinkage occurs radially across the fiber and its dimensional change is not serious.

Advantages of the sol-gel processing of oxide fibers are [Mill84, Bir85] (1) fibers of highly refractory oxides can be prepared from chemical precursors at ambient temperatures and converted to final oxides at relatively low temperatures; (2) rheological properties can be adjusted to achieve fiber forming capability (spinnability); and (3) molecular or near-molecular scale of precursors provides better control of microstructure and composition.

Despite the high potential for fabricating ceramics provided by the sol-gel process, there is little information regarding the processing of oxide fibers. The chemistry and rheological behavior of sol-gels, physics of spinning, and microstructural evolution during heat treatments and at service temperatures must be investigated in depth.

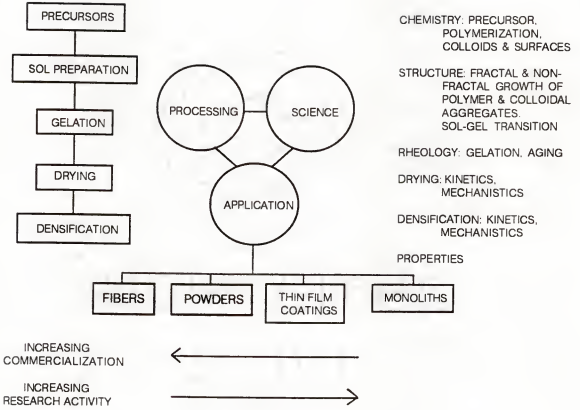

Figure 1.1. Current status of research activity and trend of commercialization of sol-gel technology.

CHAPTER II
LITERATURE SURVEY

Introduction

One of the earliest applications of the sol-gel process for preparing oxide fibers is the work by Wainer et al. [Wai65], who reported the preparation of ZrO_2 fibers by spinning a polymeric precursor followed by pyrolysis. Since then, there has been significant progress in developing and producing new oxide fibers. Recently, processing and properties of oxide fibers have been reviewed by many investigators [Bra84, Mill84, Bir85, Sow85, Fit88, Sow88a, Sta88]. However, most published literature contains only brief discussions of processing and focus on the physical properties of the final products due to the proprietary nature of work. More recently, many attempts have been made to prepare polycrystalline and glass fibers of various compositions using sol-gel technology [LaC88, Sak88, Sow88b].

Oxide fibers, commercially available and manufactured using the sol-gel process, are listed in Table 2.1. In general, ceramic fibers are based on Al_2O_3, mullite, ZrO_2 and SiC. Non-oxide fibers prepared by melt-spinning of polymers also are included. Avco silicon carbide fibers are prepared by chemical vapor deposition on carbon fibers.

TABLE 2.1

Commercially Prepared Ceramic Fibers*

Composition Type	Fiber Designation	Manufacturer	Form
Al_2O_3-B_2O_3-SiO_2	Nextel 312	3M	C+, D#
Al_2O_3-SiO_2 (2% B_2O_3)	Nextel 440		C, D
Mullite (2% B_2O_3)	Nextel 480		C, D
ZrO_2-SiO_2	Nextel Z-11		C, D
Al_2O_3	Fiber FP	du Pont	C
Al_2O_3-ZrO_2	PRD-166		C
Al_2O_3-SiO_2	Sumica	Sumitomo Chemical	C
Al_2O_3-SiO_2	Alcen	Denka Kagaku	D
Al_2O_3-SiO_2	Denka		C
Al_2O_3		Mitsui Mining	C
Al_2O_3-SiO_2	Saffil, Safimax	Imperial Chemical Industries	D
Al_2O_3-SiO_2	Fibermax	Carborundum	D
ZrO_2	Zircar	Union Carbide	D
SiC	Nicalon	Nippon Carbon	C
Si-Ti-C	Tyranno	Ube Industries	C
SiC	SCS-6	Avco	C
Si-C-N	MPDZ	Dow Corning/Celanese	C
Si-C-N	HPZ		C
SiC	MPS		C
Si_3N_4	Tonen	Tonen	C
C	Thornel 300	Union Carbide	C
	Celion GY-70	Celanese	C
	Torayca	Toray Industries	C
	Hercules	Hercules	C
	Hi-Tex	Hitco	C

* This table is not exhaustive; for example, it does not include glass fibers [Han84, Sow85, Hir87, Mah87, Fit88, Sta88].

+ Continuous fibers.

Discontinuous fibers.

Ceramic fibers in the form of roving, yarn, chopped, bulk, fabric or mat have two major applications; thermal insulation and reinforcement of plastics, metals and ceramics. In addition to applications for composites, the fibers are used in the heat shield of the space shuttle [Lei81], in flame shields, as furnace insulation and lining [Mill84], and in hot gas filtration. Ceramic filter bags are useful in high-temperature refinery operations for removal of particulates from the combustion processes [Sow88a]. A relatively recent application is in a ceramic fabric fire boom for collecting and burning oil spills on water [Sow88a]. Potential applications include monolithic supports in automobile catalytic converter, diesel engine exhaust particulate traps and acoustic insulation of aircraft engines [Bir85].

Sol-Gel Processing of Oxide Fibers

Fabrication Process

Sol-gel processing generally refers to the method which utilizes as precursors of sols either metal-organic compounds or inorganic salts to produce final oxide products through gelation, drying and densification at relatively low temperatures. Sol-gel processing is often called solution processing, because of the broad definition of the term "sol-gel."

In the first method, a polymerized alkoxide method, sols are prepared either by hydrolysis and condensation of metal alkoxides or by introducing modifier ions as soluble metal salts along with metal alkoxides as gel network formers. The second method, a colloidal sol method, uses a colloidal dispersion of hydrous oxides which

gels as a result of surface forces or hydrogen bonding. Sols can be prepared either by hydrolysis and peptization of metal alkoxides or by dispersing pre-existing colloidal particles in a liquid [John85].

The sol-gel process is associated typically with colloidal particles predominantly less than 0.1 μm in size, considerably smaller than the median size of particles in the usual ceramic slip or slurry. These sols usually are transparent or translucent and exhibit the Tyndall effect, which causes the transparent sol to appear bluish white and turbid when illuminated from the side against a dark background. The turbidity is due to scattering of the incident light by the tiny particles in the sol. [vanO77].

In the sol-gel processing of fibers, precursors may be sols or mixtures of sols and solutions. Inorganic solutions, sometimes modified with fugitive organics, and metal-organics such as alkoxides can be included in this broad category [Sow88a].

Processing of ceramic fibers consists of several steps which are controlled to meet specific criteria [Eve88]. In order to obtain fibers with the desired properties, in each step, the processing aspects such as chemistry of fiber precursors, rheological properties for fiber spinning, physics of spinning and microstructural changes during heat treatment should be taken into account.

The first step is preparation of the sol or a dilute mixture of precursors which is formulated to obtain a desired composition of fibers when calcined (heated). Precursors of inorganics such as metal salts, alkoxides and organometallics are dissolved in a suitable solvent, water or alcohol. Generally, additives are mixed in the

sols at this step. Polymers are added to control viscosity of the spinning mixture and to enhance spinnability of the sols. Other additives are often used as a second phase to control the microstructure of fibers.

The second step is thickening of the dilute sol, solution or mixture to a viscous state. One method of thickening is concentration of sols by evaporating the solvent under reduced pressure. Polymerized sol is thickened by aging at ambient or elevated temperature to increase viscosity. Under the right conditions, the mixture will become spinnable and contain no gel or precipitate. Rheological properties of the mixture are an important consideration in obtaining continuous or discontinuous fibers in the next step, the spinning process.

Three types of spinning processes were developed in late 1960s. The methods are extrusion of slips, spinning (centrifugal or extrusion) of viscous solutions and the relic process. Another method which is not commercially used is unidirectional freezing of gels. Continuous fibers are prepared by the extrusion of slips and spinning of viscous solutions methods. The spinning processes and types of precursors used for oxide fibers prepared commercially and experimentally are summarized in Table 2.2.

Continuous multifilaments are produced in a similar way to dry spinning of polymers in which molten polymers are extruded through a spinneret with a number of holes. The filaments are then drawn mechanically to a small diameter and passed through a drying column. During draw-down of the filaments at fluid state, the filaments become solid by evaporation of solvents. In sol-gel processing, viscous solutions and slips are used instead of molten polymers and ceramics. However, an

TABLE 2.2

Sol-Gel Processes for Preparation of Oxide Fiber Preforms

Spinning Method	Composition	Precursor	Reference
Extrusion of Slip	Al_2O_3	Aqueous Slurry Containing Spinning Additives	[Seu74]
Spinning of Viscous Solution	Al_2O_3	Colloidal Sol Derived from Aluminum Chloride	[Mak88]
	Al_2O_3-SiO_2	Solution of Aluminum Chloride, Organic Silicon Compound and Polymer	[Ray78] [Bir85]
	Al_2O_3-SiO_2	Polymer Solution of Organic Aluminum and Silicon Compounds	[Abe82]
	Al_2O_3-SiO_2 -B_2O_3	Solution of Aluminum Acetate, Colloidal SiO_2 and Spinning Additives	[Kar77]
	SiO_2	Polymerized Alkoxide Sol	[Sakk82] [LaC84]
	SiO_2-Al_2O_3, TiO_2, ZrO_2, and Na_2O	Polymerized Alkoxide Sol Mixture	[Kam80a] [Kam80b] [Sak88] [LaC88]
	SiO_2-TiO_2	Polytitanosiloxane Derived From Titanium Alkoxide and Silicic Acid	[Gun89]
	TiO_2	Polymerized Alkoxide Sol	[Lang79] [Kam86]
	ZrO_2	Solution of Zirconium Acetate, Metal Salt and Polymer	[Ler84] [Mar87] [Kha88]
	ZrO_2	Polymerized Alkoxide Sol	[Jad87]

TABLE 2.2 -- Continued.

Spinning Method	Composition	Precursor	Reference
Relic Process	ZrO_2	Solution of Zirconyl Chloride or Nitrate	[Ray78] [Yer84]
Unidirectional Freezing of Gel	Al_2O_3	Sol Derived From Aluminum Salt	[Mak86]
	SiO_2	Silicic Acid	[Mahl80]
	TiO_2	Sol Derived From Titanium Chloride	[Sak88]
	ZrO_2	Sol Derived From Zirconyl Chloride, Zirconyl Nitrate	[Kok83] [Mahl84] [Kok88]

additional heat treatment is required to convert sol-gel fibers to oxide forms. Figure 2.1 illustrates the processes for continuous and discontinuous fiber production. Centrifugal spinning is used for producing discontinuous fibers. In this technique, a solution is projected by centrifugal force from a small orifice or from a rapidly rotating disc. Short, staple glass fibers are produced by centrifugal spinning. The small cross-section and large surface area of sol-gel-derived fibers enables the volatiles to be eliminated rapidly and completely without damaging the filaments or producing voids. The solution spinning process is most versatile in that close control over compositions, rheology and hence fiber diameter is possible. The viscosity of a spinning solution is adjusted depending on the spinning processes.

The final step is to convert the spun fibers to oxide form by calcining and sintering. The conversion to oxide fibers is done usually by two-stage firing. The first stage serves to remove volatile materials from the fibers, while the second stage serves to densify the calcined fibers to yield dense, strong fibers with the desired microstructure. These steps can be done continuously or separately.

Whatever sol-gel processes and precursors are employed in fiber spinning, the post-spinning treatment is of great importance in determining the properties of the final fibers. Several aspects of heat treatment must be considered in order to successfully produce polycrystalline oxide fibers [Bir85]. First, the fiber must be dried without distortion, internal voids or bubble formation. This is necessary to produce dehydrated solid fibers capable of withstanding the handling involved in subsequent treatment. Second, further heating dehydrates hydrous phases and removes volatiles,

(a)

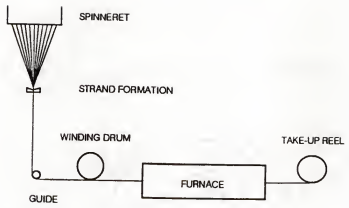

(b)

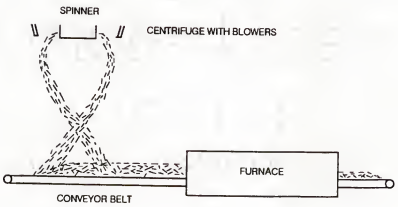

Figure 2.1. Schematic representation for the production of continuous and discontinuous fibers: (a) process for continuous fibers by extrusion and (b) process for discontinuous fibers by centrifugal spinning.

thus generating anhydrous oxide (calcining). In this stage, organics are burned out and crystallization of amorphous phases occurs. Finally, heating to higher temperatures should generate the desired final phase having appropriate crystallite size or grain size and completely removing of porosity (sintering).

After sintering, fibers may be coated with a polymer binder (referred to as sizing) such as poly(ethylacrylate) or poly(vinyl acetate) to facilitate handling and weaving. Additional coatings with other materials often are necessary to control interfacial properties such as interfacial bonding and wettability and to provide a diffusion barrier between fibers and matrix. A SiO_2 coating on Al_2O_3 fibers has been reported to enhance wetting and result in good bonding between the fiber and a metal matrix [Dhi80].

Extrusion of slips

The extrusion of slips is the process whereby a concentrated suspension of oxide particles is extruded through a spinneret to form continuous filaments. The suspension may contain dissolved organic polymers to aid suspension stability and to obtain appropriate rheological properties. The disadvantage in this process is that of excessive grain growth in the final oxide fibers due to relatively large oxide particle sizes typically found in slips. At the sintering temperature, recrystallization can occur resulting in a coarse texture and a weak fiber. To prevent this problem, additives such as grain growth inhibitors or phase stabilizers are included in the suspension. Fiber

diameters usually are large (≈20 μm) due to the larger particle sizes (>0.1 μm) used in this process as compared to the particle sizes in other processes.

Polycrystalline α-Al_2O_3 fibers, with and without a small amount of SiO_2 or other oxide, have been produced by this method [Seu74]. The spinning mixture is comprised of Al_2O_3 particles and an aqueous phase containing a dissolved Al_2O_3 precursor or a precursor which forms a solid solution with Al_2O_3. The most preferred Al_2O_3 precursors are the basic aluminum salts such as aluminum chlorohydroxide, basic aluminum nitrate and basic aluminum chloroacetate. To aid with spinnability, inorganic modifiers such as silicic acid and a high molecular weight poly(ethylene oxide) are added to the spinning mixture. Spinning mixtures containing high loadings of solid particles yield less volatility and fiber shrinkage on heating. One commercial fiber produced by this method is the FP fiber manufactured by du Pont and consisting of polycrystalline Al_2O_3 (>99% α-Al_2O_3) [Dhi80].

Spinning of Viscous Solutions

In the spinning process, a solution of inorganic compounds or alkoxides together with additives is concentrated to obtain a viscous spinning mixture. Soluble polymers such as poly(vinyl alcohol) or poly(ethylene oxide) often are added to increase the viscosities of the solutions and improve their spinning characteristics. Depending on the types of fibers desired, extrusion or centrifugal spinning is used to produce continuous or discontinuous fibers, respectively.

Transparent, flexible and continuous Nextel™[a] fibers are produced by spinning a viscous solution of a water-dispersible Al_2O_3 or a water-soluble organic aluminum salt and a SiO_2 sol. Alumina precursors may include aluminum formoacetate ($Al(OH)(OOCH)(OOCCH_3)$), aluminum nitrate ($Al(NO_3)_3{\cdot}9H_2O$), aluminum isopropylate ($Al(OC_3H_7)_3$), basic aluminum acetate ($Al(OH)_2(OOCH_3){\cdot}1/3H_3BO_3$), or a mixture of these. Using aluminum chloride has been found not to be beneficial since the presence of residual chloride (≈0.2 wt%) results in fragile fibers.

Silica precursors may be an aqueous colloidal SiO_2 sol or an organosol. An organosol is a colloidal dispersion of SiO_2 in such water miscible polar organic solvents as ethylene alcohol, dimethyformamide and various glycol ethers. Acetic or nitric acid is used to acidify the SiO_2 sol and prevent premature gelling. To improve shelf-life and spinnability of the concentrated mixture, an organic additive such as poly(vinylpyrrolidone), poly(vinyl alcohol), latic acid, or glucose (corn syrup), is added to the spinning mixture [Kar77].

Discontinuous Saffil®[b] fibers are produced by centrifugal spinning of a solution of aluminum oxychloride, 2 wt% of poly(vinyl alcohol) and a precursor of SiO_2 or CaO as a grain growth inhibitor. The resulting fibers are uniform in diameter (3 μm), flexible and have a silky texture. They have modest values of strength and elastic modulus [Ray78, Bir85].

---

[a]Nextel™ is a trademark of 3M Company.

[b]Saffil® is a registered trademark of Imperial Chemical Industries, Ltd.

Sumica[c] fibers are prepared in continuous filament forms by spinning a polymerized organo-aluminum compound and a silicon-containing compound [Abe82]. Trialkyl aluminum or trialkoxy aluminum is partially hydrolyzed to form aluminoxane. The polymerized solution of aluminoxane then is mixed with poly(vinyl alcohol) and an organosiloxane compound, such as alkylsilicate, and concentrated into a viscous spinning mixture.

Discontinuous ZrO_2 and MgO- or CeO_2-stabilized ZrO_2 fibers have been drawn by an air jet from a solution of zirconium acetate and magnesium acetate or cerium nitrate, which was concentrated by evaporation and aged so that polymerization progressed [Ler84]. A concentrated solution of zirconium acetate, a yttrium salt and a high molecular weight poly(ethylene oxide) have been used to produce continuous, fine grained tetragonal ZrO_2 fibers containing 3 mol% Y_2O_3 (Y-TZP) [Mar87, Kha88]. However, attempts to prepare ZrO_2 fibers by spinning of various solutions are still in experimental stages.

Recently, metal alkoxides have been used to prepare crystalline and amorphous fibers. But fabrication of the fibers is in an experimental stage and limited to SiO_2 fibers [Sakk82, LaC84] and SiO_2 fibers containing Al_2O_3 [Sak88], TiO_2 [Kam80a], ZrO_2 [Kam80b], and ZrO_2 and Na_2O [Kam80b]. The use of metal alkoxides has an advantage over that of salt solutions. The alkoxide solution itself, which has been hydrolyzed, polymerized or aged, can become viscous and spinnable

[c]Sumitomo Chemical Co., Ltd., Osaka, Japan.

without spinning additives. However, the composition of the starting solution must be chosen so that it can produce a spinnable sol.

Silica fibers have been prepared from a sol prepared by hydrolysis, condensation and aging after adding alcoholic solutions of H_2O and HCl to tetraethylorthosilicate (TEOS), $Si(OC_2H_5)_4$ [Sakk82]. When the composition of the starting solution was appropriate, fibers could be drawn from the viscous solution near room temperature. It has been claimed that a maximum heat-treatment temperature is much lower than that required for the fibers drawn from a sol-gel-derived bulk glass rod. The fibers drawn from an alkoxide solution can be converted to oxide fibers at 800°C.

The preparation of TiO_2 fibers from alkoxides is difficult due to the fast rates of hydrolysis and condensation reactions leading to immediate precipitation of hydroxide. An attempt has been made to use a complex titanium alkoxide, titanium acetylacetonate ($Ti(C_5H_7O_2)_2(OC_3H_7)_2$), which is stable in alcohol-water solutions [LaCo86]. Another approach has been made to prepare continuous TiO_2 fibers from an aqueous colloidal sol, obtained by dispersing dry gel granules [Lang79]. The gel was prepared by hydrolysis of titanium isopropoxide ($Ti(OC_3H_7^i)_4$) with HCl.

The same difficulty in preparing homogeneous and stable sols with titanium alkoxides is encountered with zirconium alkoxides. However, ZrO_2 fibers have been prepared from zirconium n-propoxide ($Zr(OC_3H_7^n)_4$) [Jad87]. Discontinuous fibers containing 6 wt% CaO could be drawn from a concentrated solution prepared by hydrolysis and condensation of zirconium n-propoxide using a hot air jet. Details of

the procedure have not been reported. Zirconium acetylacetonate also has been used to avoid the problems of inhomogeneity and instability [LaC88].

Relic Process

In the relic process, a support of organic form is impregnated with an inorganic solution, dried and then calcined to produce a relic of the original fiber or cloth. The support typically is made using an organic filament, yarn or woven cloth of wool, cotton or cellulose acetate rayon. The organic support fiber may be treated with amine or with dimethylsulfoxide to cause it to swell and become more absorbent. A wide range of textiles can be obtained in the forms of monofilaments, rigid boards and complex shapes. The fibers are porous and have a hollow center, resulting in poor mechanical properties. However, the fibers provide excellent thermal insulation.

Zircar[®d] fibers are manufactured using an aqueous solution of zirconyl chloride and yttrium chloride [Ray78]. A similar method has been used to prepare ZrO_2 fibers by oxidizing hydrated cellulose fibers which had been impregnated with a solution of zirconyl nitrate or chloride [Yer84].

Unidirectional Freezing of Gel

Unidirectional freezing of gels was first applied by Mahler and Bechtold [Mahl80] who prepared SiO_2 fibers from silicic acid. Fibers of ZrO_2 [Kok83, Mahl84, Kok88], TiO_2 [Sak88] and Al_2O_3 [Mak86] have been prepared similarly.

---

[d]Zircar® is a registered trademark of Zircar Products Inc.

Gels are prepared in cellulose tubes by dialysis or by polymerization and aging of sols. The gel is unidirectionally frozen by slowly immersing a cylinder containing the gel in a cold medium from the bottom of the cylinder. Directional freezing causes phase separation in the gel to occur and leads to cellular growth of ice and the gel. This process has same similarities to that used for directional solidification of an eutectic alloy. Upon thawing the frozen cylinder at room temperature, the gels are separated as a bundle of fibers and have polygonal cross-sections because of hexagonal shaped ice crystals. Fiber diameters can be controlled by adjusting both the freezing rate and the temperature gradient. However, this process is slow due to the slow freezing rate and produces discontinuous fibers with relatively large diameters.

Chemical Behavior of Precursors

There is little literature available that relates chemical behavior of precursors directly to fiber processing requirements. However, both Al_2O_3 and SiO_2 precursors are fairly well-studied and documented. Alumina precursors were investigated due to the early interest in Al_2O_3 fibers. The chemical behavior of alkoxides, especially silicon alkoxides, was extensively studied as interest in sol-gel processing has grown.

In general, the preparation of spinning sols involves hydrolysis and condensation reactions of precursor species to final oxides. During concentration and aging, the species are polymerized and eventually form polymeric networks or colloidal particles. For fiber spinning, intermediate species (linear polymers) are desired since the continuous polymeric phases are likely capable of withstanding

drawing stresses and provide fiber handling strength before and throughout all heat treatment stages [Sakk82, Bir83, LaC88].

Inorganic Solutions of Metals

A solution of aluminum oxychloride ($Al_2(OH)_5Cl$) is used as a precursor for Saffil® fibers. The solution is prepared by dissolution of aluminum metal in an aluminum chloride solution, followed by hydrolysis with sodium carbonate. At an OH/Al ratio of 3, $Al(OH)_3$ is formed and precipitated, but at ratios below this polymeric species of $[Al(H_2O)_6]^{3+}$ are formed. As the hydrolysis reaction proceeds, the hydrated species eliminate water to link octahedral units of the polymeric species by Al-OH-Al and Al-O-Al bridges. The continuation of such a process allows corners and edges of the octahedra to link up to form polymeric networks. The formula $Al_2(OH)_5Cl$ does not correspond to a stoichiometric compound, but to complex polymeric species such as $[AlO_4Al_{12}(OH)_{24}(H_2O)_{12}]^{7+}$ and $[AlO_4Al_{12}(OH)_{25}(H_2O)_{11}]^{6+}$ [Bir83].

Another Al_2O_3 precursor is an aluminum acetate solution used in preparing Nextel™ fibers [Kar77]. Aluminum triacetate ($Al(C_2H_3O_2)_3$) cannot be used because it is insoluble in water. Water-soluble aluminum monoacetate ($Al(C_2H_3O_2)(OH)_2$) is preferred in fiber spinning. Aluminum monoacetate is prepared by dissolution of aluminum powder in an acetic acid solution. Boric acid is used to prevent the formation of water-insoluble aluminum diacetate ($Al(C_2H_3O_2)_2(OH)$) and stabilize the formation of aluminum monoacetate [Eve88]. However, boric acid leads to a

significant decrease in fiber strength at high temperatures due to the presence of low-melting point glasses formed with B_2O_3. Lactic acid and dimethylformamide (DMF) are used to enhance the stabilizing effect during concentration of the solution. Lactic acid allows the thickening process to produce a fiberizable fluid without causing gelation, whereas DMF aids the formation of aluminum monoacetate [Eve88]. As the solution is concentrated, aluminum monoacetates link together by hydrogen bonding, which is weak but may include multiple interaction between adjacent complexes. The fiberization can be attributed to the hydrogen bonding. Figure 2.2 shows the structures of possible aluminum monoacetate species and the hydrogen bonding between the complexes.

Solutions of zirconyl chloride and zirconium acetate are common precursors for ZrO_2 fibers. Hydrolysis and condensation reactions of zirconium compounds differ from those of silicon and aluminum compounds. Zirconium hydroxides are compounds in which a number of hydroxyl groups are bound to a single zirconium atom. The negative charge of the hydroxyl group tends to pass to the zirconium atom, causing it to repel other hydroxyl groups or to relieve the repulsion by passing a proton from one of the hydroxyl groups to the oxygen atom of the neighboring hydroxyl group, resulting in the formation of oxo and aquo groups (formation of hydrated or hydroxylated zirconium oxides) [Blu58].

Zirconyl chloride solution is used as a precursor for Zircar® fibers. Hydrated zirconyl chloride ($ZrOCl_2 \cdot 8H_2O$) has a well-defined crystal structure [Cle56]. The cation in the solid is a dihydroxyl bridged tetramer with additional water ligands.

(a)

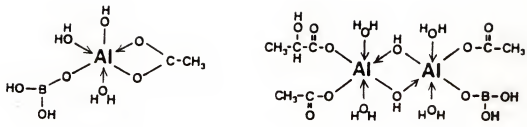

(b)

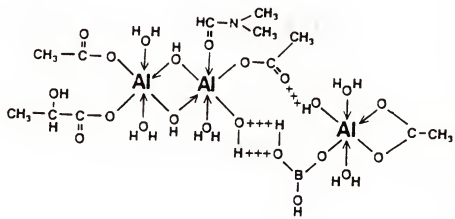

Figure 2.2. Structure of aluminum monoacetate: (a) possible aluminum monoacetate species and (b) hydrogen bonding interaction between aluminum species [Eve88].

There is no actual bond between zirconium and chloride ions. The composition of the tetrameric complex in the unit cell was found to be $[Zr_4(OH)_8(H_2O)_{16}]^{8+}$. On dissolution in water, the tetrameric unit is retained and hydrolysis occurs. One water ligand on each zirconium atom loses a proton to form a hydroxyl group as follows [Rij70]:

$$[Zr_4(OH)_8(H_2O)_{16}]^{8+} + 4H_2O \rightarrow [Zr_4(OH)_8(OH)_4(H_2O)_{12}]^{4+} + 4H_3O^+, \text{ and} \quad (2.1)$$

$$[Zr_4(OH)_8(OH)_4(H_2O)_{12}]^{4+} + H_2O \leftrightarrow [Zr_4(OH)_8(OH)_5(H_2O)_{11}]^{3+} + H_3O^+ \quad (2.2)$$

Depending on the acid concentration, the charge of the tetrameric complex 4+ can be reduced to 3+ in a second hydrolysis step. A polymerized solution consists of species in which the tetrameric complexes are connected by bridging OH ligands between zirconium ions. Figure 2.3 illustrates the structure of the tetrameric zirconyl cation and its polymerization products. Norman and Jones [Nor78] have reported a change in the viscosity of a solution of polyacrylamide (average molecular weight 110,000) with addition of zirconyl chloride solutions. An increase in viscosity was attributed to the interaction between cationic zirconium species and residual carboxyl groups (-COOH, 0.5-2 mole%) in the organic polymer. The more highly polymerized zirconium species produced, the greater the increase in sol viscosity.

Zirconium acetate solutions can be formed from zirconyl chloride solutions of moderate concentration by reacting them with acetic acid [Blu58]. Upon contact with an acetate ion (CH_3COO^-), the basic zirconyl cation ($[ZrOOH]^+$) in the solution

(a)

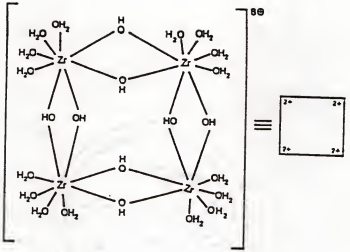

(b)

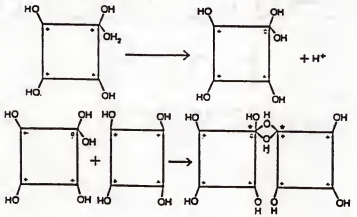

Figure 2.3. Structural representation of zirconyl chloride, $ZrOCl_2.8H_2O$: (a) tetrameric zirconyl cation and (b) its hydrolysis and polymerization products [Clo85].

combines to form a basic zirconyl monoacetate complex, $ZrO(OH)(C_2H_3O_2)\cdot nH_2O$. Further reaction of the complex with an acetate ion causes the complex to become a more stable and water-soluble zirconyl diacetate complex, $[ZrO(OH)(C_2H_3O_2)_2\cdot 2H_2O]^{\cdot}$. A bond between an acetate ion and a zirconium atom is more stable than a bond between an aquo group and a zirconium atom. Because of the large number of oxygen atoms in a molecule of zirconyl diacetate complex, it is expected to have a strong tendency to polymerize. When the solution is evaporated, its viscosity progressively increases until it sets to an amorphous solid [Blu58].

Alkoxide-Derived Sols

Tetraethylorthosilicate (TEOS or $Si(OC_2H_5)_4$) is especially useful in fiber spinning because the structure of species in the sol allows spinnability without spinning additives. However, this is true only if the sol is prepared under specific conditions. The major reactions in preparing sols from TEOS are hydrolysis and condensation. In the presence of water, TEOS undergoes hydrolysis:

$$\equiv Si\text{-}OR + H_2O \rightarrow \equiv Si\text{-}OH + ROH \tag{2.3}$$

where R is an ethyl group (C_2H_5). Upon hydrolysis, the condensation reaction follows:

$$\equiv Si\text{-}OR + \equiv Si\text{-}OH \rightarrow \equiv Si\text{-}O\text{-}Si\equiv + ROH, \text{ or} \tag{2.4}$$

$$\equiv Si\text{-}OH + \equiv Si\text{-}OH \rightarrow \equiv Si\text{-}O\text{-}Si\equiv + H_2O \tag{2.5}$$

The sol forms as a result of both reactions. The condensation reaction occurs initially on a microscale forming isolated clusters in solution (microgels). It results eventually in the large-scale network formation of gel. The reaction rates and resulting structures of silicate species are affected by several factors such as pH, water/alkoxide ratio and temperature.

Sols prepared with acid catalysis and low water content are important in fiber spinning [Sakk82]. The hydrolysis reaction in an acidic solution proceeds through an electrophillic reaction mechanism in which a protonated water molecule (H_3O^+) is attracted by oxygen atoms in alkoxy groups, forming a silanol group (Si-OH) and releasing an alcohol molecule [Ael50]. The extra proton is given up to protonate another water molecule. Due to positively charged attacking species (H_3O^+), the hydrolysis reaction is more favored than the condensation reaction as the electron density around the silicon increases with the number of alkoxy groups [Kee84]. The reaction occurs more likely in end groups than in middle groups since the end groups have more alkoxy groups. The result is more linear, less branched polymeric clusters. Such clusters in acid-catalyzed sols are illustrated in Figure 2.4 with comparison of those in base-catalyzed sols.

At a higher water content in an acidic solution, the extent of the hydrolysis reaction and the amount of hydroxyl groups available for the condensation reaction increase. The resulting clusters are more branched and cross-linked. At lower water contents (<2 water/alkoxide molar ratio), chain-like polymers are produced and are capable of being fiberized [Sakk82].

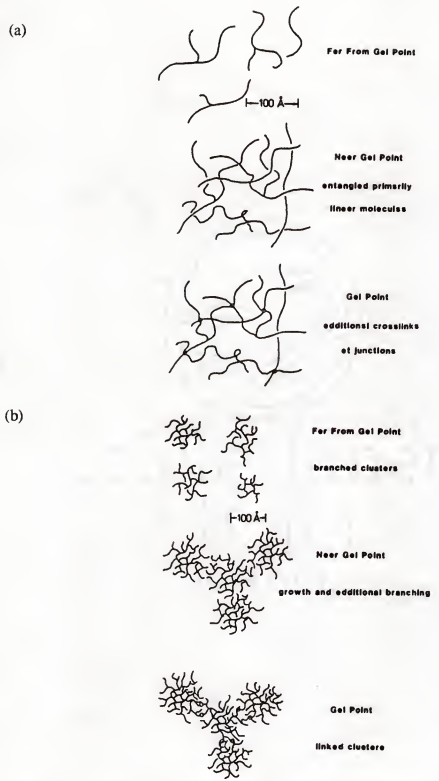

Figure 2.4. Schematic illustration of polymeric species and gel formation in (a) acid-catalyzed and (b) base-catalyzed TEOS sols [Bri85].

On the other hand, the hydrolysis reaction in a basic solution occurs slowly by a nucleophillic substitution mechanism [Ael50]. Keefer [kee84] proposed that a negatively charged hydroxide ion (OH^-) attacks silicon, releasing an alkoxy ion which reacts with water to generate a hydroxide ion. This reaction is retarded when there are bulky and highly basic alkoxy groups surrounding silicon in TEOS. Thus, monomeric hydrolysis products tend to be hydrolyzed at a faster rate than TEOS. Such a system could condense to form highly cross-linked, relatively compact polymer clusters or particles through Ostwald ripening by a dissolution and reprecipitation process.

The tendency to form dense, colloidal particles in basic solutions can also be explained by a condensation reaction in which a deprotonated silanol ($Si\text{-}O^-$) reacts with a nonionized silanol (Si-OH) releasing an hydroxide ion [Ile79]. In very acid solutions (pH<1.0), there are more protonated silanols ($Si\text{-}OH_2^+$), which react with nonionized silanols (Si-OH) and release protonated water molecules, leading to a higher condensation rate and subsequently producing very small spherical particles. Although, in general, highly cross-linked species do not lead to fiberization, fiber drawing has been reported from sols produced under very acidic conditions (at pH near zero) [Dah83]. It was suggested that chains produced from coalescence of extremely small particles (5 nm in diameter) also can lead to spinnability. Substantial chain flexibility would be retained by the coalesced chains due to the small particle size and residual alkoxy groups.

In contrast to the relatively slow hydrolysis reaction of silicon alkoxides, that of alkoxides of some transition and main group metals such as zirconium, titanium and

aluminum is extremely facile. As a result, insoluble oxide-alkoxide products are obtained [Yol82]. This makes the control of the polymerization reaction required for obtaining fiberizable polymeric species virtually impossible. The chemical properties of such metal alkoxides have been reviewed by Bradley et al. [Brad78]. A more recent review has been given by Mehrotra [Meh88]. An additional peptization step is necessary to form a stable colloidal sol, e.g., Al_2O_3 sol [Yol75].

In order to control the polymerization reaction of the metal alkoxides, chemical modifications using additives such as acetylacetone and acetic acid have been employed [Deb86, Gui86, Doe87, Pap89]. However, such chemical modifications have not been reported for preparing spinnable sols.

The influence of acetylacetone on the polymerization reaction of zirconium alkoxides has been investigated by Debsikhdar [Deb86] and Papet et al. [Pap89]. It has been proposed that acetylacetone reacts with zirconium alkoxides in the absence of water to form chelated complexes, allowing a control of hydrolysis. Steric hindrance prevents a fast hydrolysis of the bonds between the zirconium and the acetylacetone group and reduces the hydrolysis reaction rate.

Doeuff et al. [Doe87] has reported the formation of monolithic TiO_2 gels by hydrolysis of titanium alkoxide in the presence of acetic acid. In titanium butoxide, bidentate acetates have been reported to behave as either chelating or bridging ligands. Acetate replaces two alkoxy groups and is bonded directly to the titanium ion to form a chelated complex (chelating ligand), or bonded to two different titanium ions (bridging ligand). Hydrolysis of the modified precursors first removes alkoxy groups

and bridging acetates. Chelating acetates remain, slowing down both hydrolysis and condensation reactions, and can only be removed upon heating above 200°C.

Recently, another chemical modification of metal alkoxides has been used to prepare continuous SiO_2 fibers containing TiO_2 [Gun89]. A stable, homogeneous sol was obtained from polytitanosiloxanes prepared by the reaction of silicic acid with titanium chelate, bis(2,4-pentanedionato) titanium diisopropoxide. The sol was found to exhibit a good spinnability in the viscous state. Such an approach to modifying precursors can be useful in preparing fibers of binary and ternary oxide systems.

Rheology of Spinning Sols

Fiber Spinning

The continuous stretching of viscous liquids to form fibers is a primary manufacturing process for textiles and ceramic fibers. Figure 2.5 shows schematically the melt spinning process in which a polymer melt is extruded from a spinneret into ambient air at a temperature below the solidification temperature. The solidified fiber is taken up at a higher velocity than the mean extrusion velocity and hence thinning of the fiber takes place. There is some extrudate swell near the spinneret due to the viscoelasticity of the polymer. The solidified fiber is subjected to further downstream processing for property development.

Typical processing variables are the temperature of extrusion and ambient air, spinneret hole diameter, take-up velocity, cross-flow air velocity, and draw ratio. The draw ratio (D_R) is defined as the steady-state ratio of extrusion area to take-up area or

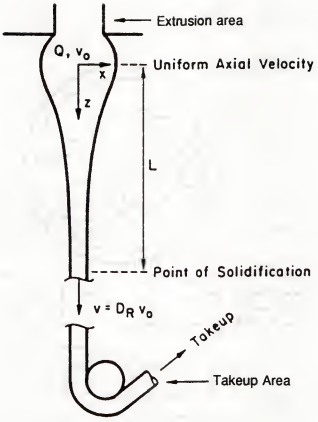

Figure 2.5. Schematic of continuous spinning process. The individual fibers from the spinneret containing many holes are taken together to form a yarn [Den80].

take-up velocity to extrusion velocity. Rheological properties are of value in defining regions of instability where fiber diameter and property fluctuation occur.

The stress and rate of diameter attenuation (take-up force and draw ratio) depend strongly on the rheological properties of the liquid being drawn, as shown in Figure 2.6. Chang and Denn [Chan79] have shown, from results of spinning a Newtonian corn syrup (η = 25 Pa·s) and a viscoelastic solution of poly(acrylamide) in corn syrup, that the force required to draw the non-Newtonian liquid is nearly two orders of magnitude greater than the force to draw the Newtonian liquid of equal viscosity at the same draw ratio. Similar large take-up forces have been observed for a variety of polymer melts, but direct comparison with comparable Newtonian liquid is not possible because of the more complex melt rheology.

Various physical aspects of fiber spinning for polymers have been reviewed by many investigators [Zia67, Pet79, Den80, Cog81]. General principles of the spinning process which also are applicable to the sol-gel fiber spinning are described below [Zia67, Den80].

First, the flow of a polymer or a spinning solution is steady-state and continuous. Any deviation due to non-uniformity of extruded material and variation of extrusion conditions results in turbulence and causes irregularity and non-uniformity of the resulting fibers.

Second, spinning is a non-equilibrium kinetic process with continuously varying parameters: temperature, stress, concentration, etc. The kinetics of spinning involves hydrodynamic flow, heat and mass transfer, and phase and structural

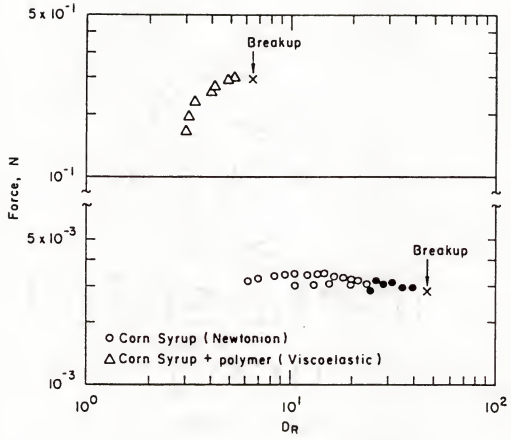

Figure 2.6. Take-up force as a function of draw ratio, D_R, for a Newtonian liquid and a non-Newtonian liquid of almost equal viscosity. Open symbols correspond to steady state and closed symbols to sustained oscillations in fiber diameters [Den80].

transformation. There is no mass transfer between the filament and the surroundings in the melt spinning process. However, dry and wet spinning processes such as those used for sols require mass transfer to remove solvents or to allow chemical reactions to occur.

Third, shear flow takes place when a spinning solution is extruded through the capillary of a spinneret hole. The flow velocity profile in the capillary channel of a spinneret is paraboloid. The velocity field involved in shear flow is that with a velocity gradient perpendicular to the flow direction.

Finally, elongational flow is a particularly important type of flow in fiber spinning. Elongational flow is called extensional, tensile, stretching or free-surface flow. The dominating type of deformation in spinning is uniaxial extension, which takes place during stretching of a fluid filament. The velocity gradient is parallel to the flow direction.

The rheological aspects of fiber spinning cannot be described in terms of shear flow behavior alone. Elongational flow behavior also should be considered since the flow occurring during fiber spinning has an elongational component. However, current experimental techniques do not yield reliable data on the elongational flow behavior [Bar89]. At the present, rheological behavior of a spinnable sol can be studied only by the shear viscosity measurements and the shear viscosity is used as a measure of spinnability. More details regarding the shear and elongational flow behaviors are discussed in Appendix A.

Shear Flow of a Colloidal Dispersion

Rheological properties of a colloidal dispersion depend on viscosity of the dispersion medium, concentration, size and shape of the dispersed particles, and forces of interaction between particles.

The forces arising from London-van der Waals attraction, electrostatic repulsion and steric repulsion lead to deflocculated, stable dispersions or flocculated dispersions, if the resulting net force is a repulsion or an attraction, respectively [Ove52, Nap77]. Brownian motion is important in the rheology of the dispersion of colloidal size particles. The constant random motion of the particles opposes structure buildup of the dispersion by affecting the radial distribution of particles of all shapes and by randomizing spatial orientation of non-spherical particles. The viscous forces are proportional to the local velocity difference between the particle and the surrounding liquid. These forces affect suspension viscosity via the viscosity of the continuous phase which, in turn, scales all such interactions [Bar89]. Hydrodynamic interactions, due to the presence of particles, also affect the flow through their concentration, size distribution and shape.

Dilute Colloidal Dispersions. For a very dilute dispersion of non-reacting spherical particles in a Newtonian liquid, the viscosity is given by the Einstein equation [Ein06, Ein11]:

$$\eta_r = \eta/\eta_o = 1 + 2.5\phi, \tag{2.6}$$

where η_r is the relative viscosity, η is the viscosity of the dispersion, η_o is the viscosity of the dispersion medium, and ϕ is the volume fraction of the particles in the dispersion. This equation is valid only for a dilute dispersion and does not include the effect of interaction between particles. In general, dilute colloidal dispersions prepared with Newtonian liquids show Newtonian flow behavior, whereas those prepared with non-Newtonian liquids exhibit non-Newtonian flow behavior.

Concentrated Colloidal Dispersions. The viscosity of a dispersion increases with increasing concentration due to particle shape, charge and hydrodynamic interaction arising when any particle comes into the vicinity of another. The dependence of the viscosity may be expressed by extending the Einstein equation in the power series [Rut64]:

$$\eta_r = \eta/\eta_o = 1 + 2.5\phi + k_1\phi^2 + \cdots. \tag{2.7}$$

However, deviations from the Einstein equation occur at high concentrations (>5-10 vol%) and can be seen from an empirical approach:

$$\eta_{red} = [(\eta/\eta_o) - 1]/\phi = 2.5 + k_1\phi + \cdots, \tag{2.8}$$

where η_{red} is the reduced viscosity. The deviation from the Einstein equation is illustrated in Figure 2.7 for a dispersion of spherical particles with the volume fraction ϕ up to 0.40.

Viscosity for a dispersion with a concentration >5-10 vol% is approximated by the Krieger-Dougherty equation [Krie59]:

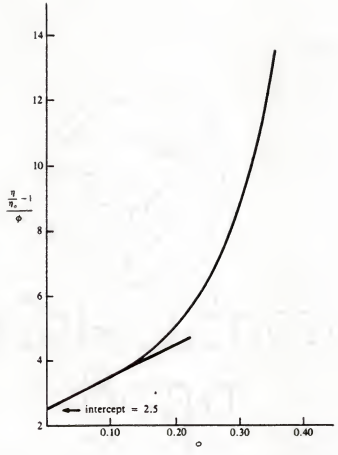

Figure 2.7. Reduced viscosity versus volume fraction for a dispersion of glass spheres in 65 μm diameter [Hie86].

$$\eta_r = \eta/\eta_o = [1 - (\phi/\phi_m)]^{-[\eta]\phi_m}, \tag{2.9}$$

where $[\eta]$ is the intrinsic viscosity and ϕ_m is the maximum packing fraction of particles. The intrinsic viscosity is the limiting value of the reduced viscosity and defined as

$$[\eta] = \lim_{\phi \to 0} [(\eta/\eta_o) - 1]/\phi. \tag{2.10}$$

The intrinsic viscosity is a characteristic of the dispersed particles and is affected by particle asymmetry. For spherical particles, $[\eta] = 2.5$. Asymmetry in particle shape increases the viscosity for the same volume. The rotation of non-spherical particles in the velocity gradient during flow produces a larger effective hydrodynamic volume and $[\eta]$ becomes greater than 2.5. Brownian motion randomizes the particles at low shear rates and can increase $[\eta]$. Rods have a greater effect than discs in increasing viscosity [Bar81].

The value of ϕ_m is strongly dependent on the particle-size distribution [Bar89]. A broader spherical particle-size distribution yields a high ϕ_m because the smaller particles can fit into the gaps between the larger particles. Non-spherical particles lead to poor space-filling and hence a low ϕ_m. Flocculation also can lead to a low ϕ_m because the flocs themselves are not close-packed. Experimental data fit well the Krieger-Dougherty equation (equation 2.9) over a wide range of ϕ and for different values of ϕ_m. Figure 2.8 shows the change in relative viscosity of the dispersion of

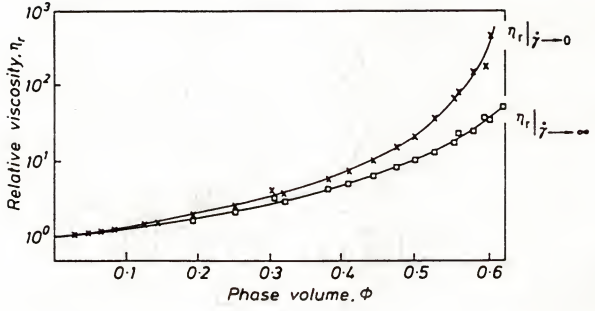

Figure 2.8. Relative viscosity versus volume fraction for monodispersed latices. The upper curve corresponds to the zero shear-rate asymptotic value of relative viscosity with $[\eta] = 3.133$ and $\phi_m = 0.632$ in the equation 2.9. The lower curve corresponds to the high shear-rate asymptotic value of relative viscosity with $[\eta] = 2.710$ and $\phi_m = 0.708$ in the equation 2.9 [Bar89]. Solid lines are based on equation 2.9 while the cross and square represent experimental values.

latices with increasing the volume fraction ϕ at very low and very high shear rates.

When a dispersion containing charged particles is sheared, extra energy is required to overcome the interaction between ions in the electrical double layers around particles and the electrical charge on the particle surfaces. The result is an increase in viscosity (electroviscous effects) [Kri72]. At low ionic strength, the double layer repulsions between the particles are relatively long range, while at high ionic strength, the range of the double layer interactions is small. Therefore, the viscosity increases with decreasing ionic strength. This effect becomes more important for colloidal size particles with high charge or low ionic strength since the electrical double layers are relatively large compared to the particle sizes [Goo87]. As the shear rate increases, the electrostatic contribution diminishes and the hydrodynamic forces dominate. Thus, the viscosity of the dispersion decreases, i.e., shear-thinning, and follows the Krieger-Dougherty equation (equation 2.9) for non-interacting particles.

Well-dispersed colloidal dispersions exhibit Newtonian flow behavior (see Appendix A) at low and moderate concentrations. Dispersions at higher concentrations may exhibit shear-thickening at high shear rates. The magnitude of shear-thickening depends on volume, particle-size distribution and liquid viscosity. The shear-thickening becomes significant at approximately 50 vol% of particles and is usually followed by shear-thinning [Bar89]. A wide particle-size distribution can decrease the magnitude of shear-thickening. Very high concentrations of dispersions tend to show plastic flow behavior due to particle-particle interlocking.

Flocculated dispersions at low and moderate concentrations can exhibit Newtonian flow but their viscosities are higher than those for well-dispersed dispersions. The immobile liquids trapped in voids of agglomerates increase the effective volume and thus increase viscosities. However, at high concentrations, flocculated dispersions show shear-thinning flow behavior (see Appendix A) due to the breakdown of the floc structure. At higher concentrations, plastic flow behavior appears due to floc-floc interlocking.

Spinnability

The most important consideration in preparing fibers is the spinnability of sols or solutions. In a spinnable sol, as a spin mix is forced through a spinneret hole, a continuous fiber-shaped structure must be formed which is self-supporting enough to be moved away by mechanical means. Spinnability is a necessary prerequisite to fiber formation, but does not guarantee fiber-forming ability. There are many known spinnable liquids such as honey, high-mineral oils and soap solutions which are not considered as fiber-forming. To be considered a fiber-forming liquid, a continuous filament several feet long should result. The spinnability can be tested qualitatively by conventional methods, the pulling rod method and the falling drop method.

It has been suggested that an increase in elongational viscosity (η_E) with tensile stress (tension-thickening) is an essential condition for spinnable liquid [Cog81]. A breakup of a fluid filament at a neck (necking) can be prevented when the increased elongational viscosity compensates the high local stress arising from the

neck (see Appendix A). However, Ziabicki [Zia67] argued that there is a marked difference between deformation of solids and liquids and that a breakup in the fluid filament cannot be described in the same way as necking in a solid. Much experimental data, together with theoretical considerations, indicate that formation of long liquid threads also is possible in Newtonian liquids at constant elongational viscosity.

The maximum thread length is considered to be a measure of spinnability. It has been observed that a maximum thread length of a liquid depends on not only the viscosity of the liquid, but also on the extrusion speed. In Figure 2.9 (a), the thread length (x^*) is presented as a function of the product of viscosity and extrusion speed (ηV) for a cellulose acetate solution. Ziabicki [Zia67] has suggested that the filament breakup occurs at a critical stress by cohesive fracture for very viscous liquids and by a capillary mechanism for low-viscosity liquids. The theoretically determined thread length for both mechanisms is shown in Figure 2.9 (b).

The first process responsible for the observed thread length is a cohesive (brittle) fracture of the liquid thread due to applied tensile stress (Figure 2.10 (a)). There is some critical level of stored elastic energy above which the material undergoes fracture. In the case of homogeneous liquids, the stored elastic energy is of the order of the cohesive energy density (K). Therefore, for uniaxial extension of a linear viscoelastic liquid, the condition of brittle fracture becomes

$$W_{el}^* = \sigma_{xx}^{*2}/2E \approx K, \tag{2.11}$$

(a)

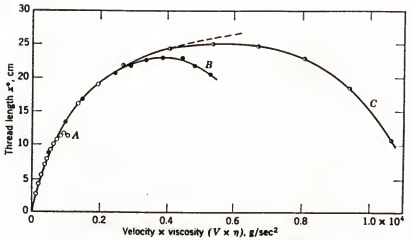

(b)

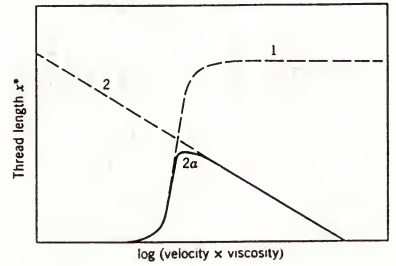

Figure 2.9. Thread length (x^*) as a function of the product of extrusion velocity and viscosity ($V\eta$). (a) Experimentally determined x^* for solutions of cellulose acetate in an acetone and water mixture. The viscosities of the solutions in curve A, B and C are η_0 = 9, 48 and 134 Pa·s, respectively. (b) Theoretically determined x^*. The curves 1 and 2 are due to a capillary breakup and cohesive fracture, respectively. The solid line is due to cohesive fracture in the presence of capillary waves [Zia67].

(a)

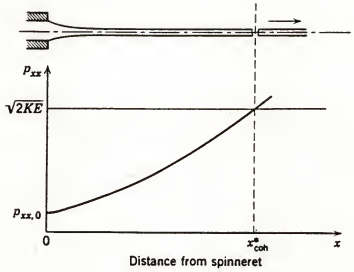

(b)

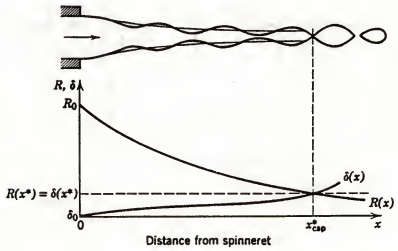

Figure 2.10. Schematic illustration of liquid thread breakup mechanisms. (a) Cohesive fracture of a steady-state liquid thread. (b) Capillary breakup of a steady-state liquid thread [Zia67].

where W_{el}^* is the critical elastic energy, σ_{xx}^* is the critical tensile stress, and E is Young's modulus. The tensile stress (σ_{xx}) changes when the liquid thread is continuously elongated. Deformation is possible up to the moment at which the critical value σ_{xx}^* is reached. The thread length is expressed by assuming a simple exponential velocity distribution along the steady-state liquid thread:

$$x_{coh}^* \approx \xi^{-1}\ln[(2KE)^{1/2}/3\xi V_o\eta] = \xi^{-1}\ln[(2K/E)^{1/2}/3\xi V_o\tau], \qquad (2.12)$$

where V_o is the initial velocity of the liquid thread and ξ (= dlnV/dx) is the deformation gradient. The thread length (x_{coh}^*) determined by cohesive fracture increases with cohesive energy density (K) and decreases with velocity (V_o), deformation gradient (ξ) and relaxation time (τ), in accordance with experimental data for highly viscous materials.

Another process limiting the thread length is associated with surface tension and involves spontaneous development of surface waves (capillary waves), on the free surface of the liquid thread (Figure 2.10 (b)). Any small distortions of the free surface of the liquid thread can grow spontaneously and lead to a breakup into drops according to

$$\delta(t) = \delta_o\exp(\mu t)\cos(2\pi x/\lambda), \qquad (2.13)$$

provided that $\lambda > 2\pi R$. The δ denotes axially symmetrical distortion of the thread radius (R), t the time, μ the growth factor, and λ the wavelength. The original distortions with amplitude (δ_o) (usually of the order of 10^{-5}-10^{-6} cm) can be generated

in a spinneret as a result of pressure oscillations, fluctuations of density, etc. The liquid thread breaks when the growing amplitude reaches the radius of undistorted thread, i.e., $\delta(x^*) = R(x^*)$.

The thread length governed by the capillary breakup is estimated as

$$x_{cap}^* \approx 2\xi^{-1}[\ln(R_o/\delta_o) - \alpha/3\eta V_o \xi R_o], \tag{2.14}$$

which is valid for small ratios $(\alpha/3\eta V_o \xi R_o)$; R_o is the initial radius of the thread and α is the surface tension. According to the equation (2.14), x^* actually increases with $(\eta V_o R_o/\alpha)$, though not linearly.

Under a given set of conditions, the break mechanism which causes earlier breakage, i.e., yields smaller x^* values, is expected to determine the maximum thread length. Actually, in the presence of external tensile stress, the capillary breakup proceeds according to the cohesive fracture mechanism. When the node of the capillary wave becomes sufficiently thin, the tensile stress attains its critical value before complete separation of the drops occurs. As shown in Figure 2.9 (b), x^* increases with (ηV_o) for smaller values of the parameter when the capillary mechanism prevails and decreases in the higher (ηV_o) region corresponding to the cohesive fracture.

In general, when the viscosity of a spinning fluid is too low, e.g., a dilute solution in dry spinning or at high melt temperature, the spinning fluid leaves the spinneret in individual drops; the capillary breakup causes nearly simultaneous formation of several small droplets resulting from capillary waves. On the other hand,

highly viscous spinning solutions with too long relaxation time lead to cohesive fracture, followed by slow shrinkage of the broken ends. In the latter case, only slow spinning is possible.

The effect of rheological factors (non-linear viscosity, elasticity, elongational viscosity) on the maximum thread length is complex and depends itself on the conditions of flow, i.e., constant tensile force or constant deformation, and on the values of involved variables. Increasing both elongational viscosity and elasticity lead to formation of long threads in some cases, while leading to lower maximum thread length in others [Zia67]. However, variation of elongational viscosity with the deformation rate can also affect the maximum length of obtained liquid threads. Therefore, spinnability should be treated experimentally, not theoretically. However, experimentally determined spinnability depends on the testing methods (e.g., centrifugal spinning or the pulling rod method) which cause different flow conditions.

Rheological Behavior of Spinning Sols

Much of the work on the rheological properties of sols has been carried out by Sakka and coworkers [Sakk82, Mak88, Koz88, Sak88, Sakka88] who studied shear flow behavior as it relates to fiber spinning behavior. The rheological studies were limited to SiO_2 and Al_2O_3 sols. As mentioned previously, spinnability cannot be explained entirely by shear flow behavior; elongational flow behavior should also be considered. However, due to the difficulty in measuring elongational viscosity, steady

shear viscosity measurements are used in obtaining structural information on the spinnable sol.

Silica Sol. Sakka and Kamiya [Sakk82] have suggested that the shape of polymeric species formed in the sols is an important factor for the spinnability of the sols. When a small amount of water and an acid catalyst are used in the hydrolysis, the sols contain linear, less branched polymer clusters, which give rise to spinnability of the sol. When a large amount of water or a base catalyst is used, non-linear polymers are formed in the sols which are non-spinnable.

The spinnability of TEOS sols has been explained from reduced viscosity measurements [Sakk82] and intrinsic viscosity measurements [Sakka88]. Sakka and Kamiya [Sakk82] have found concentration dependence of the reduced viscosity in spinnable sols but not in non-spinnable sols. The concentration dependence was attributed to the presence of chain-like or linear polymers. Sakka and Kozuka [Sakka88] determined the shape of the polymers in spinnable sols using the Staudinger-Mark-Houwink equation [Hie86]:

$$[\eta] = k(\bar{M}_n)^{\alpha}, \tag{2.15}$$

where k is a constant depending on the polymer-solvent system and temperature and $\bar{M}_n$ is the number average molecular weight related to the intrinsic viscosity $[\eta]$. The exponent α is the diagnostic parameter because it depends on the shape of the particles in the sol. For spherical polymers, $\alpha \approx 0$. For non-flexible, rigid rod-like polymers,

α=1.0-2.0. For flexible, linear polymers, α is in the range of 0.5-1, which correspond to the values for the spinnable sols.

Kozuka et al. [Koz88] investigated the flow behavior of spinnable TEOS sols, hydrolyzed with a low water content (H_2O/TEOS molar ratio=2) and an acid, with respect to shear rate, as shown in Figure 2.11. When the solvent was allowed to evaporate during reaction (open system), the sol behaved as a Newtonian liquid up to a highly viscous state (≈10 Pa·s) and showed spinnability at viscosity above 1 Pa·s (Figure 2.11 (a)). On the other hand, when the solvent was not allowed to evaporate during reaction (closed system), the sol behaved as a non-Newtonian liquid in a viscous state and showed no spinnability (Figure 2.11 (b)). The closed system sol exhibited shear-thinning behavior and changed to thixotropic behavior (see Appendix A) as aging time increased. The same authors proposed that the increase in viscosity of the open system sol is attributed to the increasing concentration while maintaining one-dimensional linear polymers. Whereas, that of the closed system sol was attributed to the formation of the three dimensional network in the sol.

In contrast to the finding of Kozuka et al. [Koz88], Sacks and Sheu [Sac86] observed the spinnability in TEOS sols hydrolyzed with a low water content after the sol became shear-thinning and the best spinnability prior to the transition to thixotropic behavior (Figure 2.12). Sacks and Sheu [Sac86] pointed out that the flow behavior of the spinnable sol depends on shear rate conditions. The sol may exhibit a Newtonian behavior in a narrow range of shear rates, but viscosity values can vary with shear rate over a wider range of shear rates.

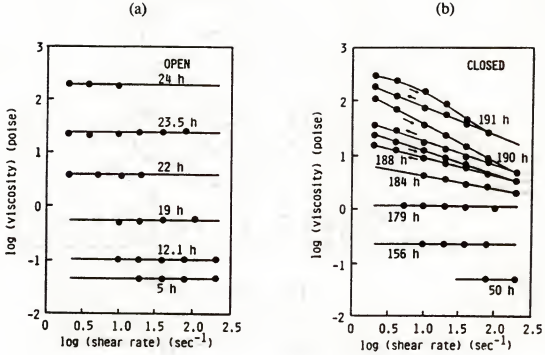

Figure 2.11. Viscosity as a function of shear rate for spinnable and non-spinnable TEOS sols. (a) Spinnable sol in an open system allowing evaporation of solvents. (b) Non-spinnable sol in a closed systems not allowing evaporation of solvents. Numbers attached to the curves indicate aging time [Koz88].

(a)

(b)

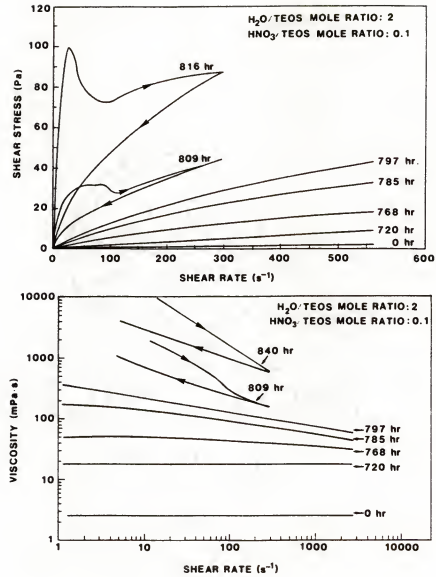

Figure 2.12. Flow behavior of an acid-catalyzed TEOS sol hydrolyzed with a low water content at various aging times. (a) Shear stress versus shear rate. (b) Viscosity versus shear rate. The spinnability was observed after aging for 785 hours [Sac86].

In general, the viscosities of TEOS sols increase gradually as the hydrolysis and condensation reactions proceed and then rapidly when gelation occurs. For longer aging times, the viscosity becomes increasingly dependent on shear rate.

Acid-catalyzed TEOS sols exhibit transitions from Newtonian to shear-thinning to thixotropic behavior with increasing aging time [Sac86]. Figure 2.12 shows the transitions in the flow behavior of the sol occurring at various aging times. In an early stage of hydrolysis and condensation reactions, the concentration of polysiloxane species is relatively low and does not influence the flow. As aging proceeds, there is continued formation and condensation growth of polysiloxane clusters, along with agglomeration of the clusters. This results in shear-thinning behavior when the cluster-agglomerates break down at high shear rates. With continued aging, condensation growth and agglomeration of the clusters result in the formation of a continuous, three-dimensional network of gel. The thixotropic behavior arises from a gradual recovery of the agglomerates breakdown when shear stress is removed.

Alumina Sol. Alumina sols prepared from alkoxides exhibit similar transitions in the flow behavior of colloidal dispersions, as discussed previously. As the sol is concentrated by evaporating water, the aluminum hydroxide particles agglomerate progressively with one another and form three-dimensional gel networks.

Maki and Sakka [Mak88] observed that the flow behaviors in Al_2O_3 sols prepared from an inorganic aluminum salt ($AlCl_3 \cdot 6H_2O$) are quite consistent with those observed in TEOS sols. The sol containing fibrous long-shaped particles became spinnable in the viscosity range of 1-100 Pa·s, while the sol containing round or

granular-shaped particles was not spinnable. The spinnable sols exhibited a Newtonian flow or a near Newtonian flow throughout the investigated viscosity range. The non-spinnable sols exhibited a Newtonian flow but a shear-thinning behavior at viscosities higher than about 1 Pa·s.

The spinnability of the Al_2O_3 sols has been explained by Maki and Sakka [Mak88], who suggested that, as the solvent evaporates, the long-shaped particles in the spinnable sols are not entangled due to the non-flexible nature of the fibrous Al_2O_3 particles. This would lead to Newtonian behavior and also to spinnability. On the other hand, the sols containing round particles gather together, forming agglomerated network structures as the solvent evaporates. This type of structure leads to shear-thinning behavior and no spinnability. However, this scenario is unlikely. Alkoxide-derived Al_2O_3 sols contain similar fibrous boehmite particles to those in the spinnable sol derived from the aluminum salt. They exhibit a shear-thinning behavior in a viscous state and no spinnability.

Properties and Microstructures of Oxide Fibers

Mechanical properties of oxide fibers are very much dependent on their microstructures. The most important factors affecting mechanical properties are grain sizes, porosity and flaws. Grain growth should be suppressed at the service temperature. Glassy phases at grain boundaries and flaws generated during processing should be kept to a minimum, in order to avoid a strength decrease at high temperatures.

Ceramic fibers exhibit flaw-controlled brittle fracture behavior. In general, tensile strength decreases as gauge length increases, due to an increase in flaw populations. A recent study of the SiC-based fibers showed the effects of flaw types on tensile strength [Saw87]. Failure is initiated by internal flaws such as inclusions, pores, large grains, and grain boundaries, and surface flaws introduced during fiber manufacture. Low tensile strength in the fibers was attributed to surface flaws and particle defects within the fibers. Higher tensile strength was observed in the fibers where granular defects and heterogeneous particles were confined to the interior. The highest strength was observed in the fibers exhibiting no defects [Saw87].

In pure, polycrystalline oxide fibers, the small grain size and low porosity criteria for the best mechanical properties of the fibers are incompatible, since low-temperature sintering conditions employed to achieve small grain sizes lead to pore growth. High sintering temperatures necessary to completely eliminate porosity inevitably lead to massive grain growth. Therefore, it is very difficult to optimize fiber microstructure with sintering temperature alone. Incorporation of a second phase is usually necessary to achieve this goal. A second phase restricts grain boundary mobility, while porosity is removed. Careful selection of the type and concentration level of the second phase make it possible to also inhibit grain growth during processing and at service temperatures.

Typical grain growth inhibitors for Al_2O_3 are MgO, SiO_2 and ZrO_2 [Bir85]. Magnesia has been used as a grain growth inhibitor for α-Al_2O_3 but is effective only for micron-sized grains. However, in fiber manufacture, it is essential to control the

growth of sub-micron-sized grains. Silica is known to be most effective for Al_2O_3-based fibers. Silica stabilizes the various forms of transition Al_2O_3, allowing for the removal of porosity before full conversion to α-Al_2O_3 takes place. Once α-Al_2O_3 is nucleated, silica acts as a grain growth inhibitor at high temperatures. This is achieved by the formation of mullite crystallites at Al_2O_3 grain boundaries. Unfortunately, excess SiO_2 in the fibers results in a strength decrease at elevated temperatures due to creep.

The room-temperature properties of some commercial oxide fibers are summarized in Table 2.3. These fibers are either Al_2O_3- or mullite-based with tensile strengths ranging from 1 to 2 GPa. It should be noted that strengths of the fibers cannot be easily compared to one another due to their dependence on the gauge lengths and testing methods. Recently, high-temperature strengths of three oxide fibers, Nextel™ 480, FP and PRD-166, under equivalent test conditions have been reported by Pysher et al. [Pys89]. The strength and elastic modulus as a function of temperature for oxide fibers are shown in Figure 2.13.

Among the three oxide fibers, mullite-based Nextel™ 480 exhibits the highest tensile strength at room temperature. This is because the fiber has few processing flaws and consists of very small mullite crystallites [Joh87]. The room-temperature strength of FP fibers consisting of α-Al_2O_3 is lower than those of the mullite-based fibers. The higher strength of PRD-166 than FP is attributed to the fine dispersion of tetragonal ZrO_2 in the α-Al_2O_3 matrix. As shown in Figure 2.13 (a), however, large strength reductions at 1200°C and almost complete loss of strength at 1300°C for all

TABLE 2.3

Room-Temperature Mechanical Properties of Oxide Fibers[+]

Fiber	Phase[*]	Diameter (μm)	Tensile Strength (MPa)	Tensile Modulus (GPa)	Upper Use Temperature (°C)
Nextel 312	aluminum boro-silicate	10-12	1700 (2")[†]	150	1200
Nextel 440	mullite+γ-Al_2O_3 +SiO_2	10-12	2000 (2")	190	1430
Nextel 480	mullite	10-12	1900 (2")	220	1430
Nextel Z-11	ZrO_2+SiO_2	14	1310 (1")	76	1000
FP	α-Al_2O_3	20	1380 (0.25") 1310 (2")	380	1320
PRD-166	α-Al_2O_3+ tet-ZrO_2	20	2100 (0.25") 1914 (1") 1339 (2")	380	1320
Sumica	transition Al_2O_3+SiO_2	17	1790	210	1250
Saffil	transition Al_2O_3+SiO_2	3	1030	103	1400

[+] [Sum83, Sow85, Hol87, Joh87, Mah87, Rom87]

[*] Fiber Compositions:

Nextel 312: 62% Al_2O_3, 14% B_2O_3, 24% SiO_2
Nextel 440: 70% Al_2O_3, 28% SiO_2, 2% B_2O_3
Nextel 480: 70% Al_2O_3, 28% SiO_2, 2% B_2O_3
Nextel Z-11: 68% ZrO_2, 32% SiO_2
FP: >99% α-Al_2O_3
PRD-166: 80% α-Al_2O_3, 20% tet-ZrO_2
Sumica: 85% Al_2O_3, 15% SiO_2
Saffil: 95% Al_2O_3, 5% SiO_2

[†] Gauge Length (inch)

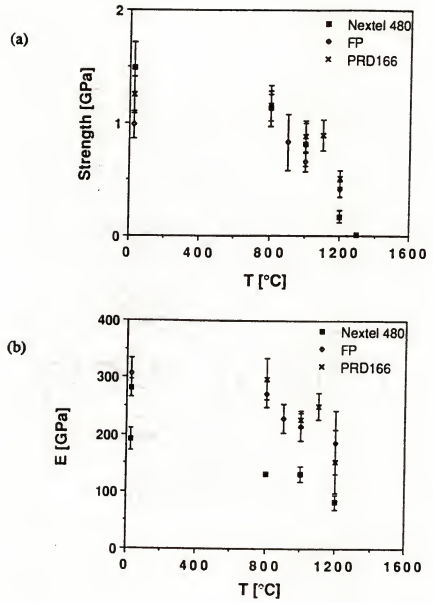

Figure 2.13. Tensile strength (a) and elastic modulus (b) as function of temperature for oxide fibers [Pys89]. A single fiber was tested with 3 inch gauge length in air and at least 10 tests were made. Error bars represent 95% confidence limits.

fibers are attributed to either softening of intergranular glassy phases or excessive grain growth [Pys89]. Elastic moduli of FP and PRD-166 fibers are larger than that of Nextel™ 480, due to the lower elastic modulus of mullite. However, the elastic moduli of all fibers decrease with increasing temperature (Figure 2.13 (b)).

Nextel™ 480 has been reported to retain 60% of its room temperature strength after exposure to 1400°C for 2 hours in air and then cooling to room temperature [Joh87]. PRD-166 has been reported to retain 75% of its room temperature strength after the same exposure and even after exposure for 100 hours [Rom87]. The retention of strength after high temperature exposure is due to the increased resistance to grain growth and creep which arises from increased mullite content in Nextel™ 480 or finely dispersed ZrO_2 particles in PRD-166.

Zirconia-Yttria System

Polymorphism of Zirconia

Pure ZrO_2 exhibits three well defined polymorphs. There are the monoclinic, tetragonal and cubic structures. The monoclinic ZrO_2 is stable up to approximately 1170°C where it transforms to the tetragonal phase, which then transforms to the cubic fluorite structure at 2370°C and finally melts at 2680°C. These structures are shown schematically in Figure 2.14. It also has been shown that a high pressure orthorhombic form exists in ZrO_2 [Liu80].

Of significance is the martensitic nature of the monoclinic $\leftrightarrow$ tetragonal transformation, suggested by Wolten [Wol63]. The transformation occurs by shear

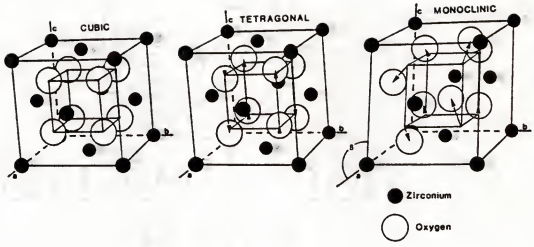

Figure 2.14. Crystal structures of three stable polymorphs of zirconia [Heu87]. The arrows in the tetragonal and monoclinic structures indicate the displacements of the oxygen from its positions in the cubic phase.

movement of the atoms through distances less than an interatomic distance. The transformation from the tetragonal to monoclinic phase is accompanied by a 3-5% volume increase, which makes pure ZrO_2 unsuitable when cycled between low and high temperatures. Fortunately, the transition can be avoided by the addition of stabilizing oxides such as Y_2O_3, MgO, CaO, CeO_2 and several rare earth oxides. The addition of stabilizing oxides in sufficient concentrations allows the stability of the cubic form of ZrO_2 from room temperature to its melting point.

The volume expansion of the tetragonal to monoclinic transformation can be used to improve the toughness and strength of ceramics. Garvie et al. [Garvi75] were the first to realize the potential of ZrO_2 for increasing both strength and toughness of ceramics. This is achieved by utilizing the transformation of metastable tetragonal particles to the monoclinic phase which is induced by the presence of the stress field ahead of a crack. The volume change and shear strain developed in the martensitic transformation were recognized as opposing the opening of the crack and therefore acting to increase the resistance of the ceramic to crack propagation.

Although the tetragonal phase in pure ZrO_2 cannot be quenched to low temperatures, it can be produced and retained metastably in many ways. Thermal decomposition and solution-precipitation of various zirconium salts and alkoxides produce metastable tetragonal ZrO_2 powder. A hydrated, amorphous ZrO_2 has been produced by precipitation from a zirconyl chloride ($ZrOCl_2 \cdot 8H_2O$) solution with excess bases such as ammonia and soda [Gar65, Liv68, Mit74]. Progressive heating above 200°C dehydrates the precipitates. Heating to 500°C crystallizes out the tetragonal

phase. At temperatures over 600°C, the tetragonal phase reverts to the stable monoclinic. Based on the hypothesis that the tetragonal particles have a lower surface free energy than the monoclinic, Garvie [Gar65] has suggested that the formation of metastable tetragonal ZrO_2 is due to a small crystallite size. He found that the crystallite sizes for stabilizing the tetragonal phase must be smaller than 30 nm. This was supported by Bailey et al. [Bai72], who observed the formation of the tetragonal phase in excessively milled ZrO_2.

The tetragonal phase also can be retained at room temperature when a constraint imposed by the matrix opposes either or both of the volume and shape changes. Metastable tetragonal ZrO_2 can exist either as precipitates in a cubic matrix of partially-stabilized ZrO_2 (PSZ) [Ban75] or as particles in ceramic matrices such as Al_2O_3 [Heue82]. However, there are critical sizes required for metastable tetragonal particles to be retained. The critical sizes depend on the matrix constraint and composition of the ZrO_2. If the particle sizes are smaller than a critical size, they will not transform on cooling. They can transform under stress and increase fracture toughness of the matrices (stress-induced phase transformation toughening). If they are larger than a critical size, they will transform spontaneously and can also increase fracture toughness (microcracking).

Phase Equilibria in the Zirconia-Yttria System

The phase diagrams for this system have been studied extensively [Sco75, Stu78, Ruh84, Rüh84]. However, there have been considerable discrepancies

regarding the exact location of phase boundaries. The difficulties in establishing the precise diagram arises from the sluggish solid-state reactions in ZrO_2 at relatively high temperatures (<1400°C). The slow rates of these reactions can be attributed to the slow diffusion rates of cations, coherency strains between different phases which may influence the extent of the phase fields, and retention of the metastable phase at low temperatures. The phase diagram reported by Scott [Sco75] is the most reliable one. The ZrO_2-rich portion of the ZrO_2-Y_2O_3 phase diagram is given in Figure 2.15, which is the most relevant for the present study.

The most important feature of the ZrO_2-Y_2O_3 phase diagram is the decrease in temperature of the tetragonal to monoclinic transformation with increasing Y_2O_3 content, as shown in the tetragonal phase field (T_{ss}) in Figure 2.15. This has important implications for the design and use of toughened ceramics produced as either partially stabilized or as heterogeneous two phase systems, since the upper temperature limit for any application is determined by the monoclinic-tetragonal transformation temperature.

As the temperature increases above the monoclinic phase field (M_{ss}), a narrow monoclinic and tetragonal field (M_{ss}+T_{ss}) is encountered before a tetragonal field is reached. The tetragonal solid solution exists in a composition range 0-≈2.6 mol% Y_2O_3. For compositions greater than 2.6 mol% Y_2O_3, a mixture of tetragonal and cubic solid solutions exists. Compositions greater than ≈10 mol% Y_2O_3 result in a homogeneous cubic solid solution, stable from room temperature to melting point.

It should be noted that the stability of phases in ZrO_2 should be considered from both thermodynamic and kinetic aspects. However, these aspects still are not

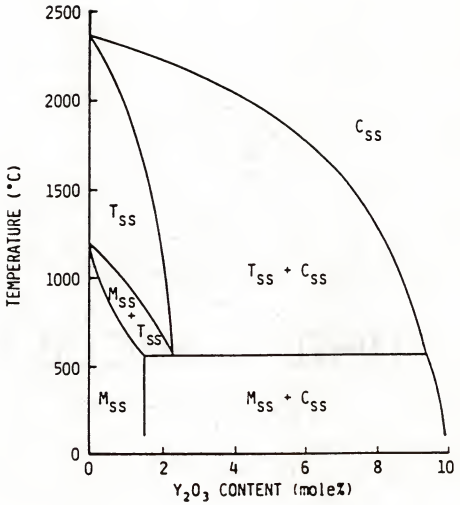

Figure 2.15. Phase diagram for the zirconia rich portion of the zirconia-yttria system [Sco75]. M_{ss}, T_{ss} and C_{ss} correspond to monoclinic, tetragonal and cubic solid solutions, respectively. The fibers investigated in this study contained 2 or 3 mol% Y_2O_3.

completely understood. The phase stability is affected mostly by kinetics at low temperatures due to much slower diffusion of zirconium and stabilizing cations than the oxygen ion [Rho66].

Yttria-stabilized Tetragonal Zirconia Polycrystals

Yttria-stabilized tetragonal ZrO_2 polycrystals (Y-TZP) were first reported by Rieth [Rie76] and subsequently by Gupta and coworkers [Gup77]. The high strength (1-1.2 GPa) and high fracture toughness (8-10 $MPam^{1/2}$) of the Y-TZP ceramics can be attributed to the presence of almost 100% metastable tetragonal phase and fine-grained microstructures. High values for the fracture toughness have been obtained in Y-TZP with a composition of approximately 2 mol% Y_2O_3. The composition lies close to the phase boundary between the tetragonal phase field and the tetragonal phase and cubic phase field. The high fracture toughness is attributed to a large amount of the metastable tetragonal phase which is transformed readily by stress. A maximum in the fracture strength has been obtained in the Y-TZP with a composition of 3 mol% Y_2O_3 where a small amount of the cubic phase usually is present as large grains [Mat84, Rüh84, Tsu84]. Generally, in fibers, the presence of large grains is undesirable.

The Y-TZP can be sintered to full density at relatively low temperatures (<1400°C) due to the presence of a liquid phase at the grain boundaries. The low sintering temperatures do not allow equilibrium phases to be attained in the relatively short sintering schedules. The Y-TZP always contains an amorphous phase, rich in SiO_2, which is present in ZrO_2 powders. At high sintering temperatures, SiO_2 and

other trace impurity oxides combine to form a liquid phase which remains as a glass upon cooling [Rüh84]. This intergranular phase plays a significant role in both the densification and in the properties, particularly those at high temperatures. In general, Y-TZP ceramics are not considered to be high-temperature structural materials (>1000°C). Due to the presence of the liquid phase, the high-temperature strength of Y-TZP drastically decreases. Also, fine-grain size and a loss of transformation toughening effect with increasing temperature contribute to the decrease in strength of Y-TZP.

Influence of Alumina Addition to Yttria-Stabilized Tetragonal Zirconia

Tsukuma and coworkers [Tsuk85, Tsu87] have reported that the addition of Al_2O_3 to Y-TZP results in, not only an increase in room and in high-temperature strengths of Y-TZP, but also in a more uniform, fine-grained microstructure. The Y-TZP/Al_2O_3 composites containing 20 wt% Al_2O_3 exhibited extremely high strength (2.4 GPa) at room temperature [Tsuk85]. As shown in Figure 2.16, their strength decreased at high temperatures, but still was relatively high (≈750 MPa at 1000°C) [Tsu87]. The addition of 40 wt% Al_2O_3 further increased high-temperature strength of the Y-TZP up to 1 GPa at 1000°C, which was nearly four times higher than that of the Al_2O_3-free Y-TZP.

The strength data of Tsukuma and coworkers [Tsuk85, Tsu87], particularly those for the samples tested at high temperature (Figure 2.16), are very encouraging for producing high-temperature, high-strength fibers. Comparing their data for bulk

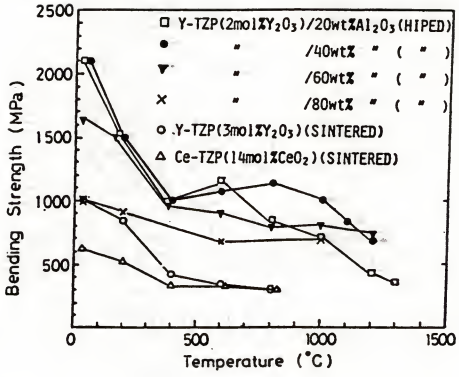

Figure 2.16. Strength as a function of temperature for TZP and TZP/Al_2O_3 bulk composites [Tsu87]. Fibers prepared from the same material are expected to yield even higher strengths.

samples to those of Al_2O_3 and mullite-based fibers (Table 2.3 and Figure 2.13), the strength of Y-TZP/Al_2O_3 fibers is expected to considerably exceed those of Al_2O_3- and mullite-based fibers at room temperature and 1000°C. In general, strengths of the fibers are a factor of 2 or higher than those of the same bulk materials [Mor87]. This makes the Y-TZP/Al_2O_3 system appear even more promising.

The addition of Al_2O_3 is believed to serve two major purposes. First, dispersion of Al_2O_3 particles with higher elasticity than that of the matrix increases the elastic modulus of composites. Lange [Lan82a] suggested that an increase in elastic modulus of the composite matrix will enlarge the critical transformation size of ZrO_2 particles to allow more metastable tetragonal ZrO_2 particles to be retained in the matrix, thus increasing toughness and strength.

Secondly, the fine particles of Al_2O_3 can contribute to grain boundary pinning and inhibit grain growth of ZrO_2 at high temperatures, improving high-temperature strength. It has been reported that the Al_2O_3 inclusions inhibit the grain growth of ZrO_2 at temperatures up to 1600°C, where the inclusions are relatively immobile and are located primarily within ZrO_2 grains [Lan87]. Alumina particles also can prevent the development of large grains of the cubic ZrO_2 phase, which are inevitably present in TZP ceramics, and result in uniform fine grained microstructures.

Alumina can exist as discrete particles in the Y-TZP matrix, since the solubility of Al_2O_3 in ZrO_2 is negligible. It has been reported that Al_2O_3 is only 0.1 mol% soluble in Y_2O_3-fully stabilized ZrO_2 (YSZ) and can be dissolved up to 1-2 mol% at 1700°C [Bau69]. A slight solubility of ZrO_2 in Al_2O_3 (0.1 wt%) up to

1600°C, as well as that of Al_2O_3 in YSZ, was reported from diffusion processes and solid-state reactions between Al_2O_3 and YSZ by Kosmac et al. [Kos84]. They also observed no reaction and no solubility of Y_2O_3 in Al_2O_3 at temperatures up to 1600°C, despite the fact that, in the Al_2O_3-Y_2O_3 binary system, the solubility of Y_2O_3 was reported to be in the range of 1 mol% [Lev75].

CHAPTER III
RESEARCH OBJECTIVES AND ACCOMPLISHMENTS

Fabrication of the Y-TZP/Al_2O_3 fibers requires a broad knowledge of sol-gel processing and microstructure/property relationships. To date, there has not been any systematic study reported in the literature regarding the various aspects of ceramic fiber processing. Studies, at least as reported in the open literature, are limited to either characterization or testing and contain little, if any, processing information. Processing includes all those steps required to fabricate stable fibers: preparation of sol precursors, tailoring of the sol chemistry consistent with desired fiber composition, modification and control of rheology to obtain spinnable sols, spinning, calcination to reduce the sols to oxides and sintering to achieve desired microstructure.

Due to the high strength and toughness of the Y-TZP ceramics, these materials potentially are of significant practical importance. Dispersion of Al_2O_3 in the Y-TZP [Tsuk85, Tsu87] improves high-temperature strength of these materials in bulk form. Based on these data, it appears reasonable that fibers prepared from these materials will exhibit improved high-temperature performance compared to fibers that are commercially available.

Rheological properties of colloidal ZrO_2 sols have not been studied previously. Factors affecting spinnability of the sol, such as sol concentration, aging and additives,

must be investigated to establish appropriate processing conditions for fiber spinning. A few studies on the rheological properties of sols have been made in relation to spinnability, but the reported shear flow behaviors of spinnable sols do not agree [Sac86, Koz88]. Although the flow occurring during fiber spinning has an elongational component, shear viscosity is used as a measure of spinnability due to the difficulty in measuring elongational viscosity. However, experimentally determined spinnability depends on the testing methods which cause different flow conditions.

There are many investigations reported in the literature regarding the microstructure of the Y-TZP ceramics. Although all studies have been made using only bulk ZrO_2 ceramics, the microstructural information available on the bulk ceramics can be useful in understanding the fiber microstructures. The grain growth of ZrO_2, particularly on the surfaces of the Y-TZP/Al_2O_3 fibers, is an important phenomena influencing the mechanical properties as well as the long-term thermal stability of the polycrystalline oxide fibers.

The objectives of this study were to

1) select a suitable precursor system capable of yielding the Y-TZP/Al_2O_3 fibers;

2) investigate the rheological behavior of the colloidal ZrO_2 sols with respect to Y_2O_3 and Al_2O_3 precursors combined with a polymer additive in an attempt to relate this behavior to the spinnability of the sols;

3) examine the effects of Al_2O_3 precursor addition on the thermal behavior, including calcination, densification and microstructural evolution during processing; and

4) study the effect of Y_2O_3 and Al_2O_3 additives on the thermal stability of the fibers.

The accomplishments of this study are

1) spinnable sols containing colloidal ZrO_2, yttrium and aluminum precursors and PVA were prepared and discontinuous fibers with diameters ranging from 5-15 μm were fabricated. The presence of PVA is a required but not sufficient condition for achieving spinnability with the colloidal ZrO_2 sols. In addition, the molecular weight and degree of hydrolysis of the PVA are important factors;

2) shear viscosities were measured and related to spinnability. Only those sols with viscosities in the range of $1\text{-}6x10^4$ mPa·s were spinnable using centrifugal spinning;

3) heating at temperatures of up to 1500°C resulted in fibers having composite microstructures with >99% relative density. These microstructures consist of elongated Al_2O_3 grains dispersed in a fine-grained tetragonal ZrO_2 matrix. Addition of 15 wt% Al_2O_3 inhibits grain growth of ZrO_2 on the fiber surfaces at temperatures up to 1400°C. Above this, Al_2O_3 is less effective due to its own coarsening; and

4) alumina addition enhanced the high-temperature microstructural stability of the fibers with respect to abnormal or exaggrated grain growth of ZrO_2. Large cubic

ZrO_2 grains were found on the Y-TZP fiber surfaces tested above 1400°C, but not on the Y-TZP/Al_2O_3 fiber surfaces tested under identical conditions.

The present research included the fabrication of discontinuous fibers using centrifugal spinning on a small scale. Fibers made in this fashion are approximately 0.1-1 cm in length and are curled. Although not the aim of this research, several attempts were made to produce continuous fibers from the Y-TZP/Al_2O_3 sols. Preliminary results from these first runs indicate that continuous fibers can be made, but "fine-tuning" of the sol system will be required to fabricate fibers suitable for use in high performance composites.

CHAPTER IV
EXPERIMENTAL PROCEDURE

Starting Materials

A commercial colloidal sol[a] was used as a source of ZrO_2. The ZrO_2 sol is an aqueous sol containing 20 wt% of ultrafine ZrO_2 particles with size ranging from 5 to 10 nm and dispersed with acetic acid. The characteristics of the ZrO_2 sol are listed in Table 4.1. Table 4.2 lists the typical chemical analysis of the ZrO_2 sol.

As sources of a stabilizing oxide and Al_2O_3, 99.9% pure yttrium nitrate[b] ($Y(NO_3)_3 \cdot 6H_2O$) and certified ACS grade aluminum nitrate[c] ($Al(NO_3)_3 \cdot 9H_2O$) were used, respectively. In addition, poly(vinyl alcohol)[d] (PVA) with different molecular weights was used to control viscosity and to aid in fiber spinning.

The weight fractions of oxides in the ZrO_2 sol and the nitrates were determined by calcining known amounts of the materials in Al_2O_3 crucibles at 1200°C for 4 hours in air. The crucibles were transferred from the furnace to a desiccator and weighed

---

[a]Nyacol Products Inc., Ashland, MA.

[b]Alfa Products, Danvers, MA.

[c]Fisher Scientific, Fair Lawn, NJ.

[d]Scientific Polymer Products, Inc., Ontario, NY.
Air Products and Chemicals, Inc., Allentown, PA.

TABLE 4.1

Characteristics of Zirconia Sol*

	Acetate Stabilized
weight %	20
Particle Size (nm)	5-10
Particle Charge	+
Acetate Content (mole/mole)	1.5 Acetate
pH	3.5
Specific Gravity	1.26
Viscosity (mPa·s)	10

* Data from Nyacol Zirconia, Nyacol Products Inc., Ashland, MA.

TABLE 4.2

Typical Analysis of Zirconia Sol*

Oxide	Amount
ZrO_2	20 wt%
Al_2O_3	<10 ppm
CaO	<20 ppm
MgO	<10 ppm
Fe_2O_3	<10 ppm
SiO_2	<200ppm
Na_2O	100-300 ppm

* Data from Nyacol Products, Inc., Ashland, MA.

immediately after the crucibles were cooled to room temperature. The weight fraction of oxide was obtained from the weight of the calcined material divided by the initial weight of the material.

Fiber Fabrication

Sol Preparation

Procedures for preparing Y-TZP and Y-TZP/Al_2O_3 fibers are illustrated in Figure 4.1.

The ZrO_2 sols contained the Y_2O_3 and the Al_2O_3 precursors equivalent to 2 or 3 mol% Y_2O_3 and from 0 to 20 wt% Al_2O_3, respectively. The amount of polymer added to the sol is 2 wt%, based on the total oxide contents. The majority of samples used in this study contained 3 mole% Y_2O_3, various amounts of Al_2O_3 and 2 wt% PVA with 2,000 molecular weight.

A mixture of the ZrO_2 sol and the additives was prepared by dissolving appropriate amounts of yttrium and aluminum nitrates in the sol while stirring. Once the nitrates were dissolved and the sol was preheated to 50°C, PVA was added. After the polymer was completely dissolved, the sol mixture was cooled to room temperature and filtered through No. 42 "Whatman" filter paper. The resulting sol mixture was concentrated by evaporating the sol heated to 40°C under reduced pressure in order to obtain the desired concentration. The evaporated water was collected in a cold trap cooled by liquid nitrogen. The sol concentration was

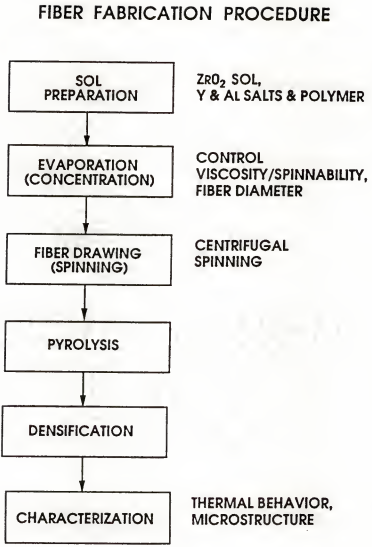

Figure 4.1. Processing flow diagram for preparation of Y-TZP/Al_2O_3 fibers.

determined based on the evaporated volume. For example, 60% of reduced volume indicates that 60 ml of water have been removed from the 100 ml of the original sol.

Fiber Spinning

After sols were concentrated to the desired concentrations, spinnability was tested by rod-pulling and centrifugal spinning methods. Spinnability was determined when the viscosity of the sol reached a point where the sol could be drawn into long fibers at least 1 meter by pulling a rod dipped in the sol or into discontinuous fibers by centrifugal force.

Fiber samples used for charaterization were prepared by centrifugal spinning at room temperature. Centrifugal spinning is a fiber forming process in which a viscous sol is projected from a small orifice by centrifugal force. This method results in discontinuous fibers with relatively small diameters. Centrifugal spinning produces quantities of the fibers large enough to allow for various characterization techniques to be used.

The sol was transferred to a container having an orifice with a 1 mm diameter and rotated by a high torque stirring motor[e] at variable speeds of up to 2,000 rpm. The rotating speed was adjusted, depending on the viscosities of the sols. The length of spun fibers ranged from a few millimeters to a centimeter. The majority of the fibers dried at room temperature had diameters varying from 5 to 15 μm. However, there were a few shots (droplets of gels) and very large diameter fibers formed during

[e]Caframo RZR50, Wiarton, ONT., Canada. Distributed by Fisher Scientific.

initial fiber spinning. The spun fibers were collected in the bottom of a glass container and were stored in an oven at 35°C and 5% relative humidity.

Heat Treatments

The dried fibers were stacked in a high purity (99.8%) Al_2O_3 combustion boat and calcined in a furnace[f] under steadily flowing air at a heating rate of 1°C/min up to 800°C and held for 2 hours. The color of the calcined fibers varied from white to slightly tan as the amount of the Al_2O_3 precursor was increased, indicating incomplete calcination. The calcined fibers were stored in a desiccator until further heat treatments.

A portion of the calcined fibers was placed in an Al_2O_3 boat made from a porous high purity Al_2O_3 (>99.8%) refractory brick and fired[g] to 1000°C in air at a heating rate of 3°C/min prior to final densification. At this temperature, the residual carbon materials were completely removed. The firing was continued in the same furnace up to 1500°C at a heating rate of 5°C/min for the density measurements or 20°C/min for the grain size measurements. The samples were cooled in the furnace and stored in a disiccator.

For the study of the thermal stability of the fibers, the calcined samples were fired at heating rate of 20°C/min and held at 1400°C for up to 24 hours and at 1500°C for up to 6 hours, respectively, and then cooled to room temperature for analyses.

---

[f]Lindberg, Watertown, WI.

[g]Deltech, Inc., Denver, CO.

Typical micrographs of the fibers drawn by centrifugal spinning and heat treated are shown in Figure 4.2. The Y-TZP fibers containing 3 mol% Y_2O_3 dried at room temperature and the Y-TZP/Al_2O_3 fibers containing 2 mol% Y_2O_3 and 10 wt% Al_2O_3 fired at 1200°C for 1 hour both exhibit uniform diameters and smooth surfaces. For the measurements of ZrO_2 crystallite sizes, the fibers containing 3 mol% Y_2O_3 and from 0 to 15 wt% Al_2O_3 were heated[f] in flowing air at a rate of 1°C/min up to 500°C, then at a rate of 3°C/min up to 1200°C for 1 hour. The samples then were furnace cooled. The sample containing 3 mol% Y_2O_3 and 20 wt% Al_2O_3 was obtained from a gel which had been prepared by evaporating a sol slowly in an oven at 35°C and 5% relative humidity.

Characterization

Infrared Spectroscopy

A Fourier transform infrared (FT-IR) spectrometer[h] was used to examine the sol and the fiber samples.

Transmission spectra were obtained from the sols using a liquid cell[i] with a ZnSe crystal which gives a transmission range useful from 4000 to 600 cm^{-1}. The spectra were obtained in a nitrogen atmosphere with 32 accumulation scans. A few measurements were made using a demountable cell suitable for a very small quantity of the sol (0.1 to 1 ml). A drop of the sol was placed between CdTe crystal plates

---

[h]Nicolet 20SXB FT-IR spectrometer, Nicolet Analytical Instruments, Medison, WI.

[i]A Circle Cell™, Spectra Tech Inc., Stamford, CT.

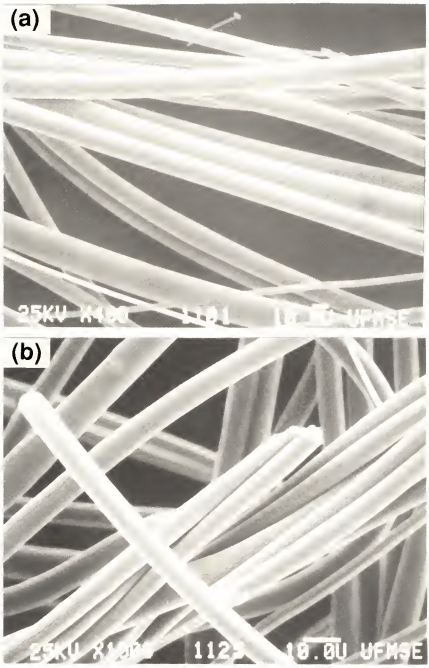

Figure 4.2. Typical micrographs of (a) Y-TZP fibers containing 3 mol% Y_2O_3 drawn by centrifugal spinning and dired at room temperature and (b) Y-TZP/Al_2O_3 fibers containing 2 mol% Y_2O_3 and 10 wt% Al_2O_3 fired at 1200°C for 1 hour.

and the cell was reassembled. A spacer of 0.05 mm thickness was placed between the two crystal plates to obtain a fixed path length. The transmission range of the CdTe crystal is 4000-400 cm^{-1}.

Transmission spectra also were obtained from the fiber samples using a DRIFT[j] accessary and 32 accumulation scans in a nitrogen atmosphere. The fibers dried at 80°C were ground in a diamonite mortar and pestle. Two wt% of the powder sample were mixed with dry KBr powder and packed in a sample holder. The range of the measured spectra was from 4000 to 400 cm^{-1}.

Rheological Measurements

The flow characteristics of the sols were determined using a cone and plate viscometer[k] at 25°C. The cone and plate viscometer has a fixed range of rotation speeds (rpm) and interchangeable cone spindles with different geometries which allow the sols to be measured through a wide range of viscosities and shear rates. For the sols with low viscosities ($<10^3$ mPa·s), the LVTD viscometer was used with spindles CP-40, 41 and 42 and at a shear rate ranging from 1.15 to 450 sec^{-1}. For the sols with high viscosities ($>10^3$ mPa·s), the HBT viscometer was used with spindles CP-51 and 52 and at a shear rate ranging from 1 to 384 sec^{-1}. The volume of the sol used in the

[j]Diffuse Reflectance Stage, Spectra Tech Inc, Stamford, CT.

[k]Model LVTD & HBT viscometers, Brookfield Engineering Laboratories, Inc., Stoughton, MA.

viscometers is varied from 2 to 0.5 ml depending on the type of spindle. The measurement was repeated at least twice by changing the sample after each run.

The viscosity (η) with respect to shear rate ($\dot{\gamma}$) was measured by changing the rotation speed of the cone every one minute. Readings were taken in order of increasing and decreasing the rotation speed and converted to viscosity (η) in mPa·s.

The viscosities of the sols with respect to reduced volume and aging time were obtained from the values of viscosities measured at fixed shear rates. The viscosities measured at shear rates of 60, 12 with the LVTD viscometer and 38.4 sec^{-1} with the HBT viscometer were used for the sols which had been evaporated to less than 30%, between 30 and 50%, and greater than 50% from their original sol, respectively.

To further examine the flow behavior of the spinnable sols, a concentric cylinder viscometer[l] was used. Steady rotational flow curves for shear stress versus shear rate were obtained by increasing the shear rate from zero to the maximum desired value in two minutes, followed by decreasing the shear rate in two minutes.

Thermal Analysis

Thermal behavior of the gels and the spun fibers was studied using differential thermal analysis[m] (DTA), thermogravimetric analysis[m,n] (TGA) and differential scanning calorimetry[n] (DSC). For TGA and DTA of the spun fibers and aluminum

---

[l]Model RV/100/CV100, Haake Buchler, Inc., Saddle Brook, NJ.

[m]Model STA-409, Netzsch Inc., Exton, PA.

[n]TGA 951 and DSC 910, Du Pont de Nemours & Co., Wilmington, DE.

nitrate, samples were ground, placed in an Al_2O_3 crucible and heated to 1500°C at a heating rate of 5°C/min. For TGA and DSC of ZrO_2 gels, ground samples were heated to 1100° and 600°C, respectively, at a heating rate of 10°C/min. All measurements were made in a static air atmosphere.

Phase Identification and Crystallite Size Measurements

Routine phase identification and ZrO_2 crystallite size measurements were performed using room-temperature X-ray powder diffraction[o] with CuKα radiation. The CuKα radiation was generated using a fine focus tube and a graphite monochromator at 40 KV and 20 mA. The samples of gels and fibers heat treated at various temperatures were crushed lightly using a diamonite mortar and pestle. Care was taken during crushing to prevent the possible stress-induced phase transformation of tetragonal to monoclinic ZrO_2 resulting from severe grinding. The powder sample was mounted on a glass slide using a mixture of collodion and amylacetate solution.

For phase identification, peaks between 20° and 80° 2θ were scanned at a scanning rate of 6° 2θ/min. The presence of monoclinic ZrO_2 is distinguished easily from the tetragonal ZrO_2 peaks in this scanning range. However, it is difficult to distinguish the cubic ZrO_2 peaks from the tetragonal ZrO_2 peaks because of overlapping of these peaks. To determine the presence of the cubic and the tetragonal phases, peaks in the range between 72° and 76° 2θ were examined closely using a

[o]Phillips ADP 3720 Automated powder diffractometer, Phillips Electronic Instruments, Eindhoven, Netherlands.

scanning rate of 0.5° 2θ/min. In this range, the peaks for both phases are separated. The phases were identified by the presence of the (400) and (004) tetragonal reflections and the (400) cubic reflection which exists between two tetragonal reflections.

The crystallite size of ZrO_2 was measured from the (111) tetragonal peak obtained by scanning between 28° and 34° 2θ at a scanning rate of 0.5° 2θ/min. The crystallite size was calculated using the Scherrer formula [Klu74]:

$$D = 0.9\lambda/\beta\cos\theta, \tag{4.1}$$

where D is the crystallite size, λ is the wavelength of CuKα radiation, β is the width of the diffraction peak at half its maximum intensity and θ is the Bragg angle. The β value was corrected using the (101) diffraction peak of α-quartz, which is close to the (111) tetragonal ZrO_2 reflection, as the standard peak in the Warren's formula [Klu74]:

$$\beta^2 = \beta_m^2 - \beta_s^2, \tag{4.2}$$

where β_m is the measured peak width of the unknown and β_s is the peak width of the standard. The peak positions, Bragg angles, were determined by measuring 2θ at the midpoint of a line drawn parallel to the background at half peak height. The measured peak positions were corrected using the least square linear regression analysis of $2\theta_{theoretical}$ versus $2\theta_{measured}$ for the silicon peaks obtained from high purity silicon

powder.[p] The peak widths of β_m and β_s were measured from the lines drawn at their half peak heights.

Electron Microscopy

Scanning electron microscopy[q] was used to study the microstructures of the fibers. The fibers were mounted onto double-side adhesive tape attached to a aluminum sample holder. A portion of the fibers were broken to expose the fractured surfaces. The mounted sample was sputter coated with gold and palladium of approximately 100 Å thickness to prevent charging in the microscope.

For the measurements of the ZrO_2 grain sizes, the mounted fibers were flattened by pressing slightly with a glass slide to insure that the horizontal fiber surfaces were the ones being examined. Scanning electron micrographs were taken randomly of each sample of the fibers.

For measuring the densities of the fibers, polished sections of the fibers were examined with the scanning electron microscope. The fibers were submerged in poly(methyl methacrylate) (PMMA) solution and polymerized at 60°C in an oven. The cured sample was ground with 600 grit silicon carbide abrasive paper until the fibers embedded in PMMA appeared. Polishing was continued progressively with diamond paste ranging from 6 to 0.1 μm on an automated polishing machine. Final polishing was done with an aqueous slurry of 0.05 μm Al_2O_3 powder. The polished

---

[p]99.999% pure Si powder, -325 mesh, Cerac Inc., Milwaukee, WI.

[q]JEOL JSM-35 CF Scanning Microscope, JEOL, Tokyo, Japan.

samples were sputter coated with gold and palladium. Some polished samples were analyzed with an energy dispersive X-ray microanalyzer.[r]

Analytical scanning transmission electron microscopy[s] and energy dispersive spectroscopy were used to investigate the ZrO_2/Al_2O_3 interface and phases present in the fibers.

Grain Size Measurements

The grain size of the ZrO_2 was measured using the line intercept method [Men69] on the micrographs showing surfaces of the fibers. The grain intercept lengths were measured by counting the number of grain boundaries intercepting a line superimposed on the enlarged photomicrographs. More than 150 grains were measured on the top surfaces of the fibers for each sample. This was accomplished using a digitizing tablet[t] and the arithmetic mean intercept length. The grain size was estimated from the grain intercept size multiplied by the factor 1.56 [Men69].

Density Measurements

Densities of the sintered fibers were determined by measuring porosities of the polished sections of the fibers using the point-counting method [Van84]. The fraction of pore volume was determined by counting numbers of pores at the intersection of

---

[r]JEOL 733 Electron Probe X-ray Microanalyzer, JEOL, Japan.

[s]JEOL ASTEM 200CX and 200FX, JEOL, Japan.

[t]Model 9111A, Hewlett Packard, CA.

the two crossed lines of a grid superimposed on the scanning electron micrographs. At least 20 fields were measured with a 25-point grid for each sample. The porosity was calculated within the 95% confidence intervals and converted to a relative density.

CHAPTER V
RESULTS AND DISCUSSION

Rheological Behavior of Zirconia-Based Sol

Rheological properties are of great importance in understanding the processing variables for fiber spinning. Although spinnability cannot be defined in terms of shear flow alone, shear viscosity is considered to be a useful measure of spinnability as discussed in Chapter 2. Factors affecting rheological properties of the ZrO_2-based sols were investigated by measuring shear viscosities. These included concentration, aging and spinning additives.

The sol[a] consists of the ZrO_2 particles ranging from 5 to 10 nm in size dispersed in water with acetic acid. The ZrO_2 particles have positive surface charges due to the adsorption of protons and are surrounded by counter acetate ions (CH_3COO^-). Although information about the preparation of the acetate-stabilized ZrO_2 sol is not available, the method is similar to that for the nitrate-stabilized ZrO_2 sol with small crystallites (<3 nm) developed at Oak Ridge National Laboratory [Bon88]. In that procedure, a dilute solution of zirconyl nitrate (0.2-0.5 M) is refluxed for 6 to 8 hours, boiled to dryness, and heated to 130-140°C. The friable powder ($ZrO_2 \cdot xH_2O$) is

[a]Data from Nyacol Zirconia, Nyacol Products Inc., Ashland, MA.

then dispersed in water to produce an acidic sol (pH=≈0) with ≈2 M ZrO_2 concentration and a nitrate/zirconia mole ratio of ≈1. This sol has properties essentially identical to those of a commercial nitrate-stabilized ZrO_2 sol[b].

Yttrium nitrate ($Y(NO_3)_3.6H_2O$) and aluminum nitrate ($Al(NO_3)_3.9H_2O$) are very soluble in the aqueous ZrO_2 sol. It is known that yttrium ions do not form hydroxides below pH=6 [Bae76]. In solutions less than pH=3, aluminum ions are not hydrolyzed but form complex polymeric species with only hydroxide and fluoride ligands [Bae76].

It was found that the addition of yttrium nitrate in an amount equivalent to 3 mol% Y_2O_3 to the ZrO_2 sol (pH=3.5) slightly changed the pH to 3.3, whereas the addition of aluminum nitrate in an amount equivalent to 10 wt% Al_2O_3 considerably reduced the pH to below 1.8. The large increase in acidity is attributed to water molecules which are coordinated to the small, highly charged, positive aluminum ions. These water molecules tend to lose protons by the probable reactions [Sis80]:

$$Al(NO_3)_3 + 6H_2O \rightarrow [Al(H_2O)_6]^{3+} + 3NO_3^- \text{ and} \quad (5.1)$$

$$[Al(H_2O)_6]^{3+} + H_2O \leftrightarrow [Al(H_2O)_5(OH)]^{2+} + H_3O^+. \quad (5.2)$$

Therefore, the formation of the hydroxides of yttrium and aluminum is not likely in the acidic ZrO_2 sol. Instead, hydrated metal ions exist, e. g., $[Al(H_2O)_6]^{3+}$. However, as water evaporates, the solubility of the nitrates changes to cause precipitation.

Poly(vinyl Alcohol) (PVA) is widely used as steric stabilizers and spinning additives in aqueous media. The PVA is prepared by hydrolysis of poly(vinyl acetate)

---

[b]Nyacol Products Inc., Ashland, MA.

and generally is not hydrolyzed completely. The PVA is considered a non-ionic polymer with a number of polar functional groups which are distributed along molecular chains and can be represented as

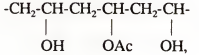

where OAc represents the acetate groups, CH_3COO-. Since the residual acetate groups in partially hydrolyzed PVA essentially are hydrophobic and weaken the intra- and intermolecular hydrogen bonding of adjoining hydroxyl groups, the presence of the residual acetate group enhances the solubility in water.

Concentration and Aging Effects

The effect of the addition of yttrium and aluminum nitrates on viscosity of the ZrO_2 sol is shown in Figure 5.1 as a function of reduced vol% (vol% of water removed by evaporation). The addition of a small amount of yttrium nitrate had little effect on the viscosity of the sol. The Z2Y sol containing yttrium nitrate (at a concentration level equivalent to 2 mol% Y_2O_3) exhibited the same viscosity change as the undoped ZrO_2 (ZS) sol. The Z3Y sol containing yttrium nitrate (in an amount equivalent to 3 mol% Y_2O_3) increased viscosity slightly as compared to the undoped ZrO_2 sol. The addition of aluminum nitrate (in an amount equivalent to 16.7 wt% Al_2O_3) to the Z2Y sol resulted in higher viscosity and a more rapid increase in viscosity.

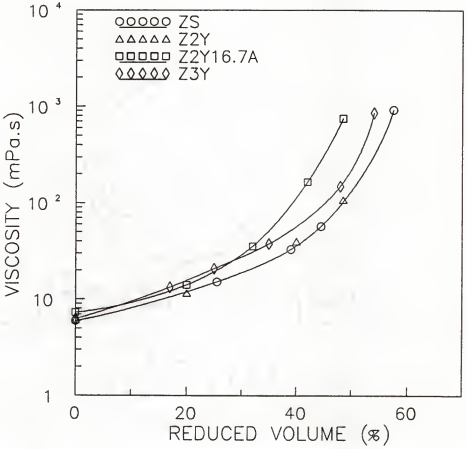

Figure 5.1. Plot of viscosity versus reduced vol% of zirconia sols containing yttrium and aluminum nitrates. ZS corresponds to the undoped sol, 2Y to 2 mol% Y_2O_3, 3Y to 3 mol% Y_2O_3, and 16.7A to 16.7 wt% Al_2O_3, respectively. The reduced vol% coincides to the vol% of evaporated water. The shear rates were 60, 12 and 38.4 sec^{-1} for sols with reduced volume less than 30%, between 30 and 50%, and greater than 50%, respectively.

Without spinning additives, evaporating water did not result in a substantial increase in viscosity. The viscosities of the sols in Figure 5.1 did not exceed 10^3 mPa·s. Attempts to remove more water caused the sols to be partially gelled and resulted in inhomogeneous sols. The removal of water by evaporation became increasingly difficult as concentration and viscosity increased for the sol containing aluminum nitrate. These sols could not be drawn into fibers using the experimentally designed spinning methods.

The addition of 2 wt% PVA (75% hydrolyzed) with low molecular weight (2,000 m.w.) allowed the sols to be concentrated to a highly viscous state without causing an abrupt gelation. Figure 5.2 shows a similar viscosity change for the sols containing PVA to that for the sols without PVA (Figure 5.1), but with a more rapid increase in viscosity at a higher concentration. The viscosity of the Z3Y2P sol containing yttrium nitrate (3 mol% Y_2O_3) and 2 wt% PVA exhibited a steady increase until the volume of the sol was reduced to 50%. The addition of the Al_2O_3 precursor (equivalent to 10 wt% Al_2O_3) (Z3Y10A2P sol) to the Z3Y2P sol resulted in a more rapid increase in viscosity than the Z3Y2P sol.

Although not shown in Figure 5.2, 2 wt% PVA (88% hydrolyzed) with high molecular weight (100,000 m.w.) increased viscosity to above 10^5 mPa·s when the volume of the sol containing the Y_2O_3 and Al_2O_3 precursors was reduced to 53%. The addition of 2 wt% PVA (88% hydrolyzed) with medium molecular weight (10,000 m.w.) did not increase viscosity to above 10^5 mPa·s. The viscosity of the sol containing the Y_2O_3 precursor and low molecular weight PVA (2,000 m.w.) was lower

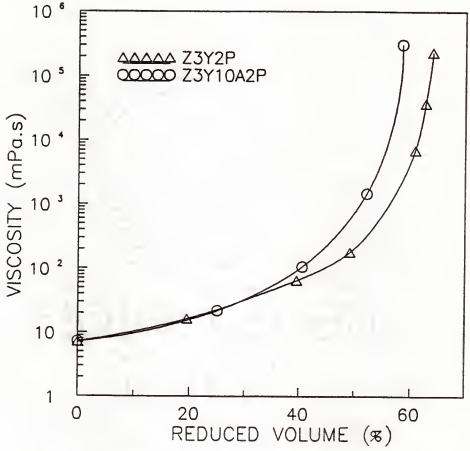

Figure 5.2. Plot of viscosity versus reduced vol% of zirconia sols with PVA. 3Y corresponds to 3 mol% Y_2O_3, 2P to 2 wt% PVA, and 10A to 10 wt% Al_2O_3, respectively. The shear rates were 60, 12 and 38.4 sec^{-1} for sols with reduced volume less than 30%, between 30 and 50%, and greater than 50%, respectively.

than when higher molecular weight PVA was added but increased to above 10^5 mPa·s after the sol volume was reduced to 40 vol%. The addition of PVA with molecular weight higher than 2,000 was found to make it more difficult to remove water by evaporation.

One of the most important properties of a sol is its stability over time. In general, a rapid increase in viscosity due to aging is not desirable for fiber spinning since it does not allow enough time for continuous spinning. However, an increase in viscosity should occur immediately after the sol is extruded from a spinneret. Otherwise, fiber shape cannot be retained. It is known that the viscosity of a polymerized sol such as a TEOS sol continuously increases during aging due to a progressive polymerization reaction which provides limited time for fiber spinning [Sakk82]. A colloidal sol such as an alkoxide-derived Al_2O_3 sol exhibits an increase in viscosity due to interparticle attraction when the sol approaches the gel. This behavior makes colloidal sols impratical for continuous spinning operations without use of polymer additives.

The sols used in this study were found to be stable at room temperature, as indicated by a negligible change in viscosity. Figure 5.3 shows the viscosity change with respect to aging time for the ZS, Z2Y and Z2Y16.7A sols containing no PVA. The sols were concentrated, kept in closed containers and aged at room temperature. The sols were very stable for up to 12 days. The nitrates in the Z2Y and Z2Y16.7A sols did not appreciably affect the viscosity of the sol.

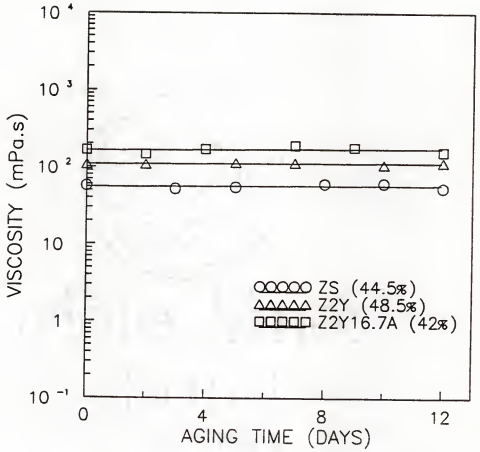

Figure 5.3. Plot of viscosity versus aging time for zirconia sols without PVA. The numbers in parentheses indicate the reduced vol% of the sols. The sols with the same compositions in Figure 5.1 were kept in closed containers and aged at room temperature. The shear rate was 12 sec^{-1}.

Figure 5.4 shows the viscosity for the concentrated Z3Y2P and Z3Y10A2P sols containing 2 wt% PVA (75% hydrolyzed) with 2,000 m.w. aged for up to 30 days under the same condition as in Figure 5.3. The addition of partially hydrolyzed PVA with low molecular weight did not change viscosities of spinnable sols noticeably. This can be attributed to the presence of bulky acetate groups in the partially hydrolyzed PVA, which impedes the close-packing of molecular chains, owing to spatial disturbance. The acetate groups reduce the interaction of the water molecules so that the viscosity increase is retarded. This finding is consistent with those reported by Toyoshima [Toy73]. He found that, although aging of an aqueous solution of PVA increases viscosity, these increases become smaller when more residual acetate groups exist in PVA.

Effect of Alumina Content on Spinnability

Spinnable sols were obtained by adding 2 wt% PVA (75% hydrolyzed) with 2,000 m.w. and by adjusting sol concentrations. Figure 5.5 shows viscosity of a spinnable Z2Y2P sol as a function of Al_2O_3 content at different reduced vol%. Since the sol viscosity increased with increasing aluminum nitrate content, less water (less reduced vol%) was removed to obtain spinnability. The sols from which fibers could be made by centrifugal spinning is designated as the "spinnable sols"[c] and the sols from which fibers could be made by pulling with a rod is designated as the "drawable sols"[c] in Figure 5.5.

[c]With the experimentally designed spinning methods.

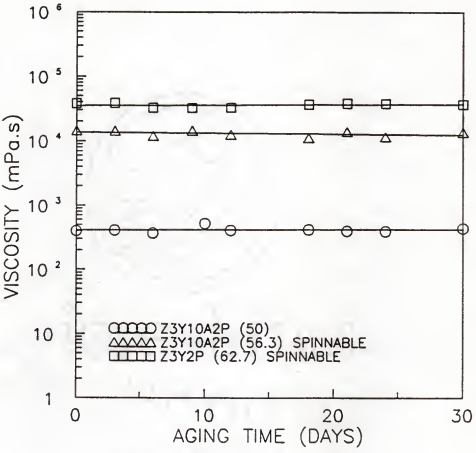

Figure 5.4. Plot of viscosity versus aging time for zirconia sols containing 2 wt% PVA. The numbers in parentheses indicate the reduced vol% of the sols. The sols with the same compositions in Figure 5.2 were kept in closed containers and aged at room temperature. The shear rates were 12 for Z3Y10A2P sol (50 reduced vol%) and 38.4 sec^{-1} for Z3Y10A2P (56.3 reduced vol%) and Z3Y2P (62.7 reduced vol%) sols, respectively.

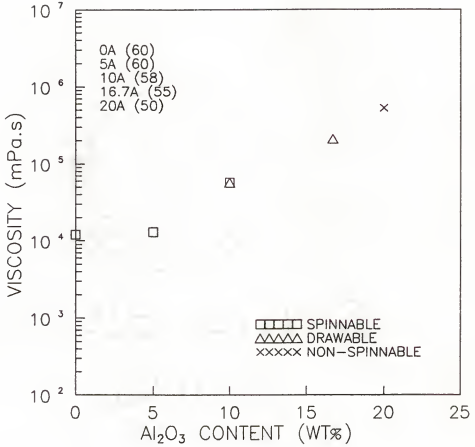

Figure 5.5. Plot of viscosity versus alumina content in zirconia sol containing yttrium nitrate (2 mol% Y_2O_3) and 2 wt% PVA. The spinnable and drawable sols were determined by centrifugal spinning and rod-pulling methods, respectively. The numbers in parentheses denote the reduced vol% of the sols. The shear rate was 38.4 sec^{-1}.

Centrifugal spinning required lower sol viscosities than the rod-pulling method. Fibers could be prepared by centrifugal spinning when the viscosities of the sols containing less than 16.7 wt% Al_2O_3 were in the range of $\approx 1\text{-}6 \times 10^4$ mPa·s. On the other hand, fibers could be drawn by the rod-pulling method at viscosities above 4×10^4 mPa·s. As shown in Figure 5.5, the sols containing aluminum nitrate in amounts equivalent to Al_2O_3 contents from 0 to 16.7 wt% became either spinnable or drawable upon volume reduction. The sol containing 10 wt% Al_2O_3 precursor showed excellent fiber forming capability with both methods when the viscosity reached 6×10^4 mPa·s. The sol containing 16.7 wt% Al_2O_3 precursor was only drawable by the rod-pulling method when viscosity reached 2×10^5 mPa·s. As the Al_2O_3 precursor content increased to greater than 16.7 wt% Al_2O_3, the sol lost its spinnability. The sol containing 20 wt% Al_2O_3 precursor could be neither drawn nor spun. Sols containing 3 mol% Y_2O_3 precursor were found to show similar spinnable viscosities to those for the sols containing 2 mol% Y_2O_3 precursor. A Z3Y2P sol with 60 reduced vol% became spinnable by centrifugal spinning at viscosities above 2×10^4 mPa·s.

The spinnability is attributed to the polymer additive which not only increases the sol viscosities to a range of optimum values for fiber spinning, but also provides a fluid thread strength to prevent a breakup from the capillary and cohesive fracture. It was observed that, when the sol viscosity was lower than the spinnable or drawable range, the capillary breakup mechanism dominated and the fluid thread broke into drops. When the sol viscosity was too high, the cohesive fracture mechanism

dominated and the highly viscous fluid thread broke in the course of spinning, followed by slow shrinkage of the broken ends (Chapter 2).

Effect of Shear on Viscosity of Spinnable Sol

The dependence of the viscosity on the shear rate for the Z3Y2P sol containing yttrium nitrate (3 mol% Y_2O_3) and PVA (2 wt%) is shown in Figure 5.6. The viscosities were measured with respect to shear rates using a cone and plate viscometer. No appreciable change in the viscosity with the shear rate was observed in the sols concentrated to a highly viscous state ($\eta > 10^5$ mPa·s). The sols appeared to behave as Newtonian fluids.

However, a narrow shear rate range used for each sol makes comparison of the flow behavior of the sols difficult. In order to determine if the sol exhibited any deviation from Newtonian flow, the flow curves in Figure 5.6 were replotted using the Casson equation. This equation is commonly used to represent the flow behavior of a flocculated suspension. Casson [Cas59] has derived the equation relating the shear stress τ to the shear rate $\dot{\gamma}$:

$$\tau^{1/2} = k_o + k_1\dot{\gamma}^{1/2}, \tag{5.3}$$

where k_o and k_1 are constant values. The constant k_o is a yield value of the suspension since k^2_o is the shear stress at the shear rate $\dot{\gamma} = 0$. For a non-Newtonian suspension, a plot of $\tau^{1/2}$ against $\dot{\gamma}^{1/2}$ gives a straight line with a non-zero intercept. For a Newtonian suspension, the plot gives a straight line passing through the origin. The

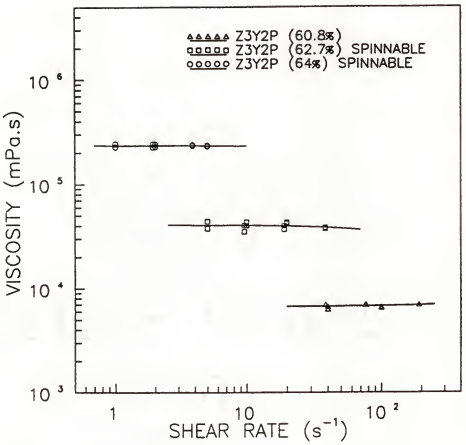

Figure 5.6. Plot of viscosity versus shear rate for zirconia sol without aluminum nitrate. The numbers in parentheses indicate the reduced vol% of the sol. The viscosity was measured with a cone and plate viscosmeter.

Casson plot in Figure 5.7 indicates that both spinnable and non-spinnable sols exhibit nearly Newtonian flow behavior.

The flow characteristics of the Z3Y10A2P sol containing yttrium nitrate (3 mol% Y_2O_3), aluminum nitrate (10 wt% Al_2O_3) and PVA (2 wt%) were determined using a wider range of shear rates with a concentric cylinder viscometer. The dependence of the viscosity on the shear rate for the sol is shown in Figure 5.8. The flow behavior of the sol progressively changes from nearly Newtonian to shear-thinning flow as the reduced vol% of the sol increases (i.e., sol becomes more concentrated). Figure 5.9 represents the viscosity as a function of shear rate and shear stress, showing only a small (if any) deviation from Newtonian behavior. The Casson plot for the sol in Figure 5.10 clearly indicates that the sols have yield values, suggesting that they are non-Newtonian.

The present study suggests that the flow behavior of the spinnable sols be described according to the shear rate conditions. The spinnable Z3Y2P sol showed Newtonian flow behavior when viscosities were measured using a narrow range of shear rates ($<100\ s^{-1}$). Similarly, Newtonian flow behavior for a spinnable TEOS sol has been reported by Kozuka et al. [Koz88] who used a narrow shear rate range to measure viscosities of the sol to a viscous state ($<\approx 10^4$ mPa·s) (see Figure 2.11 (a)). The Casson plot for the spinnable TEOS sols produced similar lines with zero intercepts (Newtonian behavior) to those for the spinnable Z3Y2P sols in Figure 5.7. Although not shown in Figure 5.10, Casson plot for the spinnable Z3Y10A2P sol (58.5 reduced vol%) having the same viscosities at shear rates $<10\ s^{-1}$ as those of the

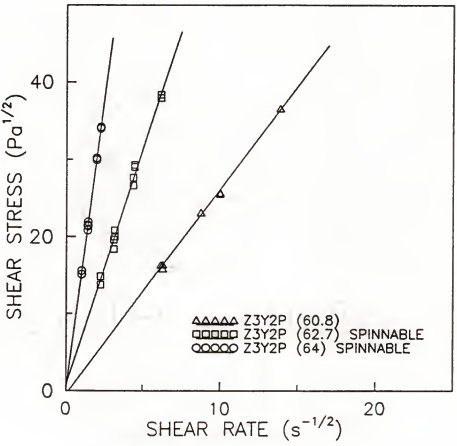

Figure 5.7. Casson plot of shear stress versus shear rate for zirconia sol without aluminum nitrate. The numbers in parentheses indicate the reduced vol% of the sol.

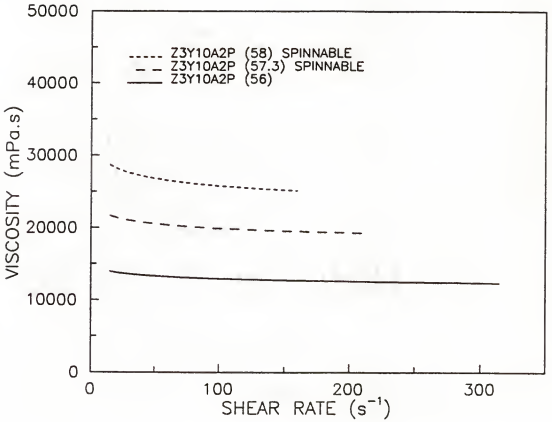

Figure 5.8. Plot of viscosity versus shear rate for zirconia sol containing aluminum nitrate. The viscosity was measured with a concentric cylinder viscometer. The numbers in parentheses indicate the reduced vol% of the sol. As the reduced volume of the sol increases (sol becomes more concentrated), the PVA content increases.

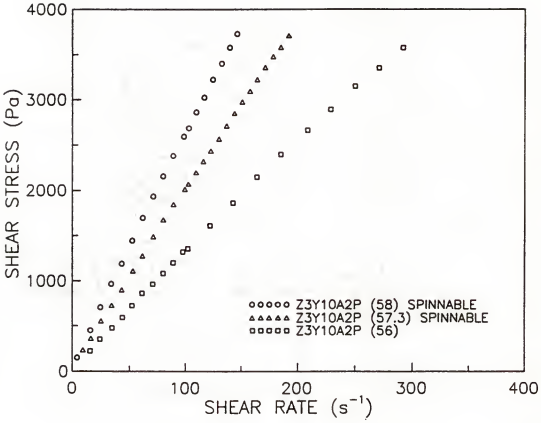

Figure 5.9. Plot of shear stress versus shear rate for zirconia sol containing aluminum nitrate.

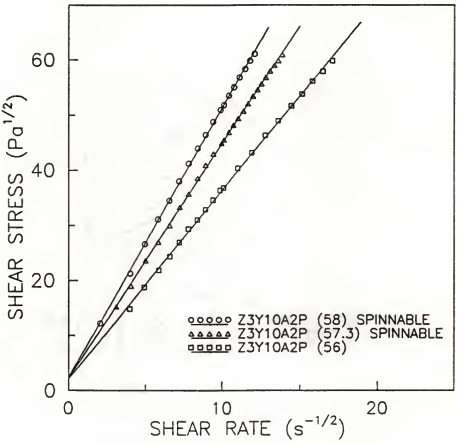

Figure 5.10. Casson plot of shear stress versus shear rate for zirconia sol containing aluminum nitrate. The numbers in parentheses indicate the reduced vol% of the sol. Data were taken from Figure 5.9.

spinnable Z3Y sol (64 reduced vol%) yielded a line with a zero intercept as in Figure 5.7. However, the spinnable Z3Y10A2P sol exhibited shear-thinning flow behavior in a wider shear rate region and yield values in the Casson plot. Sacks and Sheu [Sac86] have observed shear-thinning behavior of the spinnable TEOS sol when a wide shear rate range was used.

Sakka and coworkers [Sakk82, Mak88, Koz88, Sak88, Sakka88] have reported that spinnability can be obtained only from sols consisting of linear polymeric species (SiO_2 sol) or long-shaped particles (Al_2O_3 sol). However, the results of the rheological measurements showed that the spinnability of the colloidal ZrO_2-based sol can be achieved by adding an appropriate polymer regardless of the shape of the particles.

The PVA can influence the flow behavior of the spinnable sols since the polymer content increases with increasing the sols concentrations. Interactions between the polymer and other species in the sol may take place during the sol preparation. If the acetic acid in the ZrO_2 sol reacts with PVA, the hydroxyl groups in the PVA can be replaced with the acetate groups and more residual acetate groups are produced. In general, at high polymer concentration, entanglement between polymer molecules occurs and is broken as shear rate increases, resulting in shear-thinning. The shear effect decreases as the number of residual acetate groups in PVA increases, i.e., a small change in viscosity with respect to shear rate [Toy73]. This is due to less entanglement between the molecules. It is known that a definite chemical equilibrium between hydrolysis of poly(vinyl acetate) to form PVA and its reverse reaction exists, and at 40°C the equilibrium constant K is approximately unity according to [Nor73]

$$[PVAc][H_2O]/[PVA][HOAc] = K \approx 1, \quad (5.4)$$

where PVAc is poly(vinyl acetate) and HOAc is acetic acid. In concentrated sols, the reverse reaction of hydrolysis will be favored because, as the amount of water decreases during the evaporation process, the concentration of acetic acid increases. However, the presence of other precursors may further complicate the reaction.

Another factor possibly affecting the flow behavior is the oxidative degradation of PVA due to the aluminum nitrate dissolved in the sol. Degradation by oxidizing agents yields PVA molecules with either carboxyl (COOH) or carbonyl (C=O) end groups and several carbonyl side groups in each chain. Scission of chains can occur to lower molecular weights of polymers [Gulb73]. The degradation of PVA in nitric acid has been reported to produce oxalic acid [Marv38]. This reaction can lead to loss of spinnability of the sol.

FT-IR Analysis of Zirconia-Based Sols and Fibers

Figure 5.11 shows the infrared spectrum of the ZrO_2 sol stabilized with acetic acid. The major absorption peaks are identified in Table 5.1. Broad absorption bands of O-H stretching and bending vibrations, which arise from large amounts of water and acetic acid in the sol, make identification of the spectral bands difficult. A broad and strong absorption at 3400 cm^{-1} is due to O-H stretching vibrations of water and acetic acid. Weak C-H stretching bands are generally superimposed on the broad O-H band [Sil81]. Despite the presence of a large amount of acetic acid, a strong carbonyl (C=O) stretching vibration peak which is a characteristic of acetic acid and occurs at

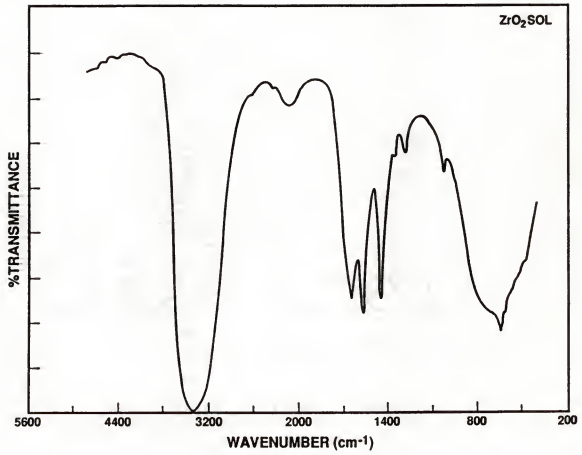

Figure 5.11. FT-IR spectra of zirconia sol stabilized with acetic acid.

TABLE 5.1

Infrared Peak Assignments for Zirconia Sol

Peak (cm^{-1})	Assignment*
3400	O-H Stretching (H_2O, CH_3COOH)
2960, 2870	C-H Stretching (CH_3COOH)
1653	O-H Bending (H_2O)
1572	$C(\dot{-}\!-O)_2^-$ Stretching (CH_3COO^-)
1450	O-H Bending (CH_3COOH) $C(\dot{-}\!-O)_2^-$ Stretching (CH_3COO^-)
1353	C-H Bending (CH_3COOH)
1281	C-O Stretching (CH_3COOH)
1027	O-H Bending (CH_3COOH)
713	O-H Bending (free OH)
650	$C(\dot{-}\!-O)_2^-$ Bending (CH_3COO^-)

* [Ros72, Sil81]

about 1760 to 1700 cm^{-1} is not seen in Figure 5.11. Instead, absorption peaks of acetate ions (CH_3COO^-) consisting of an asymmetrical $C(\overset{\cdots}{-}O)_2^-$ stretching peak at 1572 cm^{-1} and a symmetrical $C(\overset{\cdots}{-}O)_2^-$ stretching peak at 1450 cm^{-1} are observed. In addition, a peak at 650 cm^{-1} probably arising from a $C(\overset{\cdots}{-}O)_2^-$ bending vibration of hydrated zirconium acetates is observed [Ros72].

Figure 5.12 shows spectral changes for Z3Y2P sol and fibers containing yttrium nitrate (3 mol% Y_2O_3) and PVA (2 wt%). Figure 5.12 (a), (b) and (c) are the spectra of the dilute sol, the spinnable sol and the fibers dried at room temperature, respectively. The spectra of the dilute sol and the spinnable sol are very similar to those of the undoped ZrO_2 sol (Figure 5.11). As shown in Figure 5.12 (a) and (b), the sol does not reveal absorptions peaks characteristic of the Y_2O_3 precursor and PVA. As the sol is concentrated to a spinnable state, only slight intensity changes at 1350 and 1280 cm^{-1} occur. The intensity of the weak C-H bending peak at 1350 cm^{-1} is slightly increased, while the intensity of the weak C-O stretching peak at 1280 cm^{-1} is decreased.

The spectrum of the fibers in Figure 5.12 (c) exhibit the presence of PVA which is indicated by very weak C-H stretching peaks at 3016 and 2938 cm^{-1}. The C-H stretching absorption of PVA is generally stronger and occurs at higher frequencies than for those of acetate groups in acetic acid. A shoulder at 1730 cm^{-1} is indicative of the presence of the residual acetate group in PVA and ascribed to the carbonyl (C=O) stretching vibration. The $C(\overset{\cdots}{-}O)_2^-$ stretching peaks of acetate ions at 1558 and 1447 cm^{-1} in the sols remain in the fibers. Similar absorption peaks at 1530 and 1400

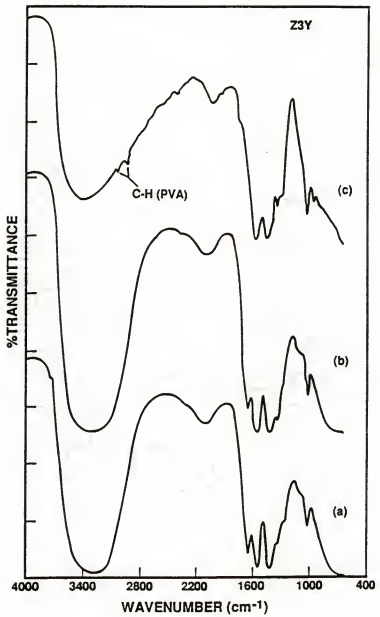

Figure 5.12. FT-IR spectra of zirconia sols and fibers containing yttrium nitrate (3 mol% Y_2O_3) and PVA (2 wt%). The spectra (a), (b) and (c) correspond to the sol without volume reduction, the sol with 60.8% of reduced volume, and the fibers dried at room temperature, respectively.

cm^{-1} corresponding to metal-bonded acetate have been reported in fibers prepared from zirconium acetate solutions [Ler84]. Although the peak at 950 cm^{-1} in the spectrum of the fibers is weak, it is stronger than that peak in the spectra of the sols and could arise from C-CH_3 bending vibration of metal acetates.

The addition of aluminum nitrate to the sol containing yttrium nitrate and PVA resulted in broadening of absorption bands between 1450 and 1300 cm^{-1}. Figure 5.13 shows spectral changes for the Z3Y10A2P sol and the fibers containing yttrium nitrate (3 mol% Y_2O_3), aluminum nitrate (10 wt% Al_2O_3) and PVA (2 wt%). Figure 5.13 (a), (b) and (c) are the spectra of the dilute sol, the spinnable sol and the fibers dried at room temperature, respectively. The nitrate ions resulting from the aluminum nitrate dissolved in the sol and coordinated water to the metal give rise to the broad bands between 1450 and 1300 cm^{-1} which become more profound in the fiber sample. A peak at 1380 cm^{-1} is assigned to the symmetrical and asymmetrical stretching vibration of nitrate ions [Nak70, Gad75]. Its absorption is increased as the sol concentration increases, as seen in the spectra of the fibers.

As compared with the spectrum of the fibers without the Al_2O_3 precursor in Figure 5.12 (c), the spectrum of the fibers containing the Al_2O_3 precursor in Figure 5.13 (c) exhibit no absorption bands of PVA and the residual acetate group in PVA. The very weak C-H stretching absorption peaks of PVA at 3016 and 2938 cm^{-1} and the carbonyl (C=O) peak occurring as a shoulder at 1730 cm^{-1} in the fibers without the Al_2O_3 precursor are not seen in the spectra of the fibers containing the Al_2O_3 precursor. This suggests that the degradation of PVA may have occurred in the sols

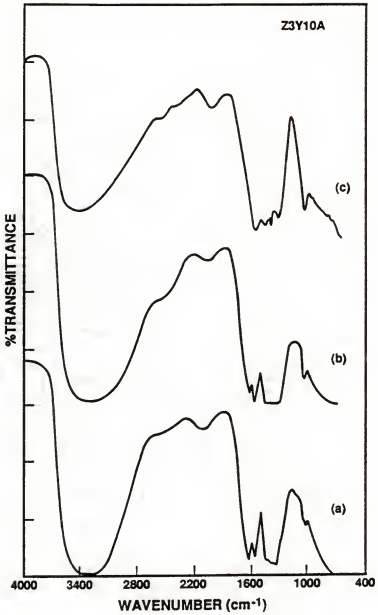

Figure 5.13. FT-IR spectra of zirconia sols and fibers containing yttrium nitrate (3 mol% Y_2O_3), aluminum nitrate (10 wt% Al_2O_3) and PVA (2 wt%). The spectra (a), (b) and (c) correspond to the sol without volume reduction, the sol with 60.3% of reduced volume, and the fibers dried at room temperature, respectively.

containing aluminum nitrate. Thus, the polymer degradation could account for the loss of spinnability of the sol containing a large amount of aluminum nitrate (20 wt% Al_2O_3).

The FT-IR results of the sols and the dried fibers did not give a clear indication that the reactions between PVA and other species had taken place during the sol preparation process because of a strong influence of hydroxyl and acetate groups. There appears to be no well-defined differences between the FT-IR spectra of the dilute sols and those of the concentrated spinnable sols. A strong influence of water and acetic acid resulted in poor distinction between the spectra of the dilute sol and the spinnable sol. Further work using either more sensitive FT-IR or other techniques such as nuclear magnetic resonance (NMR) spectroscopy is necessary to clearly understand chemical interactions between the ZrO_2 sol and the additives affecting rheological behavior and spinnability.

Thermal Behavior of Zirconia in Y-TZP/Al_2O_3 Fibers

Thermal Analysis

Thermal behavior of ZrO_2 gel is similar to that of ZrO_2 fibers drawn from zirconium acetate solution [Ler84] because of acetic acid in the ZrO_2 sol. The DSC and TGA curves of the ZrO_2 gel are presented in Figure 5.14. The DSC curve shows broad endothermic peaks up to 300°C corresponding to dehydration of the gel and decomposition of acetate. Sharp exothermic peaks at 370°C and 505°C are due to the oxidation of carbon compounds and the crystallization of ZrO_2, respectively. The gel

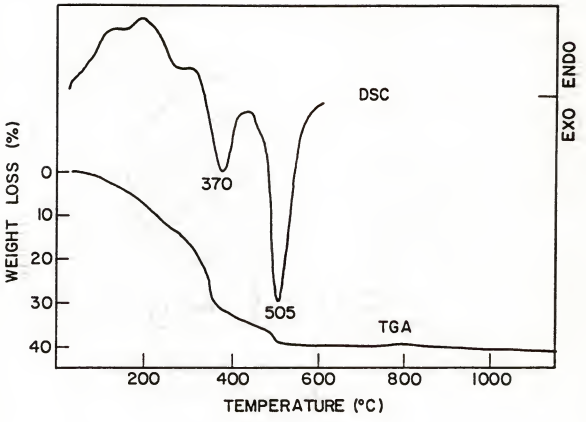

Figure 5.14. DSC and TGA curves of zirconia gel at a heating rate of 10°C/min in air.

sample exhibits a large weight loss of 39% up to 500°C and 41 wt% loss at 1100°C as shown in the TGA curve.

Osendi et al. [Ose85] have reported exothermic peaks at 344°C and 508°C from thermal decomposition of zirconyl acetate compound. They suggested that, at 344°C, carbon compounds resulting from decomposition of acetate are removed by consuming gaseous oxygen and lattice oxygen in the powder, creating oxygen deficient defects. At 508°C, the defects are eliminated by oxidation. The first exothermic peak at 344°C was attributed to the crystallization of tetragonal ZrO_2. However, the X-ray diffraction analysis of the ZrO_2 gel used in this study revealed that the ZrO_2 gel transforms to poorly crystallized oxide and hydroxide (X-ray amorphous) at 370°C and to well-crystallized tetragonal ZrO_2 at 500°C. Therefore, the strong exothermal effect at 505°C in Figure 5.14 is attributed to the crystallization of tetragonal ZrO_2. Such a strong exothermal effect is characteristic crystallization behavior of amorphous hydrous ZrO_2 to tetragonal ZrO_2 and is called a glow phenomenon [Liv68, Tor84].

The DTA and TGA curves of aluminum nitrate ($Al(NO_3)_3 \cdot 9H_2O$) are shown in Figure 5.15. The DTA curve exhibits two sharp endothermic peaks. The first endothermic peak at around 80°C is due to melting of the nitrate accompanied by no weight loss. The second endothermic peak at around 170°C is due to the decomposition of the nitrate accompanied by a large weight loss. Most weight loss arising from dehydration of aluminum hydroxide occurred up to 500°C and the final weight loss was 85%, which is close to the theoretical weight loss (86.4%) expected when the nitrate decomposes to the oxide.

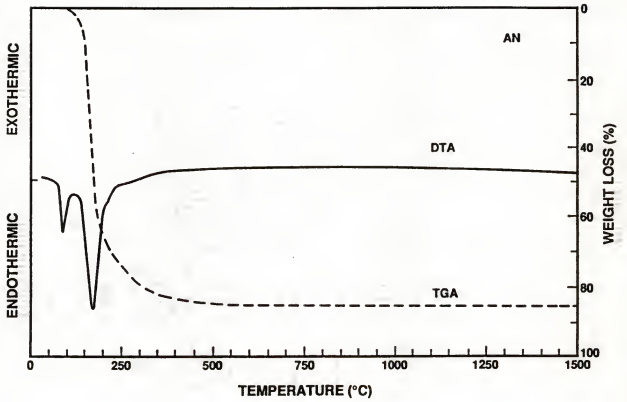

Figure 5.15. DTA and TGA curves of aluminum nitrate, $Al(NO_3)_3 \cdot 9H_2O$, at a heating rate of 5°C/min in air.

The thermal analysis of aluminum nitrate does not show any phase transition of Al_2O_3. However, existence of η-, θ- and α-Al_2O_3 after extended heat treatments of aluminum nitrate has been reported from X-ray diffraction analysis by Ciminelli [Cim83], who could not observe the phase transition with thermal analysis. Kuklina [Kuk73] has reported the appearance of α-Al_2O_3 at 900°C and stated that the low phase transition temperature of α-Al_2O_3 is attributed to the chemisorbed nitrate to the Al_2O_3 surface acting as a mineralizer.

The DTA and TGA curves of Z2Y and Z2Y16.7A gel samples are shown in Figure 5.16 (a) and (b), respectively. The Z2Y gel containing yttrium nitrate ($Y(NO_3)_3{\cdot}6H_2O$) (2 mol% Y_2O_3) and PVA (2 wt%) in Figure 5.16 (a) shows similar behavior to the ZrO_2 gel (Figure 5.14). Broad endothermic peaks are present due to the dehydration and decomposition of the gel up to 250°C and sharp exothermic peaks at 370° and 480°C exist due to the oxidation of residual carbons followed by the crystallization of the ZrO_2 gel. The crystallization temperature of the Z2Y sample is lower than that of the pure ZrO_2 due to different heating rates; 5°C/min for the Z2Y sample and 10°C/min for the ZrO_2 sample. In addition, a broad and weak exothermic peak occurring at 1375°C without a weight loss is observed. Most weight loss occurred below 600°C followed by a small weight loss at around 800°C due to the volatilization of residual carbons. The gel lost 43% of its weight up to 1500°C.

The DTA of the Z2Y16.7A gel containing yttrium nitrate (2 mol% Y_2O_3), aluminum nitrate (16.7 wt% Al_2O_3) and PVA (2 wt%) exhibits a broad endothermic peak at 170°C mainly due to the decomposition of aluminum nitrate and several

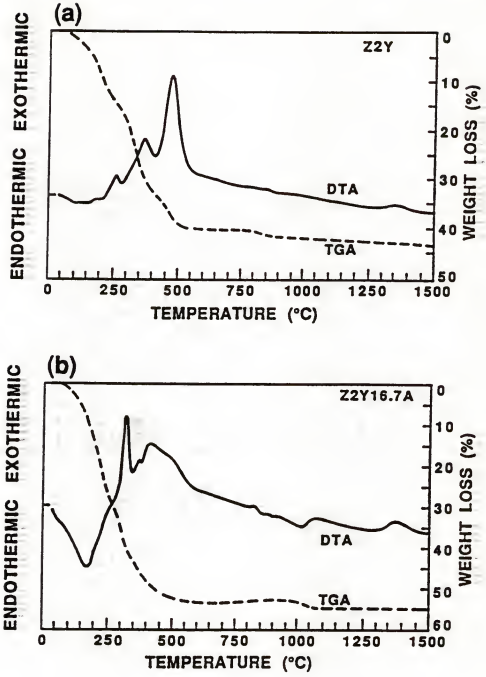

Figure 5.16. DTA and TGA curves of (a) Z2Y gel containing yttrium nitrate (2 mol% Y_2O_3) and PVA (2 wt%) and (b) Z2Y16.7A gel containing yttrium nitrate (2 mol% Y_2O_3), aluminum nitrate (16.7 wt% Al_2O_3) and PVA (2 wt%) at a heating rate of 5°C/min in air.

exothermic peaks between 300° and 550°C. In addition to an exothermic peak at 1000°C due to the volatilization of carbon residue accompanied by a small weight loss, the same exothermal effect at 1375°C as the Z2Y sample is observed. The gel lost more weight (55 wt%) at 1500°C than the Z2Y samples because of the presence of aluminum nitrate.

For comparison with Z2Y and Z2Y16.7A gel samples, the DTA and TGA curves of Z3Y and Z3Y15A fibers are shown in Figure 5.17 (a) and (b), respectively. The Z3Y fibers containing yttrium nitrate (3 mol% Y_2O_3) and PVA (2 wt%) shows the same thermal behavior as the Z2Y gel with the exception of a weak exothermic peak at 1370°C observed in the Z2Y gel. The weak exothermic peak at 1375°C in Figure 5.16 (a) and (b) coincides with the appearance of monoclinic ZrO_2 in the X-ray diffraction spectrum.

The thermal analysis of Z3Y15A fibers containing yttrium nitrate (3 mol% Y_2O_3), aluminum nitrate (15 wt% Al_2O_3) and PVA (2 wt%) does not show the same thermal behavior as the Z2Y16.7A gel with 2 wt% PVA. A sharp exothermal effect at 320°C and a broad and weak exothermal effect at 1375°C as seen in the Z2Y16.7A gel are not observed, whereas a sharp exothermic peak at 670°C accompanied by a small weight loss is observed. This may indicate that the removal of carbon compounds from acetate and PVA is easier in the fibers than gels because of large surface areas of the fibers.

The thermal analyses of the gel and fiber samples did not show clearly the thermal degradation of PVA and the decomposition of yttrium nitrate. The addition of

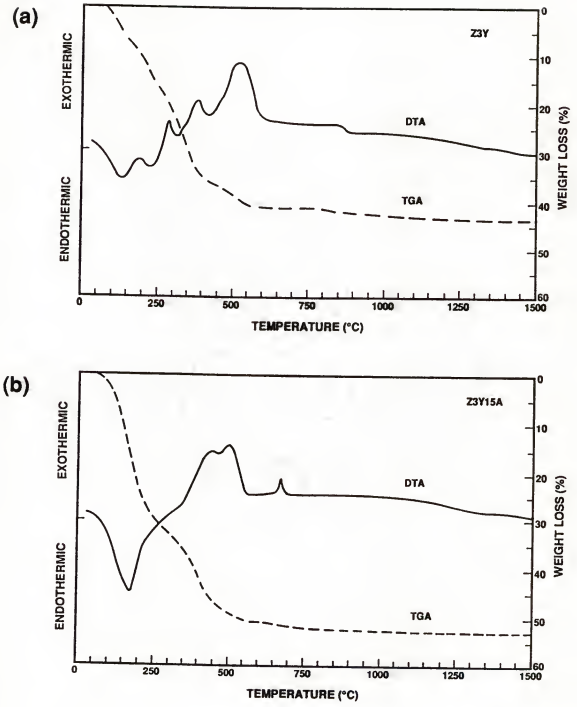

Figure 5.17. DTA and TGA curves of (a) Z3Y fibers containing yttrium nitrate (3 mol% Y_2O_3) and PVA (2 wt%) and (b) Z3Y15A fibers containing yttrium nitrate (3 mol% Y_2O_3), aluminum nitrate (15 wt% Al_2O_3) and PVA (2 wt%) at a heating rate of 5°C/min in air.

aluminum nitrate resulted in a more complex thermal behavior, as seen in the DTA curves of the sample containing aluminum nitrate. The DTA curves of Z2Y16.7A gel and Z3Y15A fiber samples suggest that the thermal behavior of the fibers is different from that of the bulk gel sample.

Phase Analysis

The pure ZrO_2 particles obtained from the thermal decomposition of the gel prepared from the acetate stabilized ZrO_2 sol is in metastable tetragonal phase which will transform to the monoclinic form as firing temperature is increased. In the Y-TZP and Y-TZP/Al_2O_3 fibers, ZrO_2 phases, including the tetragonal phase, are metastable since slow diffusion of cations at low sintering temperatures and short firing schedules do not allow the phases to reach equilibrium.

The effects of Y_2O_3 and Al_2O_3 additions on the stability of tetragonal ZrO_2 in Y-TZP fibers are shown in Table 5.2. The phases present in the Y-TZP and Y-TZP/Al_2O_3 fibers fired for 1 hour at various temperatures were identified with X-ray diffraction.

Well-crystallized tetragonal ZrO_2 was developed in all fibers at 1200°C. At 1400°C, the Y-TZP and Y-TZP/Al_2O_3 fibers containing 3 mol% Y_2O_3 showed tetragonal ZrO_2. On the other hand, a small amount of monoclinic ZrO_2, in addition to tetragonal ZrO_2, was found in the Y-TZP and Y-TZP/Al_2O_3 fibers containing 2 mol% Y_2O_3. This can arise from a change in the critical grain size of ZrO_2 with Y_2O_3 content. Lange [Lan82b] has reported in Y-TZP bulk ceramics that an increase in

TABLE 5.2

Phases Present in Y-TZP and Y-TZP/Al_2O_3 Fibers

Temperature(°C)	Z2Y*	Z2Y10A	Z3Y	Z3Y15A
900	T+	T	T	T
1200	T	T	T	T+(A)
1400	T+(M)	T+(M)+A	T	T+A

*2Y corresponds to 2 mol% Y_2O_3, 10A to 10 wt% Al_2O_3, 3Y to 3 mol% Y_2O_3, and 15A to 15 wt% Al_2O_3, respectively.

+T corresponds to tetragonal ZrO_2, M to monoclinic ZrO_2, A to α-Al_2O_3, and ( ) to a minor amount of phase, respectively.

critical transformation size of ZrO_2 with the addition of Y_2O_3 up to 3 mol% drastically increases the amount of metastable tetragonal ZrO_2 phase.

The X-ray diffraction spectra of the fibers did not exhibit the presence of any transition Al_2O_3, presumably due to a small crystallite size of the Al_2O_3 phase. At 1400°C, α-Al_2O_3 appeared in the Y-TZP/Al_2O_3 fibers with the exception of the Z3Y15A fibers which exhibited α-Al_2O_3 at 1200°C.

Figure 5.18 shows X-ray diffraction patterns of the Y-TZP/Al_2O_3 fibers fired at 1400°C. The monoclinic peaks are shown in the Y-TZP/Al_2O_3 fibers containing 2 mol% Y_2O_3 (Z2Y16.7A). The weak exothermic peak at 1370°C in the thermal analyses of both Z2Y and Z2Y16.7A samples (Figure 5.16) indicates that the transformation of metastable tetragonal to monoclinic phase occurred during heating. However, tetragonal ZrO_2 may also have transformed to the monoclinic form during cooling or grinding in sample preparation for X-ray diffraction. Consistent with these results are those reported by Kagawa et al. [Kag84] for a similar system. They found some conversion of tetragonal to monoclinic ZrO_2 in a powder mixture of Al_2O_3 and ZrO_2 prepared by inductively coupled plasma (ICP) spraying after heating to 1380°C.

The results of X-ray diffraction analysis indicate that the addition of Al_2O_3 is not effective in suppressing the tetragonal to monoclinic transformation of ZrO_2 in the Y-TZP fibers containing 2 mol% Y_2O_3. Although the fibers containing 3 mol% Y_2O_3 retain 100% of tetragonal ZrO_2 after 1 hour sintering, it is expected that even prolonged sintering will not reduce the stability of the tetragonal phase. It has been reported by Hou et al. [Hou87] that the addition of 20 wt% Al_2O_3 to Y-TZP

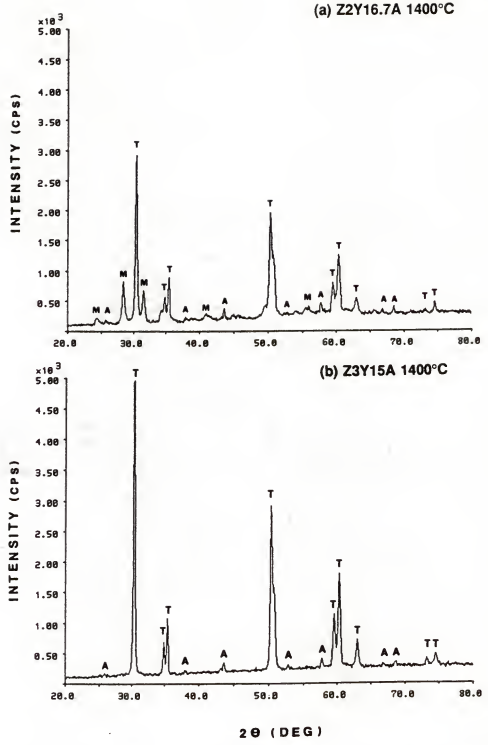

Figure 5.18. X-ray diffraction patterns of Y-TZP/Al_2O_3 fibers (a) containing 2 mol% Y_2O_3 and 16.7 wt% Al_2O_3 (Z2Y16.7A) and (b) containing 3 mol% Y_2O_3 and 15 wt% Al_2O_3 (Z3Y15A) fired at 1400°C for 1 hour in air. T,M and A correspond to tetragonal ZrO_2, monoclinic ZrO_2 and α-Al_2O_3, respectively.

containing 3 mol% Y_2O_3 significantly increases the amount of tetragonal ZrO_2 from 40% to 90% after sintering at 1600°C for 4 hours. Lange [Lan82a] suggested that an increase in elastic modulus of the composite matrix will increase the critical transformation size of ZrO_2 particle and retain more tetragonal phase, thus increasing toughness and strength.

Effect of Alumina on Growth of Zirconia Crystallites

Table 5.3 lists the phases present in Y-TZP fibers containing 3 mol% Y_2O_3 and 0 to 20 wt% Al_2O_3 and fired up to 1200°C for 1 hour in air. The sample containing 20 wt% Al_2O_3 was obtained from bulk gel since fibers could not be drawn. No monoclinic ZrO_2 phase was observed in the samples. Due to the line broadening effect of small ZrO_2 crystallite sizes on the X-ray diffraction peaks, all tetragonal ZrO_2 peaks could not be resolved: the well-resolved (400) and (004) tetragonal peaks in the range between 72° and 76° (2θ) were obtained from the samples containing 0 to 5 wt% Al_2O_3 at 900°C. On the other hand, these tetragonal peaks were not observed in the sample containing 10 wt% Al_2O_3 until 1000°C and the samples containing 15 and 20 wt% Al_2O_3 until 1100°C, respectively. Below these temperatures, a broad peak corresponding to tetragonal ZrO_2 was observed. The α-Al_2O_3 was detected in the fibers containing greater than 10 wt% Al_2O_3 at 1200°C.

The effect of Al_2O_3 on growth of tetragonal ZrO_2 crystallites is shown in Figure 5.19, suggesting that the addition of Al_2O_3 retards the growth of ZrO_2 crystallites at temperatures ranging up to 1200°C. As the Al_2O_3 content increased, the

TABLE 5.3

Phases Present in Y-TZP Fibers Containing 3 mol% Y_2O_3 and Various Amounts of Alumina.

Temperature (°C)	Al_2O_3 Content (wt%)[+]				
	0	5	10	15	20[#]
600	T*	T*	T*	T*	T*
700	T*	T*	T*	T*	T*
800	T*	T*	T*	T*	T*
900	T	T	T*	T*	T*
1000	T	T	T	T*	T*
1100	T	T	T	T	T
1200	T	T	T+(A)[†]	T+(A)	T+A

[+] Vol% of 5, 10, 15, and 20 wt% Al_2O_3 is 7.5, 14.5, 21.3, and 27.7%, respectively.

[#] Sample containing 20 wt% Al_2O_3 was prepared from dried gel.

[*] indicates tetragonal ZrO_2 phase of which all X-ray diffraction peaks are not well-resolved.

[†] A corresponds to α-Al_2O_3 and ( ) to a minor amount of phase, respectively.

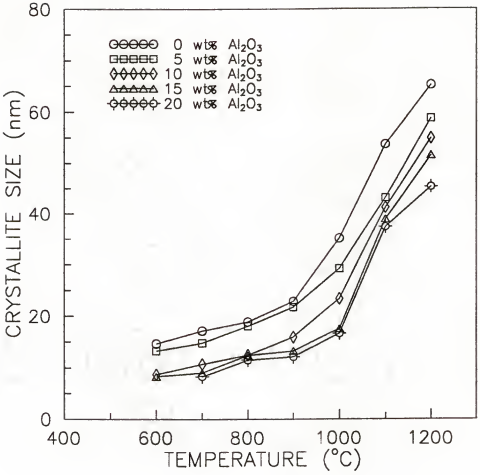

Figure 5.19. Crystallite size of tetragonal zirconia in Y-TZP fibers containing 3 mol% Y_2O_3 and various amounts of alumina.

ZrO_2 crystallite size became smaller, resulting in decreases in intensity and broadening of the tetragonal ZrO_2 peaks. This is demonstrated in Figure 5.20, showing decreasing intensities and broadening of two tetragonal peaks corresponding to (111) and (200) plus (002) reflections with increasing Al_2O_3 content in the Y-TZP samples fired at 700°C.

The temperature dependence of ZrO_2 growth in the fiber samples can be seen from an Arrhenius plot of crystallite size versus reciprocal absolute temperature. As shown in Figure 5.21, a distinct change in the slope of the curve at approximately 900°C is indicative of a change in the growth mechanisms.

At temperatures below 900°C, the curves have approximately the same slope. The thermal decomposition of precursors and removal of volatiles in the fibers result in highly porous and very fine crystallite aggregates. A steady increase in crystallite size in this temperature region is attributed to the growth of crystallites within these small aggregates. At this stage, the aggregates are densified into single crystallites. Van de Graaf et al. [van85] have found the same temperature dependence of grain growth in the bulk compact of ultrafine Y_2O_3-stabilized ZrO_2 powder prepared by hydrolysis of a mixed solution of alkoxides.

The addition of alumina greater than 10 wt% (14.5 vol%) became effective in preventing the growth of ZrO_2 crystallites (≤≈900°C). The retardation of ZrO_2 crystallite growth by coexisting Al_2O_3 particles can be attributed to the intimate mixing of the two-phase materials. Murase et al. [Mur86] have reported the retardation of ZrO_2 crystallite growth in an ultrafine powder mixture of unstabilized ZrO_2 and Al_2O_3

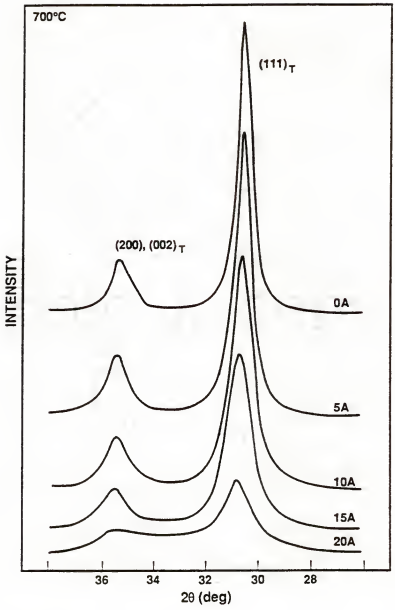

Figure 5.20. Effect of alumina on intensities of X-ray diffraction patterns of Y-TZP/Al_2O_3 samples fired at 700°C.

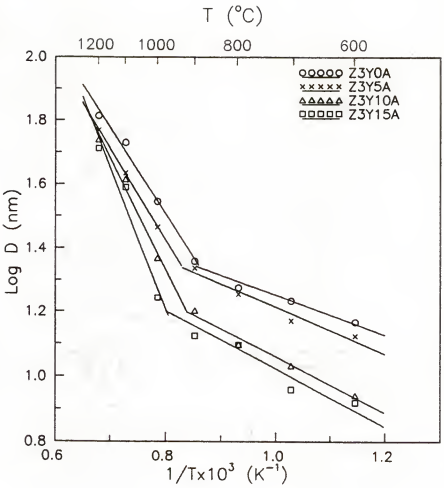

Figure 5.21. Temperature dependence of crystallite size of tetragonal zirconia in Y-TZP/Al_2O_3 fibers.

(>10 vol% Al_2O_3) prepared from ZrO_2 sols containing aluminum sulfate. In contrast, they found that mechanically mixed powders exhibit the same crystallite growth as observed in powder containing 0% Al_2O_3. Thus, mixtures of ZrO_2 and Al_2O_3 prepared by chemical methods yield different results than those prepared by mechanical mixing.

At temperatures above 900°C, the growth of ZrO_2 crystallites occurred more rapidly and was enhanced with increasing Al_2O_3 content, as shown by changes in the slopes of the curves. However, the crystallite sizes of ZrO_2 in the fibers containing Al_2O_3 were still smaller than those in the fiber containing no Al_2O_3. A rapid increase in crystallite size has been observed in pure ZrO_2 particles derived from zirconyl acetate at temperatures between 900° and 1100°C [Ose85].

The increased temperature dependence on ZrO_2 crystallite growth in the fibers containing Al_2O_3 is considered to be due to the coupled grain growth effect [Pug86]. The coupled grain growth between two oxides can occur in two ways. One is that the growth of one phase is contingent on the growth of the other. The other effect is that the phase transformation in one phase simultaneously allows the grains of the other phase to coarsen more rapidly.

Pugar and Morgan [Pug86] have found in Al_2O_3 containing 10 vol% ZrO_2 prepared by air-hydrolyzing a mixture of aluminum and zirconium alkoxides that the growth of ZrO_2 crystallites is coupled to the $\gamma \rightarrow \alpha$ phase transformation of Al_2O_3. The rapid growth of ZrO_2 started at 850°C where α-Al_2O_3 appeared and ceased when total conversion of α-Al_2O_3 occurred at 1100°C. The reconstructive transition of $\gamma \rightarrow \alpha$-$Al_2O_3$ apparently allows the simultaneous growth of ZrO_2 to occur, comparable to the

growth of molybdenum metal particles during this transformation in a transitional Al_2O_3 matrix [Morr84]. The present data show a rapid increase in ZrO_2 crystallite size at approximately 900°C, although the $\gamma \rightarrow \alpha$-$Al_2O_3$ transition was not observed until 1200°C.

Microstructural Characterization of Y-TZP/Al_2O_3 Fibers

Fiber Morphology

The Y-TZP/Al_2O_3 fibers derived from the colloidal ZrO_2 sols and inorganic salts developed unique microstructures, depending on their thermal history. Microstructural changes in the Y-TZP/Al_2O_3 fibers containing 2 mol% Y_2O_3 and various amounts of Al_2O_3 at different sintering temperatures are illustrated in Figures 5.22 through 5.25.

The Y-TZP and Y-TZP/Al_2O_3 fibers sintered at 1200°C exhibit very smooth surfaces with micropores. The Al_2O_3 particles do not appear in the surfaces of the Y-TZP/Al_2O_3 fibers containing 10 wt% Al_2O_3 as shown in Figure 5.22 (a). When the fibers with the same compositions (Figure 5.22) were sintered above 1400°C, interesting microstructures were obtained. The Al_2O_3 particles become visible as dark areas in Figure 5.23 (a). They appear to be elongated and nonuniformly distributed in the ZrO_2 matrix. The Al_2O_3 particles can be seen more clearly at 1500°C. In Figure 5.24 (a), the surfaces of the Y-TZP/Al_2O_3 fibers containing 16.7 wt% Al_2O_3 show that the elongated Al_2O_3 particles form regions with a localized grain alignment which are randomly distributed. The Y-TZP fibers sintered at 1500°C exhibit the same

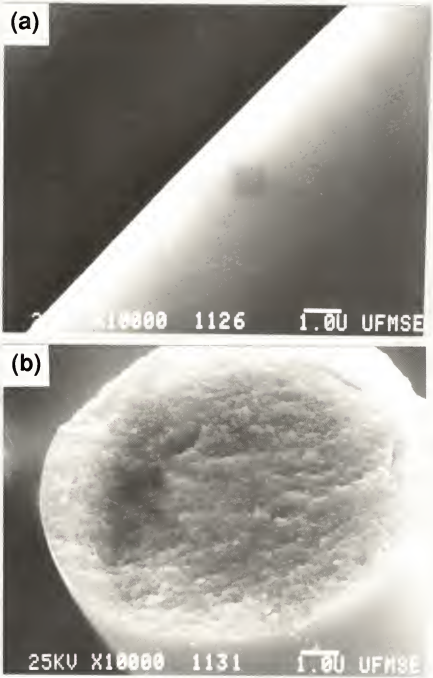

Figure 5.22. Scanning electron micrographs of Y-TZP/Al_2O_3 fibers containing 2 mol% Y_2O_3 and 10 wt% Al_2O_3 fired at 1200°C showing (a) surface and (b) fracture surface.

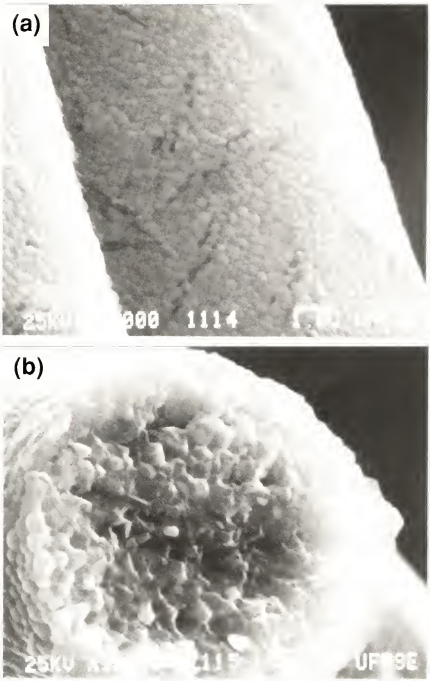

Figure 5.23. Scanning electron micrographs of Y-TZP/Al_2O_3 fibers containing 2 mol% Y_2O_3 and 10 wt% Al_2O_3 fired at 1400°C showing (a) surface and (b) fracture surface.

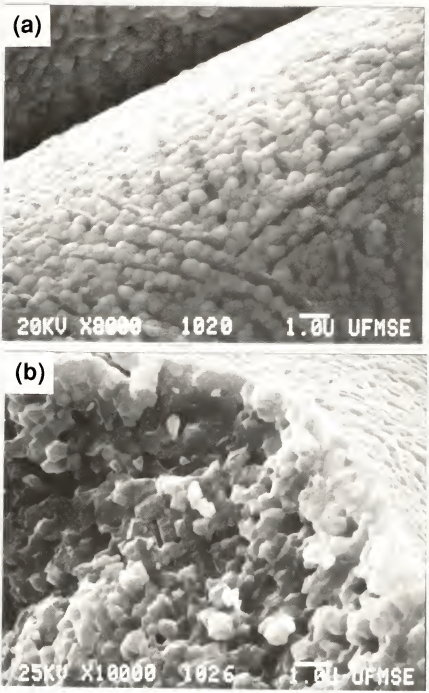

Figure 5.24. Scanning electron micrographs of Y-TZP/Al_2O_3 fibers containing 2 mol% Y_2O_3 and 16.7 wt% Al_2O_3 fired at 1500°C showing (a) surface and (b) fracture surface.

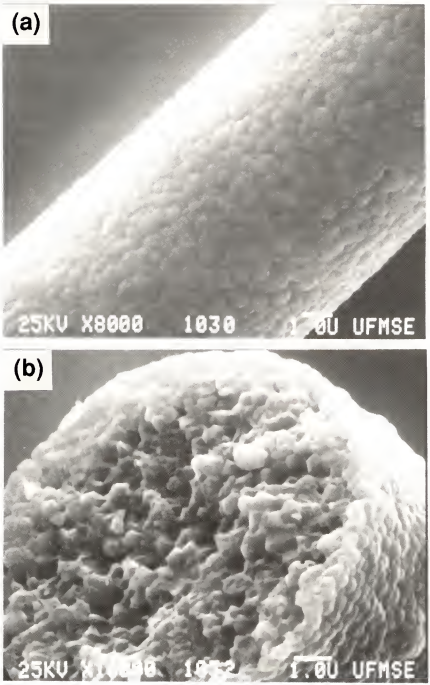

Figure 5.25. Scanning electron micrographs of Y-TZP fibers containing 2 mol% Y_2O_3 fired at 1500°C showing (a) surface and (b) fracture surface.

morphology as in the Y-TZP/Al_2O_3 fibers with the exception of the Al_2O_3 particles, as shown in Figure 5.25 (a). Such elongated Al_2O_3 particles have never been reported in Y-TZP/Al_2O_3 composites.

The fracture surfaces of the Y-TZP/Al_2O_3 fibers in Figure 5.22 (b) revealed flaws resulting from bubbles present in the sol. The fibers sintered up to 1400°C were fractured mostly intergranuarly as shown in Figures 5.22 (b) and 5.23 (b). The elongated Al_2O_3 particles were present and randomly distributed inside the Y-TZP/Al_2O_3 fibers, as indicated by the pullout of the particles in the fracture surface in Figure 5.24 (b). The Y-TZP and Y-TZP/Al_2O_3 fibers sintered at 1500°C exhibited intergranular and transgranular fracture.

It was speculated that the alignment and elongation of the Al_2O_3 particles could have occurred during fiber spinning. However, the polished surface of a Y-TZP/Al_2O_3 bulk sample using powder prepared from the sol containing 2 mol% Y_2O_3 and 16.7 wt% Al_2O_3 and sintered at 1500°C in Figure 5.26 (a) exhibits the same morphology as seen in the fibers with the same composition. This indicates that the alignment and elongation are associated with the precursors used in this study and are not due to fiber forming. The Al_2O_3 particles and the matrix are seen as dark areas (A) and light areas (B), respectively. The energy dispersive X-ray spectrum in Figure 5.26 (b) show that the dark area corresponds to Al_2O_3, indicated by stronger intensity of the aluminum in spectrum A than in spectrum B. The peak corresponding to zirconium in spectrum A arises from the surrounding matrix. The peaks corresponding to palladium in both spectra result from the sample coating.

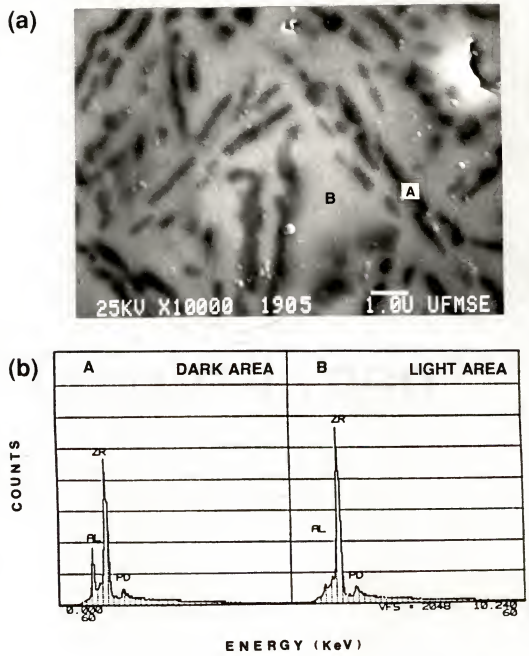

Figure 5.26. Polished surface (a) and EDS spectra (b) of bulk Y-TZP/Al_2O_3 sample containing 2 mol% Y_2O_3 and 16.7 wt% Al_2O_3 fired at 1500°C for 2 hours.

Coarsening of Alumina Particles in the Y-TZP matrix

The Y-TZP and Y-TZP/Al_2O_3 fibers containing 2 mol% Y_2O_3 exhibited a small amount of monoclinic ZrO_2 after sintering at temperatures above 1400°C, which is usually detrimental to the mechanical properties of the fibers. The transformation of the tetragonal to the monoclinic phase accompanies a volume expansion and results in microcracks in the fibers. This was observed in the Y-TZP and Y-TZP/Al_2O_3 fibers containing 2 mol% Y_2O_3. Therefore, the microstructure was characterized with the Y-TZP and Y-TZP/Al_2O_3 fibers containing 3 mol% Y_2O_3.

The polished surfaces of the Y-TZP/Al_2O_3 fibers containing 3 mol% Y_2O_3 and 15 wt% Al_2O_3, shown in Figure 5.27, illustrate the morphological changes of the Al_2O_3 particles in the Y-TZP matrix with respect to sintering temperature. The Al_2O_3 particles, although present in the X-ray diffraction spectrum, could not be seen in the fibers sintered at 1200°C. The smooth and featureless polished surface of the fibers is seen in Figure 5.27 (a). At 1300°C, the Al_2O_3 particles were distinguishable from the ZrO_2 grains and randomly distributed. Concurrently, some Al_2O_3 particles were locally aligned and exhibited an incipient anisotropic growth. The Al_2O_3 particles appeared to coarsen at the expense of the neighboring small particles, indicated by the Al_2O_3-free zones surrounding the particles in the same direction (Figure 5.27 (b)). In Figure 5.27 (b), the small Al_2O_3 particles are seen as dark speckles.

Coarsening of the Al_2O_3 particles was more evident at higher sintering temperatures. The polished surface of the fiber sintered at 1400°C (Figure 5.27 (c))

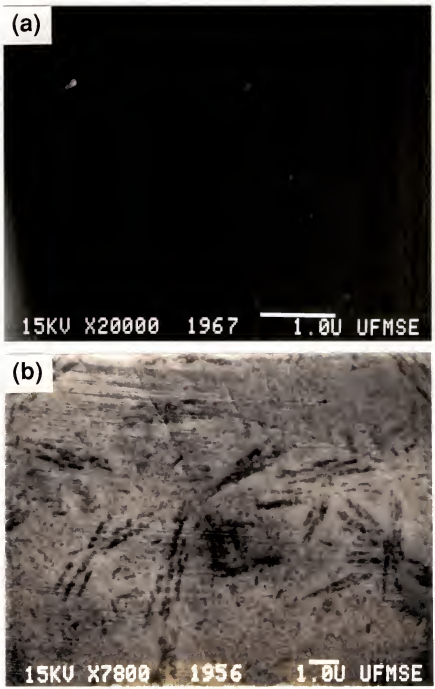

Figure 5.27. Polished surfaces of Y-TZP/Al_2O_3 (3 mol% Y_2O_3 and 15 wt% Al_2O_3) fibers sintered at (a) 1200°C, (b) 1300°C, (c) 1400°C, and (d) 1500°C. Dark areas are alumina particles.

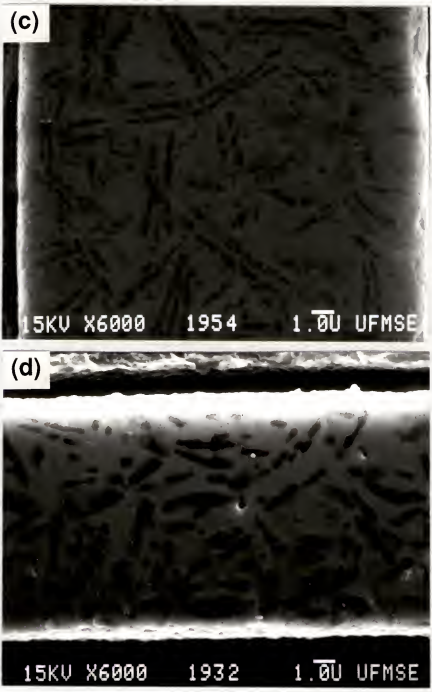

Figure 5.27 -- Continued.

shows that the Al_2O_3 particles grow at the expense of small particles and are elongated while the number of the particles decreases. The small Al_2O_3 particles which had been randomly distributed at 1300°C were not present at 1400°C. These apparently coalesced into larger Al_2O_3 particles. At 1500°C, a coarsening process involving growth and elongation of the Al_2O_3 particles was continued. Figure 5.27 (d) shows that the particles become larger and more elongated with fewer number of the particles, as compared with the fibers sintered at 1400°C. The chemically etched surface of the fiber sintered at 1500°C revealed that, when the elongated particles are in contact with each other, they readily coalesce to form a single particle with a larger aspect ratio (length/diameter). Figure 5.28 shows the agglomerated particles consisting of several elongated particles having nearly the same diameter.

Transmission electron micrographs of Figures 5.29 through 5.31 show the Al_2O_3 particles and grain boundary areas in the Y-TZP/Al_2O_3 fibers after sintering at 1200°, 1400° and 1500°C, respectively. At 1200°C, as shown in Figure 5.29 (a), the Al_2O_3 particles with sizes varying up to $\approx$0.2 μm are embedded between the ZrO_2 grains. The electron-transparent Al_2O_3 particles are seen as light areas. The ZrO_2 grains are faceted and the average gain size agrees with that measured from the fiber surfaces using the line intercept method (Figure 5.29 (b)). The grain boundaries between ZrO_2 and Al_2O_3 appear to be clean (Figure 5.29 (c)). No pockets are seen at triple joints. Energy-dispersive X-ray analysis of this grain boundary region indicates the presence of silicon and calcium in addition to aluminum, yttrium and zirconium from surrounding grains (Figure 5.29 (d)).

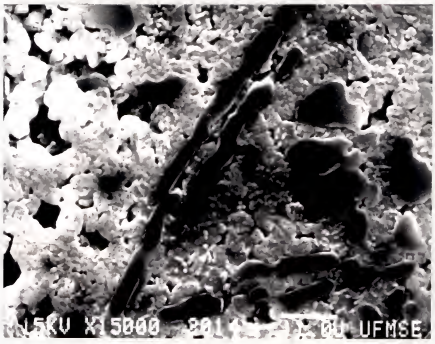

Figure 5.28. Polished surface of Y-TZP/Al_2O_3 (3 mol% Y_2O_3 and 15 wt% Al_2O_3) fibers sintered at 1500°C, showing coalescence of elongated alumina particles. The sample was etched with a dilute HF solution to reveal alumina.

Figure 5.29. Transmission electron micrographs of Y-TZP/Al_2O_3 (3 mol% Y_2O_3 and 15 wt% Al_2O_3) fibers at 1200°C, showing (a) alumina particles embedded in the zirconia matrix, (b) faceted zirconia grains (dark areas are zirconia grains and light areas are alumina particles), (c) a triple joint of zirconia and alumina having clean interfaces, and (d) EDS spectrum at the triple joint in (c).

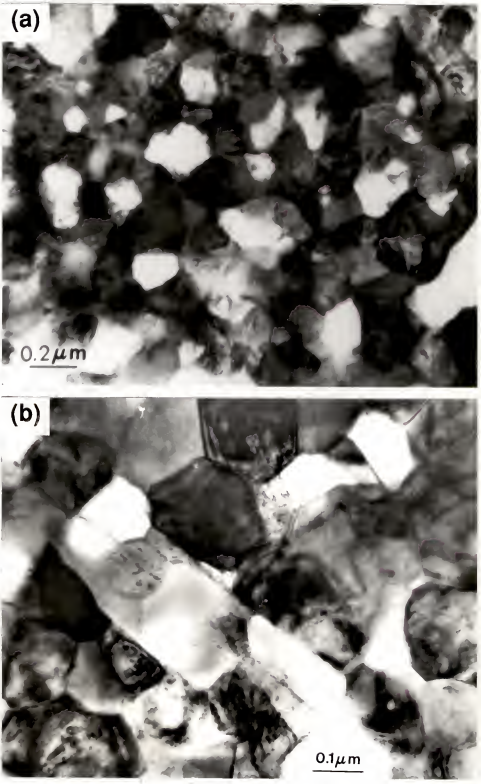
(a)
0.2μm
(b)
0.1μm

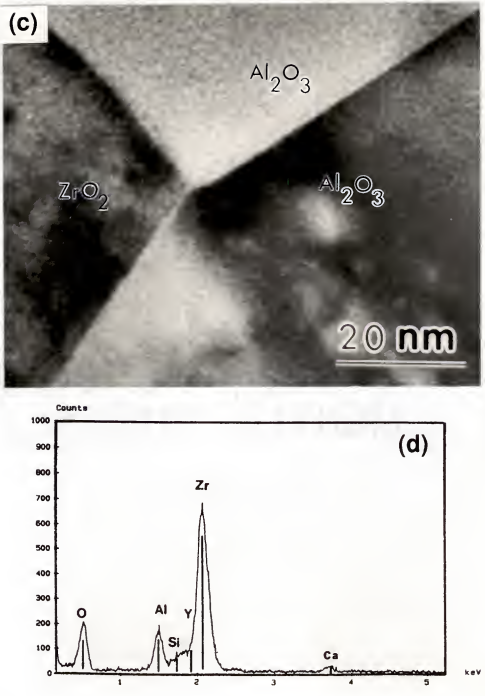

Figure 5.29 -- Continued.

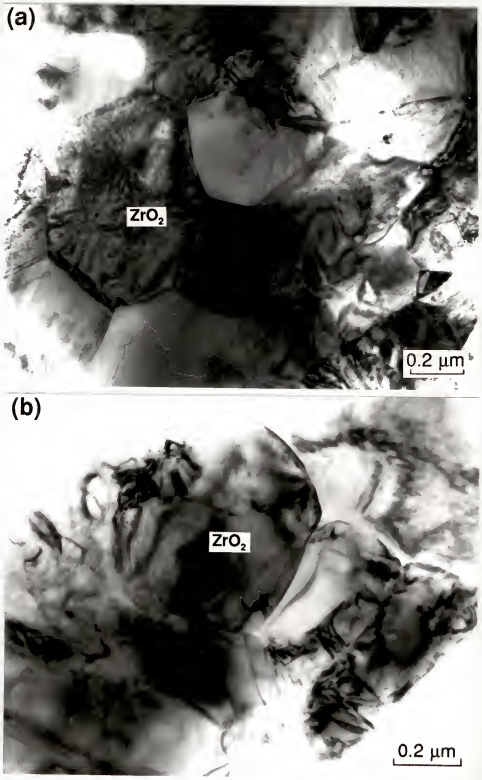

Figure 5.30. Transmission electron micrographs of Y-TZP/Al_2O_3 (3 mol% Y_2O_3 and 15 wt% Al_2O_3) fibers at 1400°C, showing (a) faceted zirconia grains (b) pockets formed between zirconia grains.

Figure 5.31. Transmission electron micrographs of Y-TZP/Al_2O_3 (3 mol% Y_2O_3 and 15 wt% Al_2O_3) fibers at 1500°C: (a) elongated alumina particles with ar aspect ratio >3 (A, B, C, D, and E grains)(insets are microdiffraction patterns of tetragonal zirconia and α-Al_2O_3), (b) a pocket formed between zirconia grains, (c) a triple joint of zirconia and alumina showing thin, continuous intergranular amorphous phases formed after sintering for 2 hours), and (d) EDS spectrum of the pocket in (b) including matrix grains.

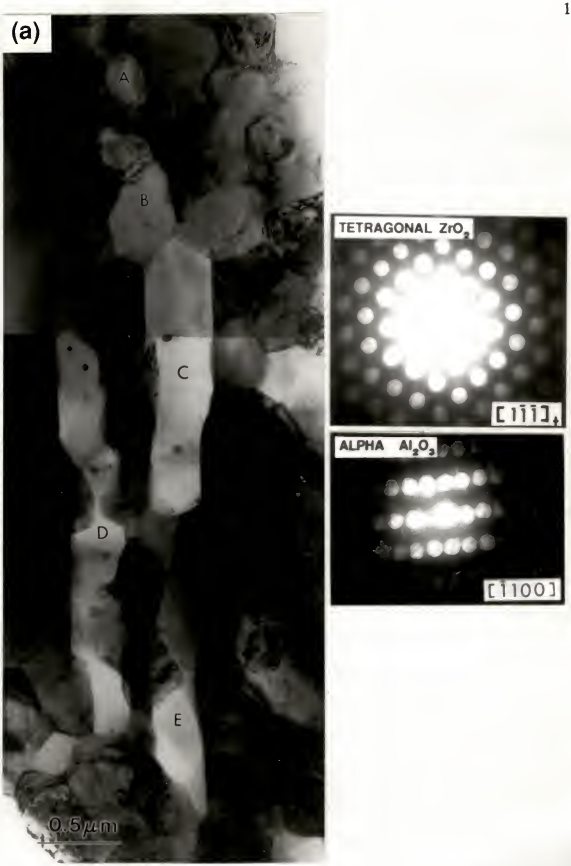
(a)
A
B
C
D
E
0.5μm
TETRAGONAL ZrO_2
$[\bar{1}\bar{1}\bar{1}]_t$
ALPHA Al_2O_3
$[\bar{1}100]$

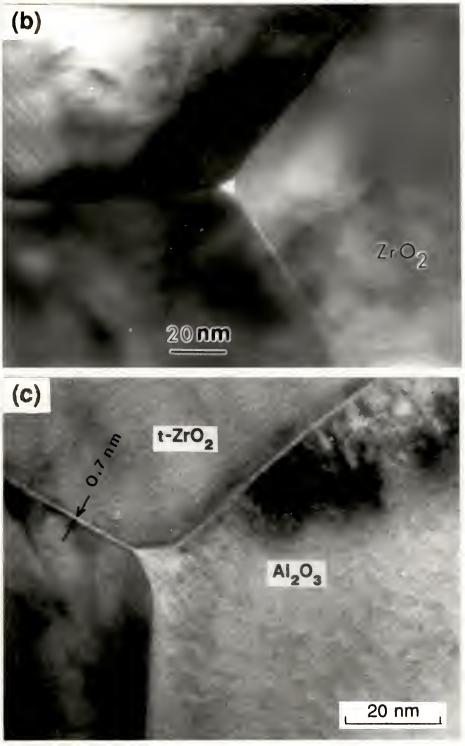

Figure 5.31 -- Continued.

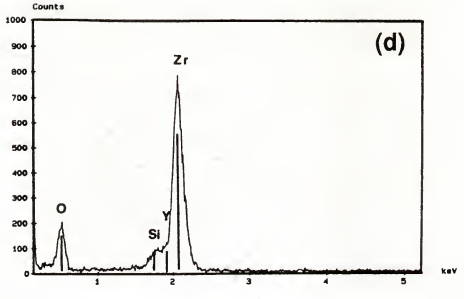

Figure 5.31 -- Continued.

At 1400°C, most ZrO_2 grains are faceted (Figure 5.30 (a)). However, occasionally, some grains with round corners and pockets at these grain corners appear. The round grains are indicative of the presence of a liquid phase.

As shown in Figure 5.31 (a), at 1500°C, anisotropic shapes of the Al_2O_3 particles are clearly visible. Electron microdiffraction patterns confirm that the fibers consist of tetragonal ZrO_2 and α-Al_2O_3. The elongated Al_2O_3 particles are $\approx$0.3 μm wide with an aspect ratio >3. The Al_2O_3 grains in C and D in Figure 5.31 (a) have a larger aspect ratio and the same orientation. The ZrO_2 grain boundary junction exhibits a pocket, possibly containing SiO_2, Y_2O_3 and ZrO_2 (Figure 5.31 (b) and (d)). However, due to the limited spatial resolution of the X-ray analyzer employed, the chemical composition of the pocket could not be quantitatively measured. The EDS spectra from pockets in the samples sintered at 1500°C and triple joints in the samples sintered at 1200°C (Figure 5.29 (d) and 5.31 (d)) show the similar intensities of silicon, yttrium and zirconium. The yttrium and zirconium in the EDS spectra also arise from the matrix grain. After sintering for 2 hours at 1500°C, the grain boundaries between the ZrO_2 grains and the Al_2O_3 inclusions exhibit pockets at triple joints and thin, continuous intergranular phases (Figure 5.31 (c)). The grain boundary phase could not be identified by EDS analysis and diffraction study since the grain boundary phase was less than 1 nm thick.

The TEM results did not provide a clear indication of a liquid formation temperature. Although the detection of the intergranular liquid phase was difficult due to the spacial resolution of the TEM, it can be seen from the impurities present in the

fibers that the liquid phase can form at a temperature as low as 1200°C. Chemical analysis of the Y-TZP/Al_2O_3 fibers in Table 5.4 shows that SiO_2 and CaO are major impurities. These impurities are due to the ZrO_2 sol. Because of low solubility of SiO_2 in the ZrO_2 lattice, SiO_2 will be either segregated to grain boundaries or, at some critical concentration, exist as a liquid phase when the sintering temperature is raised or sintering time is increased. Some Y_2O_3 also will be present in this liquid phase due to a eutectic with 45 wt% SiO_2, 20 wt% Al_2O_3 and 35 wt% Y_2O_3 which is liquid at 1250°C, according to the SiO_2-Al_2O_3-Y_2O_3 phase diagram [Levi64]. The temperature of a liquid formation can be lowered by the presence of impurities such as CaO. The formation of liquid at temperature lower than 1400°C has been observed in the quaternary system ZrO_2-Al_2O_3-SiO_2-CaO [Pen85].

Second-phase particles in ceramic compacts can coarsen by two distinct processes: Ostwald ripening or coalescence. During Ostwald ripening, small particles disappear while large ones grow because of the difference in solubility for particles of different sizes. Smaller particles have a higher solubility than larger particles. This causes matter to be transported from the smaller to the larger particles. Alternatively, particles can grow by coalescence, if they are dragged by migrating matrix grain boundaries. In the coalescence process, disappearance of small matrix grains cause particles to meet, coalesce, and thus form larger particles. For the coarsening of particles in a liquid phase, two mechanisms have been proposed [Mas80]. One is the solution-precipitation mechanism and the other is the coalescence mechanism. The solution-precipitation mechanism can be explained by Ostwald ripening. In an actual

TABLE 5.4

Chemical Analysis of Y-TZP/Al_2O_3 Fibers* Containing 3 mol% Y_2O_3 and 15 wt% Al_2O_3

Element	Amount (wt%)
Zr	49.31
Y	4.00
Al	9.40
Si	0.099
Ca	0.041
Na	0.07
Mg	<0.019

* Fibers were fired at 1200°C for 4 hours. The chemical analysis was performed with inductively coupled plasma atomic emission spectrophotometer (ICP) at Galbraith Laboratories, Inc., Knoxville, TN.

sintering process, the Ostwald ripening and coalescence mechanisms operate concurrently.

Results from TEM observations suggest that the liquid phase plays a role in the coarsening process of the Al_2O_3 particles. During sintering of the fibers, the Al_2O_3 particles coarsens in the Y-TZP matrix by Ostwald ripening (solution-precipitation due to the intergranular liquid phase), as shown by the Al_2O_3-free zones surrounding the Al_2O_3 particles. However, the coalescence mechanism also is operative since the matrix grain boundaries migrate (growth of ZrO_2 grains). Lange and Hirlinger [Lan87] have observed that the coalescence of Al_2O_3 inclusions occurs at ZrO_2 grain junctions when the inclusions become mobile at high sintering temperatures (>1600°C) and move with matrix grain boundaries.

In the present study, local alignment of the Al_2O_3 particles is not fully understood. However, elongation of the Al_2O_3 particles can be attributed to the liquid phase and provides an indirect indication of the presence of a small amount of the liquid phase and incomplete wetting of grains by the liquid. Recent experiments by Shaw [Sha87] show that a trace amount of a liquid phase in Al_2O_3 can be nonuniformly distributed on the grain scale, even when large volumes of liquid are present and a substantial fraction of the boundaries are not wet by the liquid. In such a case, elongation of the Al_2O_3 particles in the Y-TZP matrix is believed to be due to the higher mobility of clean Al_2O_3 grain boundaries than those wet by intergranular liquids [Bat89]. Kaysser et al. [Kay87] have reported the exaggerated growth of Al_2O_3 single-crystal seeds in an Al_2O_3 matrix containing a liquid phase of anorthite

($CaO{\cdot}Al_2O_3{\cdot}SiO_2$)(≈1.8 vol%). The basal planes {0001} wet by the liquid were faceted and exhibited a slow growth rate. Similarly, faceted Al_2O_3 grains with large aspect ratios have been observed by Bateman et al. [Bat89] in an Al_2O_3 containing a small amount (≈0.25 vol%) of a silicate-based liquid phase.

The elongated Al_2O_3 particles resemble the whiskers in whisker-reinforced composites, except in this case they are grown in situ during sintering. At present, it is not known if the elongated, whisker-like second particles strengthen the fibers. However, such a microstructure should be beneficial in increasing toughness of bulk Y-TZP/Al_2O_3 composites. If composites are prepared from the sols used in this study, they can be fully densified before the second phase hinders the densification followed by in situ formation of the elongated particles.

Effect of Alumina on Densification

Densities of the Y-TZP and Y-TZP/Al_2O_3 fibers with respect to sintering temperatures are presented in Figure 5.32. The addition of 15 wt% (21.3 vol%) Al_2O_3 resulted in higher densities than those of the Y-TZP fibers containing only 3 mol% Y_2O_3. The maximum relative density of the Y-TZP fibers was 95%, while the maximum relative density of the Y-TZP/Al_2O_3 fibers was 99.5% at 1400°C. Densities of the Y-TZP/Al_2O_3 fibers sintered below 1400°C could not be measured by the point-counting method, because no pores were seen on the scanning electron micrographs of the polished fibers, as shown in Figure 5.27 (a) and (b). Attempts to detect pores with a high resolution scanning electron microscope were not successful. It is possible that

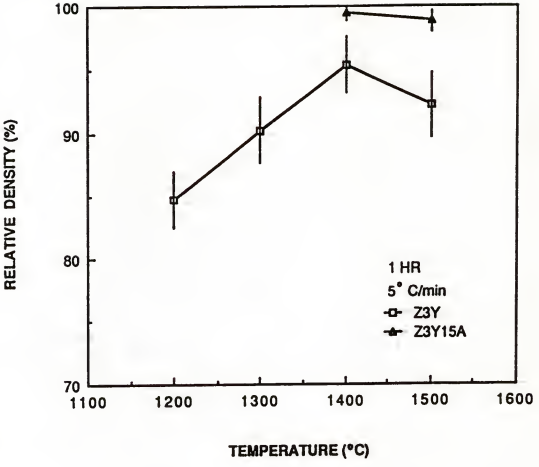

Figure 5.32. Plot of relative density versus sintering temperature for Y-TZP and Y-TZP/Al_2O_3 fibers at a heating rate of 5°C/min and held for 1 hour.

pore sizes are too small to be detected by SEM. However, TEM observations did not reveal pores, suggesting that the fibers had been fully densified at these temperatures (Figure 5.29). The decrease in relative densities of the Y-TZP and Y-TZP/Al_2O_3 fibers sintered at 1500°C is not understood but could be due to the experimental accuracy, as indicated by the error bars in Figure 5.32.

In contrast to those of the Y-TZP/Al_2O_3 fibers, the polished surfaces of the Y-TZP fibers sintered at 1200°C having a relative density of 85% showed interconnected pores and a skeletal structure of solid particles which are typical microstructures of sol-gel-derived materials (Figure 5.33 (a)). As a result of pore coarsening, these pores became larger and isolated at 1400°C, as shown in the polished surfaces of the Y-TZP fibers sintered at 1400°C (Figure 5.33 (b)).

Despite a large amount of Al_2O_3 which normally retards densification, the increased density in the Y-TZP/Al_2O_3 fibers is due primarily to the presence of an intergranular liquid phase at sintering temperatures. It has been suggested that Y-TZP ceramics are densified by liquid phase sintering, owing to the continuous intergranular liquid phases which are formed by SiO_2 and other trace amounts of impurities [Rüh84, Sch84, Mec87]. A small addition of Al_2O_3 as a sintering aid to Y_2O_3-stabilized ZrO_2 (YSZ) has been found to promote densification by a liquid phase sintering mechanism [Rad79, Buc84]. A liquid phase contributes to particle rearrangement through grain boundary sliding, assisting in the dissolution of particle-particle contacts and providing a high diffusivity path for rapid mass transport during sintering. Large capillary

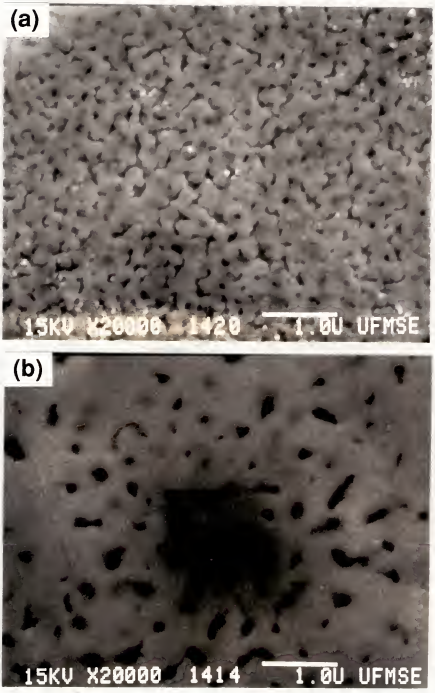

Figure 5.33. Polished surfaces of Y-TZP (3 mol% Y_2O_3) fibers sintered at (a) 1200°C and (b) 1400°C.

pressure resulting from small liquid contents (≤1.0 vol%) and very fine particles leads to a significant enhancement in the densification behavior [Kin59, Kin76].

The results from density measurements and SEM and TEM observations suggest that, at sintering temperatures below 1400°C, insufficient liquid is present to cause significant rearrangement at least in the Y-TZP sample. As a result of the incomplete wetting, grain growth sufficient to form a solid skeleton occurs and thus the densification process is slowed and stopped. The role of the Al_2O_3 inclusions appears to be an enhancement in the amount and reactivity of the liquid phase at equivalent temperatures which causes an increase in the densification rate. Such a liquid phase provides a continuous, high diffusivity path along the boundaries. The higher densities of the Y-TZP/Al_2O_3 samples than those of the Y-TZP samples indicate the presence of a more reactive and perhaps lower viscosity intergranular phase with the incorporation of Al_2O_3 [Buc84]. At higher sintering temperatures, with a higher expected liquid phase content, liquid phase sintering mechanisms became significant and led to complete densification of the Al_2O_3-containing samples.

Another role of the Al_2O_3 inclusions contributing to densification is grain boundary pinning by the inclusions, as proposed by Butler and Drennan [But82]. Since there is a limited solubility of Al_2O_3 in a liquid phase (e.g., ≈0.1 mol% in YSZ at 1300°C), most Al_2O_3 exists as discrete particles at the intersections of ZrO_2 grains and may reduce grain boundary mobility. They prevent grain growth by grain boundary pinning for long enough so that most of the porosity is eliminated before the breakaway of a boundary takes place. For the Y-TZP/Al_2O_3 fibers, this is anticipated

only in the early stage of sintering or at low sintering temperatures where the inclusions are very fine and distributed uniformly around the ZrO_2 grains. However, at high sintering temperatures, the effect of the inclusions is insignificant because of the extensive coarsening (coalescence) of the Al_2O_3 particles. In fact, larger grain sizes of the ZrO_2 in the Y-TZP/Al_2O_3 than those in the Y-TZP fibers were observed after sintering for 1 hour at temperatures above 1400°C, as discussed later.

Grain Growth of Zirconia on Y-TZP/Al_2O_3 Fiber Surfaces

Grain growth on a fiber surface can be affected by the fiber geometry. Grain boundary movement is restrained by grain boundary curvature and boundary grooves. Grain boundaries near any free surface tend to lie perpendicular to the specimen surface and grain boundary curvature becomes cylindrical rather than spherical. In general, cylindrical surfaces move at slower rates than spherical surfaces with the same radius of curvature because of a lower driving force for the boundary movement in the cylindrical surface than in the spherical surface (the pressure difference across a cylindrical surface is $2\gamma/R$ and across a spherical surface $4\gamma/R$, where γ is the surface tension and P the radius of the curvature) [Ree73].

When grain boundaries meet a free surface, boundary grooves form on the surfaces where grain boundaries intersect the free surface (thermal grooving). The formation of the grooves is due to the transport of atoms out of the grooved regions. The thermal grooving on a free surface has an effect of greater importance on grain growth than does the reduction of the curvature of boundaries at a surface does. Grain

boundary grooves tend to anchor the ends of the grain boundaries at free surfaces, especially if the boundaries are nearly normal to the surface. To free the boundary from its groove requires work and, as a result, the groove restrains the movement of the boundary [Mul58].

However, in the Y-TZP and Y-TZP/Al_2O_3 fibers, thermal grooving or the lack of curvature in the surface grains is expected to have little effect on the overall rate of grain growth because the average grain sizes of ZrO_2 (0.1-0.5 μm) are relatively small as compared to the dimensions of the fibers (5-15 μm). Although the free-surface effect of ceramic fibers has not been studied to date, in general, the grain growth rate decreases when the grain size of bulk materials becomes larger than one-tenth the thickness of the sample [Bec54].

The kinetics of grain growth have been described by the traditional phenomenological rate equation [Hil65, Bro76]

$$G^n - G_o^n = K_o t e^{-Q/RT}, \tag{5.5}$$

where G is the average grain size after time t, G_o is the initial average grain size, n is the grain growth kinetic exponent, K_o is a rate constant, Q is the activation energy for the grain growth process, R is the gas constant, and T is the absolute temperature. The most significant descriptive parameters are the grain growth kinetic exponent which is usually related to the rate-controlling mechanism of grain boundary migration, and the activation energy which can often be related to the specific mass-transport mechanism during the isothermal heat treatment. These two parameters may

indicate processes of surface or volume diffusion, evaporation and condensation, solution and precipitation, coalescence, and many others. However, as a consequence of concurrently operative mechanisms, it is not always possible to unambiguously identify the specific mass-transport process, as often the magnitude of the activation energy does not compare directly to that of any elementary mass-transport process [Hil65, Bro76].

Equation (5.5) illustrates that different rate-controlling mechanisms may be expected to yield different kinetic exponents for the relationship of the grain size to sintering time, and perhaps different activation energies as well. Since the initial zirconia particle size (0.005-0.01 μm) is much smaller than the final grain sizes (0.1-0.5 μm) and grain size measurement errors (≈0.01-0.03 μm) are larger than the initial particle size (Table 5.5), the grain growth can be estimated by neglecting the G_o^n term from the equation (5.5) and rewriting that equation as

$$G^n = K_o t e^{-Q/RT}. \tag{5.6}$$

Plotting log G against log t for a constant temperature will yield a straight line with the slope equal to the value of 1/n, if the grain growth mechanism does not change with increasing grain size (G) or sintering time (t). If the kinetic exponent is established to be constant, then the equation (5.6) can be rewritten in the form

$$\log (G^n/t) = \log (K_o) - (Q/2.303R)(1/T). \tag{5.7}$$

TABLE 5.5

Average Zirconia Grain Size in Y-TZP and Y-TZP/Al_2O_3 Fibers*

Temperature(°C)	Z3Y	Z3Y15A+
1200	0.14 (0.01)&	0.08 (0.01)
1300	0.16 (0.01)	0.14 (0.02)
1400	0.23 (0.01)	0.34 (0.02)
1500	0.36 (0.02)	0.52 (0.03)

*Fibers were sintered for 1 hour at a heating rate of 20°C/min.

+3Y and 15A correspond to 3 mol% Y_2O_3 and 15 wt% Al_2O_3, respectively.

&Grain size is in μm and the number in parenthesis is the 95% confidence limit.

A plot of log (G^n/t) versus 1/T gives a slope of -Q/2.303R from which the activation energy can be determined.

Figures 5.34 and 5.35 illustrate a series of the microstructures of the Y-TZP and Y-TZP/Al_2O_3 fibers after sintering up to 1500°C for 1 hour. The surfaces of the Y-TZP fibers containing 3 mol% Y_2O_3 at 1200° and 1300°C (Figure 5.34 (a) and (b)) consisting of small ZrO_2 grains with average grain sizes of 0.14 and 0.16 μm, respectively, show pores at intergranular sites, with the exception that fewer pores are seen at 1300°C. At 1500°C, the surface shows significant growth of the grains and profound grain boundary grooving. No pores are seen on the surface. In contrast to the surfaces of the Y-TZP fibers, the surfaces of the Y-TZP/Al_2O_3 containing 3 mol% Y_2O_3 and 15 wt% Al_2O_3 at 1200° and 1300°C consist of smaller ZrO_2 grains than those in the Y-TZP fibers and do not show any pores or grain boundaries clearly. The Al_2O_3 particles can be seen barely at 1300°C at intersections of ZrO_2 grains. However, as seen previously in the polished surfaces, at 1500°C, the Al_2O_3 particles coarsen rapidly and become large in length and diameter. The surfaces of the Y-TZP/Al_2O_3 fibers rarely reveal pores.

Figure 5.36 represents the ZrO_2 grain size on surfaces of the Y-TZP and Y-TZP/Al_2O_3 fibers as determined from the samples in Figures 5.34 and 5.35. The ZrO_2 grains in the Y-TZP fibers grow steadily as the sintering temperature increases to above 1400°C. However, they become larger in the Y-TZP/Al_2O_3 fibers than in the Y-TZP fibers. Above 1400°C, the ZrO_2 grains grow simultaneously with rapidly

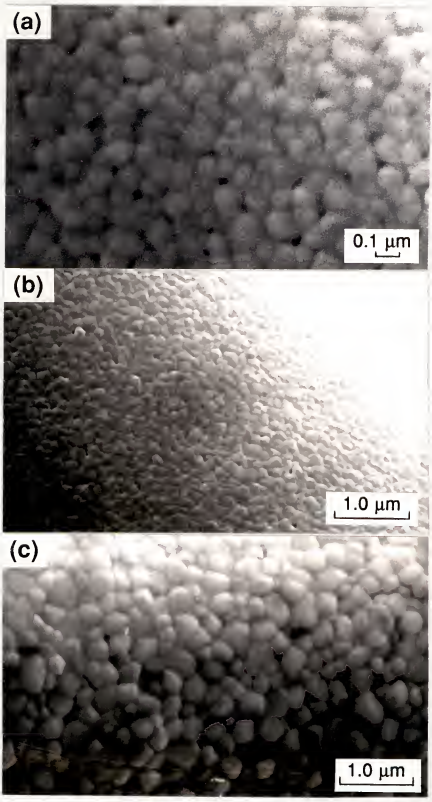

Figure 5.34. Scanning electron micrographs of Y-TZP (3 mol% Y_2O_3) fibers sintered at (a) 1200°C, (b) 1300°C and (c) 1500°C.

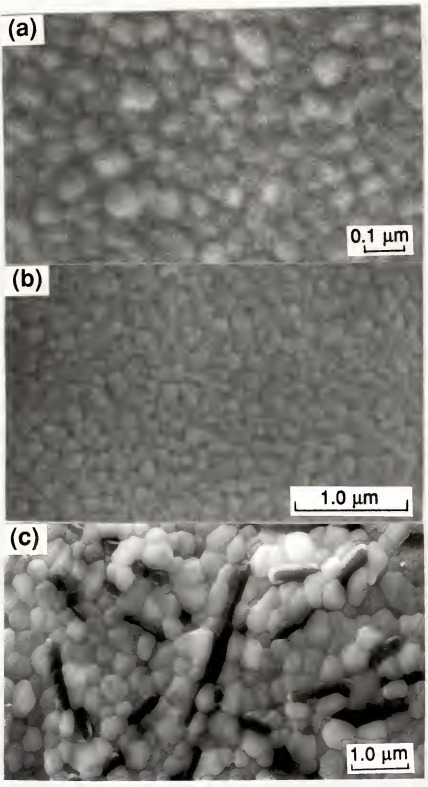

Figure 5.35. Scanning electron micrographs of Y-TZP/Al_2O_3 (3 mol% Y_2O_3 and 15 wt% Al_2O_3) fibers sintered at (a) 1200°C, (b) 1300°C and (c) 1500°C. Light grains are zirconia and dark grains are alumina.

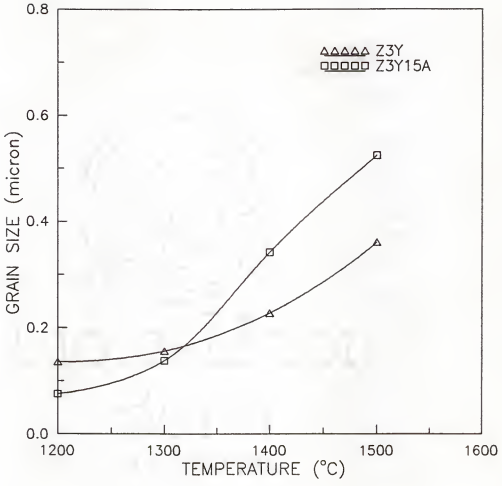

Figure 5.36. Plot of zirconia grain size versus temperature for the Y-TZP and Y-TZP/Al_2O_3 fibers sintered for 1 hour.

growing and elongating Al_2O_3 particles. This result suggests that the grain growth of ZrO_2 is relatively slow and the Al_2O_3 inclusions enhance the growth of ZrO_2 grains.

The increased grain size of ZrO_2 in the Y-TZP/Al_2O_3 fibers above 1400°C is believed to be due to the presence of a reactive liquid phase during the densification process. Similar results have been reported in YSZ containing a small amount of Al_2O_3 (0.325 wt%) by Buchanan and Wilson [Buc84]. In practice, it is found that adding a moderate amount of silicate liquid phase to Al_2O_3 prevents the extensive grain growth which frequently occurs with pure materials [Bir85]. A SiO_2 phase has been incorporated in many commercial Al_2O_3-based oxide fibers, not only to enhance the densification, but also to inhibit the grain growth.

Effect of Alumina content on Grain Size of Zirconia

The effect of Al_2O_3 additions on the grain size of the ZrO_2 was studied from surfaces of the Y-TZP/Al_2O_3 fibers containing 3 mol% Y_2O_3 and 0 to 15 wt% Al_2O_3 and sintered at temperatures of 1400° and 1500°C, where the fibers become relatively dense and a normal grain growth is expected. At these temperatures, the grains grew sufficiently large and the boundary grooves became deepened. Thus, the grain size could be measured with a scanning electron microscope.

Figure 5.37 shows the effect of Al_2O_3 content on the grain size of ZrO_2 in the Y-TZP fibers sintered for 1 hour. The addition of 5 wt% Al_2O_3 (7.5 vol%) increased ZrO_2 grain sizes at both temperatures. A further addition of Al_2O_3 up to 15 wt% (21.3 vol%) retarded the ZrO_2 grain growth at 1400°C, while, at 1500°C, the grain growth

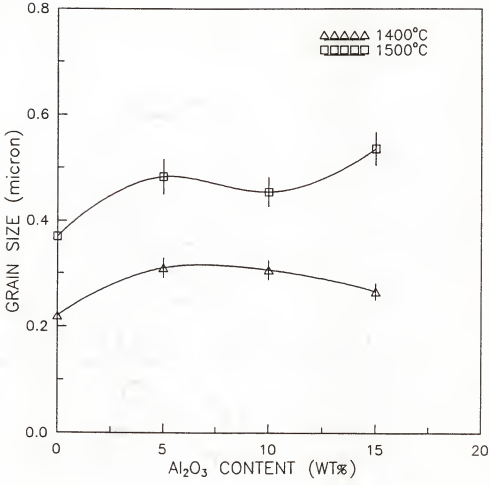

Figure 5.37. Plot of zirconia grain size versus alumina content in Y-TZP/Al_2O_3 fibers sintered at 1400° and 1500°C for 1 hour. Vol% of 5, 10, and 15 wt% Al_2O_3 correspond to 7.5, 14.5, and 21.3%, respectively.

did not follow the same trend as at 1400°C. Scanning electron micrographs of the Y-TZP/Al_2O_3 fibers in Figure 5.38 show the effect of Al_2O_3 content.

Ashby and Centamore [Ash68] have reported that second-phase inclusions, when they are finely dispersed and insoluble in the bulk material, have a drastic effect in suppressing grain growth (slowing boundary migration). The second-phase inclusions can either (1) move along with boundaries, offering little impedance; (2) move along with boundaries, with the inclusion mobility controlling the boundary velocity; or (3) be so immobile that the boundary pulls away from the inclusion. The effectiveness of the inclusions in inhibiting grain growth increases as their particle size is decreased and the volume fraction increases [Smi48]. However, in the case of the Y-TZP/Al_2O_3 fibers, the second-phase Al_2O_3 particles become mobile, tend to coalesce at high temperatures and form fewer large particles, as seen previously in the coarsening process of the Al_2O_3 particles up to 1500°C. Such coarsening diminishes the retarding effect of the inclusions on grain growth. This has been observed by Lange and Hirlinger [Lan87], who found in ZrO_2/Al_2O_3 composites that, if the size of alumina inclusions is much larger than ZrO_2, the inclusions have no effect on grain growth until the ZrO_2 grain size becomes ≈1.5 times the average inclusion size. At low temperature, the inclusions were relatively immobile and inhibited grain growth of zirconia with increasing volume fraction of the inclusions. At higher temperatures (>1600°C), grain growth was less inhibited when the inclusions could move with grain boundaries to coalesce. Their experiments showed only the grain sizes as a function

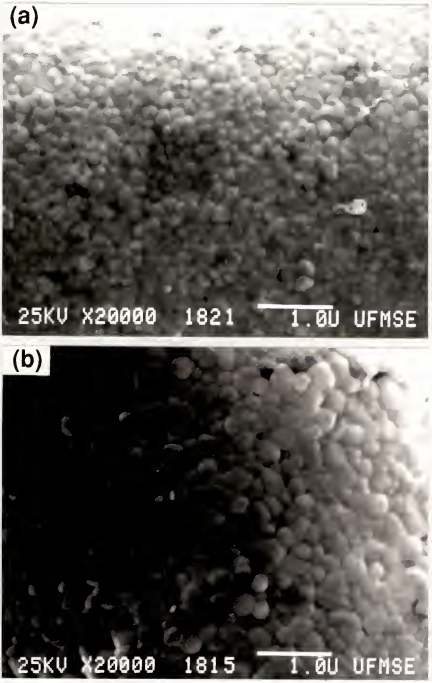

Fgiure 5.38. Scanning electron micrographs of Y-TZP/Al_2O_3 fibers sintered at 1400°C for 1 hour containing (a) 0, (b) 5, (c) 10, and (d) 15 wt% Al_2O_3.

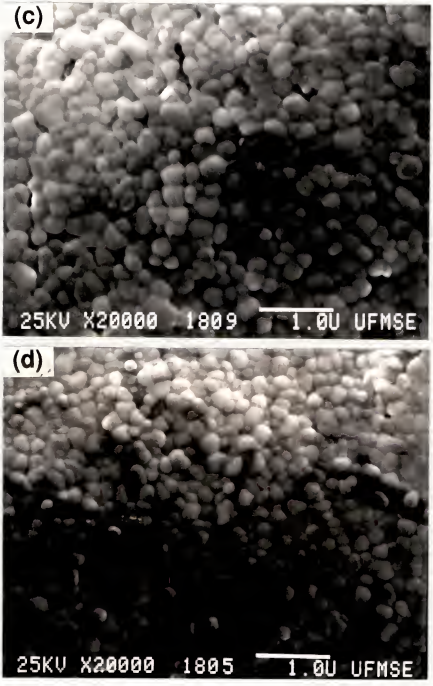

Figure 5.38 -- Continued.

of temperature, but did not show the time dependence of the grain sizes, which is necessary in order to determine the grain growth rate and mechanism.

Effect of Alumina Inclusions on Grain Growth of Zirconia

Figures 5.39 and 5.40 are plots of log G (grain size) versus log t (time), which illustrate the effects of time and temperature on the grain growth of the ZrO_2 on the surfaces of the Y-TZP and Y-TZP/Al_2O_3 fibers containing 3 mol% Y_2O_3, and 3 mol% Y_2O_3 and 15 wt% Al_2O_3, respectively. The firing time was limited at each temperature since the longer firing time, for example firing for 24 hours at 1400°C and for 6 hours at 1500°C, resulted in abnormal or exaggerated grain growth.

Figure 5.41 shows the surfaces of the Y-TZP/Al_2O_3 fibers containing 3 mol% Y_2O_3 and 15 wt% Al_2O_3 after firing for 0.1, 0.5, 1 and 2 hours at 1500°C, indicating that the grain growth occurs rapidly and becomes steady after 1 hour. It should be noted that the average grain sizes of the ZrO_2 are always larger in the Y-TZP/Al_2O_3 fibers than those in the Y-TZP fibers, but the difference between the average grain sizes of the two fibers is smaller at 1400°C than at 1500°C and decreases with increasing firing time.

In Figure 5.39, which illustrates the results for the Y-TZP fibers, the data appear to be consistent as the results lie on straight lines. A least-squares regression for the slopes of these two lines yields 0.22 and 0.23, corresponding to values for the grain growth kinetic exponents of 4.55 and 4.35 at 1400° and 1500°C, respectively. In general, previous theoretical considerations do not lead to fractional grain growth

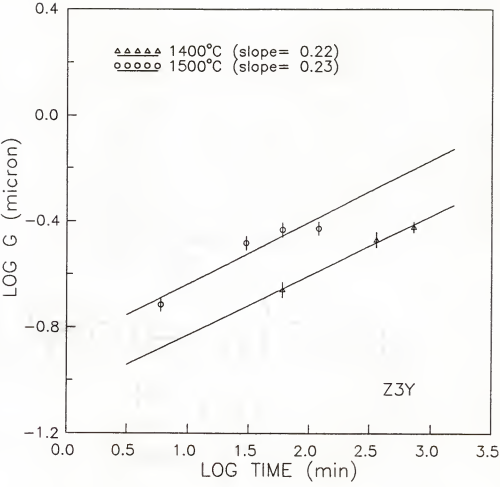

Figure 5.39. Plot of zirconia grain size versus sintering time for Y-TZP (3 mol% Y_2O_3) fibers sintered at 1400° and 1500°C.

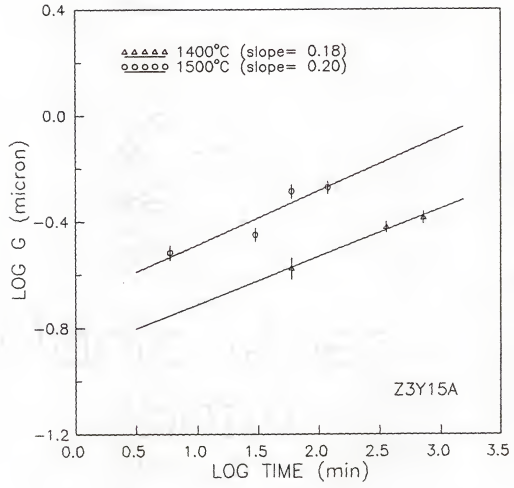

Figure 5.40. Plot of zirconia grain size versus sintering time for Y-TZP/Al_2O_3 (3 mol% Y_2O_3 and 15 wt% Al_2O_3) fibers sintered at 1400° and 1500°C.

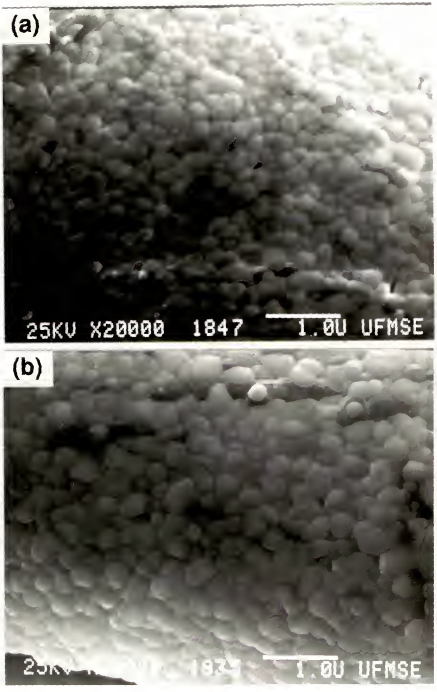

Figure 5.41. Scanning electron micrographs of Y-TZP/Al_2O_3 (3 mol% Y_2O_3 and 15 wt% Al_2O_3) fibers sintered at 1500°C for (a) 0.1, (b) 0.5, (c) 1, and (d) 2 hours.

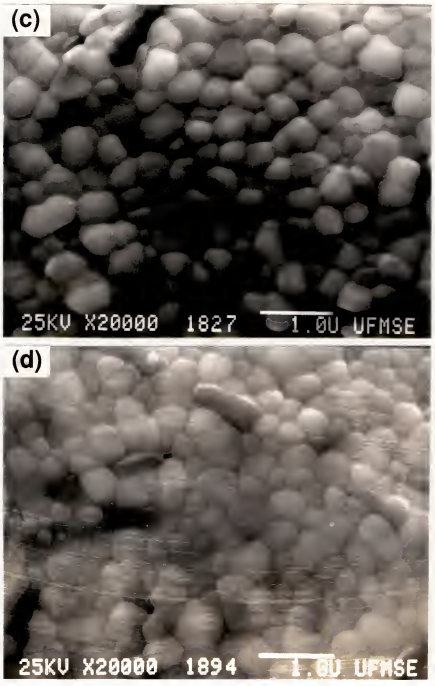

Figure 5.41 -- Continued.

exponents. Therefore, the slope for the Y-TZP can be estimated to be 0.2, which corresponds to a kinetic exponent of 5 (a $t^{1/5}$ dependence of grain growth).

The effect of Al_2O_3 addition on the ZrO_2 grain growth is presented in Figure 5.40, showing that the data for the Y-TZP/Al_2O_3 fibers appear to be more scattered than those for the Y-TZP fibers. The slope of the two lines are 0.18 and 0.20, corresponding to the grain growth kinetic exponent of 5, as in the case of the Y-TZP fibers.

The kinetic exponents for both of the fibers suggest that the rate-controlling mechanisms of the ZrO_2 grain boundary migration are very similar. The kinetic exponents determined in this study are greater than the 2 or 3 which is generally observed for single phase microstructures [Cob61, Ben85]. The larger kinetic exponent is indicative of a more stable microstructure (more stable in grain size or more resistant to grain growth). The kinetic exponent values have been related to processes controlled by intrinsic grain boundary migration in pure systems, by porosity, or by solute drag effects on the grain boundary mobility and liquid-phase controlled processes.

There are no data for the Y-TZP and Y-TZP/Al_2O_3 bulk ceramics directly comparable to the grain growth of the ZrO_2 on the fibers. Tien and Subbarao [Tie63] found a kinetic exponent value of 2.5 for the grain growth in a CaO fully-stabilized ZrO_2 (CSZ), but did not give a satisfactory explanation for the mechanism. Dou et al. [Dou85] observed a kinetic exponent of 3 for CSZ containing a liquid phase at 1510°C for up to 230 hours, and suggest that the grain growth is limited by diffusion of Zr^{4+}

ions through the liquid phase. Hori et. al [Hor85] have found the growth kinetic exponent of 4 in Al_2O_3/ZrO_2 composites, where grain growth of Al_2O_3 is inhibited by ZrO_2 inclusions, and proposed that the growth inhibition is attributed to the surface-diffusion-controlled inclusion drag and is analogous to pore drag. Comparable to the present systems is the kinetic exponent of 5 in porous Al_2O_3 compacts reported by Nichols [Nic66], who proposed that grain growth is controlled by the grain boundary drag effect exhibited by pores within which material is transported by surface diffusion on the pore surface. Although substantial porosity was not observed on the fiber surfaces, the grain growth of the ZrO_2 probably is controlled by surface diffusion which is also responsible for the thermal grooving of grain boundaries.

Although the grain growth data are limited to two temperatures, an attempt was made to obtain the activation energies for the grain growth. From the estimated kinetic exponents at 1400° and 1500°C, the activation energies were calculated by plotting log (G^n/t) versus 1/T and by determining the slopes. The data at 1200° and 1300°C for 1 hour heat treatment, as shown in Figure 5.36, were included in the plot. Figure 5.42 shows the plot where the kinetic exponent of 5 is utilized. The activation energies for the Y-TZP and Y-TZP/Al_2O_3 fibers were found to be 339 and 661 KJ/mole, respectively. The activation energies for the Y-TZP and Y-TZP/Al_2O_3 fibers and some of the previously published values are listed in Table 5.6. In ZrO_2 ceramics, the rate-controlling species are considered to be cations, zirconium and other stabilizing cations, because the cation diffusion rates are several orders of magnitude lower than for the oxygen ion, as shown in Table 5.6 [Rho66].

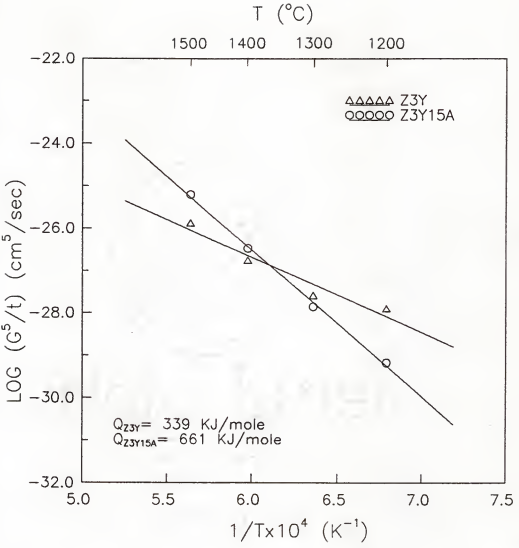

Figure 5.42. Temperature dependence of growth of zirconia grain on surfaces of sintered Y-TZP (3 mol% Y_2O_3) and Y-TZP/Al_2O_3 (3 mol% Y_2O_3 and 15 wt% Al_2O_3) fibers.

TABLE 5.6

Activation Energies for Zirconia Systems

Species and systems	Activation energy (KJ/mole)	Reference
Ca^{2+} in $Ca_{0.16}Zr_{0.84}O_{1.84}$	458	[Rho66]
Zr^{4+} in $Ca_{0.16}Zr_{0.84}O_{1.84}$	458	[Rho66]
O^{2-} in $Ca_{0.15}Zr_{0.85}O_{1.85}$	125	[King59]
Grain growth in $Ca_{0.16}Zr_{0.84}O_{1.84}$	336	[Tie63]
Growth of grain-boundary grooves on Y_2O_3-stabilized ZrO_2	340	[Wu84]
Grain growth on Y-TZP fiber surfaces	339	Present study
Grain growth on Y-TZP/Al_2O_3 fiber surfaces	661	Present study

The activation energies determined in this study are not certain due to the limited data. However, the activation energy for the Y-TZP fibers was found to be in agreement with those reported by Tien and Subbarao and, especially, by Wu and Brook [Wu84], who studied the surface diffusion from boundary grooving on Y_2O_3-stabilized ZrO_2 bicrystals. This suggests that the grain growth of the ZrO_2 is controlled by surface diffusion.

The slow grain growth of ZrO_2 (large kinetic exponent) in the Y-TZP fibers can be attributed primarily to the slow diffusion of cations at firing temperatures. The presence of the liquid phase at the boundaries at higher temperatures may complicate the grain growth process [Ger85, Kin76]. If a small amount of boundary liquid is formed, it tends to slow grain growth, since the driving force is reduced and the diffusion path across the boundary is increased. There are two solid-liquid interfaces and the driving force which is the difference in the interface energy between them is smaller than either alone. In addition, if the liquid wets the boundary, the interface energy must be lower than the pure grain boundary energy. Therefore, the liquid phase provides a continuous, low diffusivity path across the boundaries which then acts to inhibit the boundary migration.

The activation energy may differ depending on the additives or second phases. The presence of a liquid phase in which matrix grains are soluble may facilitate mass transfer by a soultion-precipitation mechanism, thus increasing the rate of grain growth with increasing temperature [Tie63].

It should be noted that the effect of the liquid phase mentioned above would be different in sintering, because the grain growth involves materials transport across the grain boundary while the sintering involves transport along the boundary (grain boundary diffusion). For sintering, the grain boundary diffusion path is not blocked, enhancing the densification of the fibers.

The activation energy for grain growth of ZrO_2 in the Y-TZP/Al_2O_3 fibers suggests that the mass transport across the boundary is hindered due to the presence of Al_2O_3, the liquid phase, and perhaps other phases on the fiber surfaces. However, the reason for the larger activation energy for the Y-TZP/Al_2O_3 fibers as opposed to the Y-TZP fibers is not understood. Since the estimated kinetic exponents for both fibers are the same, the activation energy for the Y-TZP/Al_2O_3 fibers is expected to be identical to that of the Y-TZP fibers. Considering the scattered and limited data, more rigorous experiments are necessary to determine the slopes with certainty. The grain growth kinetics should be studied over a wide range of temperatures and using grain sizes from the interior of the fibers to compare with data for bulk samples.

High-Temperature Stability of Y-TZP/Al_2O_3 Fibers

Thermal stability of the fibers is one of the most important considerations in the present study. Under prolonged use at high temperature, microstructural and phase changes can deteriorate mechanical properties of the fibers. Grain growth continues until the grains reach a stable grain boundary configuration, where the grains become so large that their boundaries span the width of the fiber. In this case, the boundaries

have no curvature and cannot migrate. Eventually, the mass transport associated with grain growth causes the grain boundary grooves to deepen, breaking a continuous fiber into a row of individual particles [Mil89].

High-temperature stability of the microstructure and phases in the Y-TZP/Al_2O_3 fibers was studied by heat treating at 1400° and 1500°C. Figures 5.43 and 5.44 show the X-ray diffraction patterns of the Y-TZP fibers containing 3 mol% Y_2O_3 and the Y-TZP/Al_2O_3 fibers containing 3 mol% Y_2O_3 and 15 wt% Al_2O_3, and held at 1400°C for 24 hours and at 1500°C for 6 hours, respectively. The insets are peaks corresponding to the (400) and (004) tetragonal reflections and the (400) cubic reflection. After 24 hours at 1400°C, all fibers contained tetragonal ZrO_2 and a small amount of monoclinic ZrO_2. In addition, cubic ZrO_2 appeared, as shown in the insets of Figure 5.43 (a) and (b). After 6 hours at 1500°C, the cubic ZrO_2 phase also appeared in both fibers, as shown in the Figure 5.44 (a) and (b). The Y-TZP fibers contained a small amount of monoclinic ZrO_2 along with tetragonal ZrO_2, whereas the Y-TZP/Al_2O_3 fibers did not contain the monoclinic ZrO_2 phase.

The appearance of the cubic ZrO_2 was associated with exaggerated grain growth. Figures 5.45 and 5.46 represent the distribution of ZrO_2 grain intercept sizes, illustrating the effect of Al_2O_3 inclusions on the exaggerated grain growth on the surfaces of the Y-TZP fibers. Heat treating the Y-TZP fibers at 1400°C for 24 hours resulted in a smaller mean grain intercept size of ZrO_2 than that of the Y-TZP/Al_2O_3 fibers, as shown in Figure 5.45 (a) and (b). At 1400°C, the distribution of the ZrO_2 grains in the Y-TZP/Al_2O_3 fibers was broadened, as compared with that of the Y-TZP

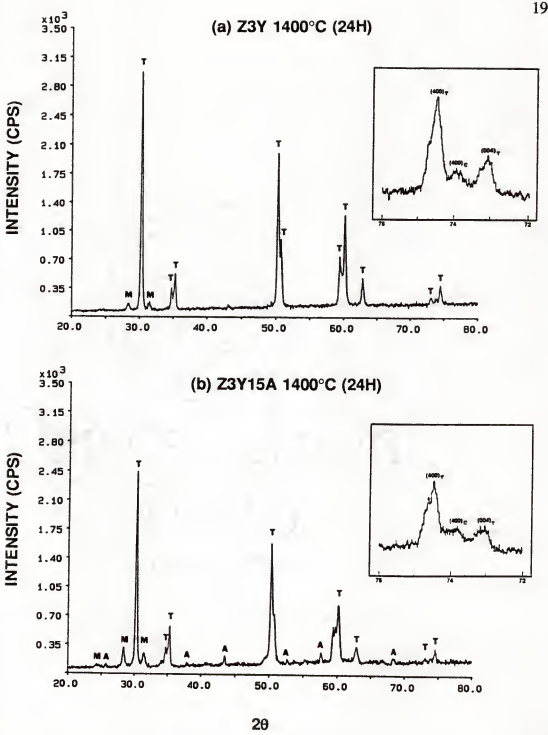

Figure 5.43. X-ray diffraction patterns of (a) Y-TZP (3 mol% Y_2O_3) and (b) Y-TZP/Al_2O_3 (3 mol% Y_2O_3 and 15 wt% Al_2O_3) fibers after maintaining at 1400°C for 24 hours in air. The insets are peaks corresponding to the (400) and (004) tetragonal ZrO_2 reflections and the (400) cubic ZrO_2 reflection.

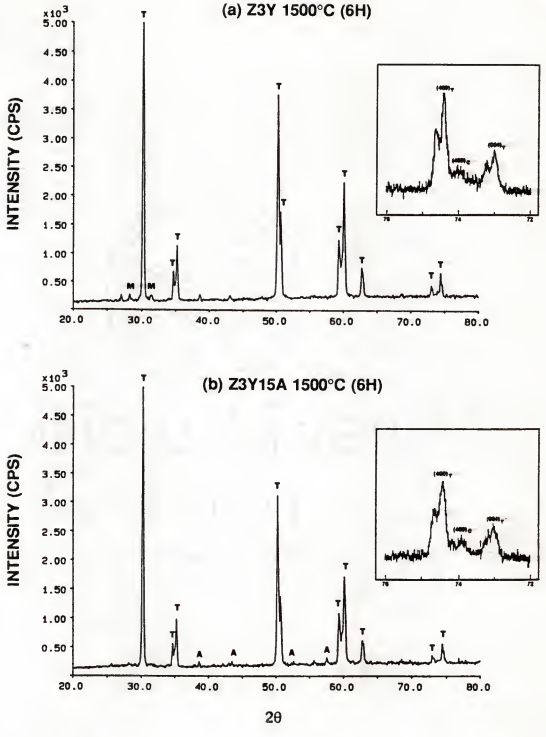

Figure 5.44. X-ray diffraction patterns of (a) Y-TZP (3 mol% Y_2O_3) and (b) Y-TZP/Al_2O_3 (3 mol% Y_2O_3 and 15 wt% Al_2O_3) fibers after maintaining at 1500°C for 6 hours in air. The insets are peaks corresponding to the (400) and (004) tetragonal ZrO_2 reflections and the (400) cubic ZrO_2 reflection.

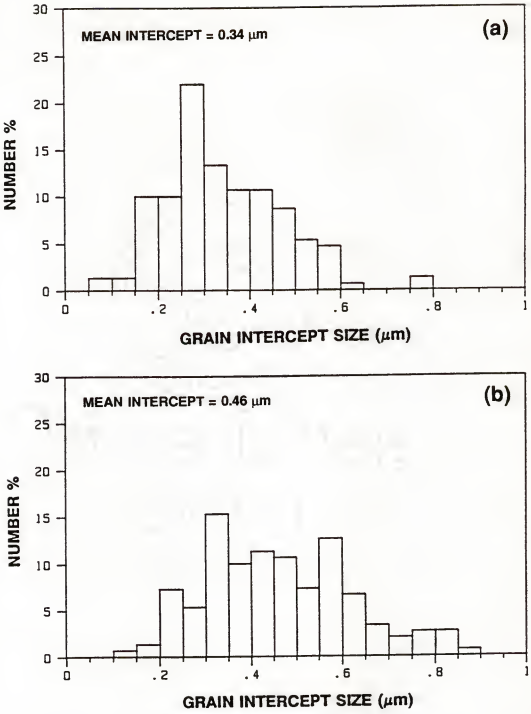

Figure 5.45. Distribution of grain intercept size of zirconia in (a) Y-TZP (3 mol% Y_2O_3) and (b) Y-TZP/Al_2O_3 (3 mol% Y_2O_3 and 15 wt% Al_2O_3) fibers after maintaining at 1400°C for 24 hours in air.

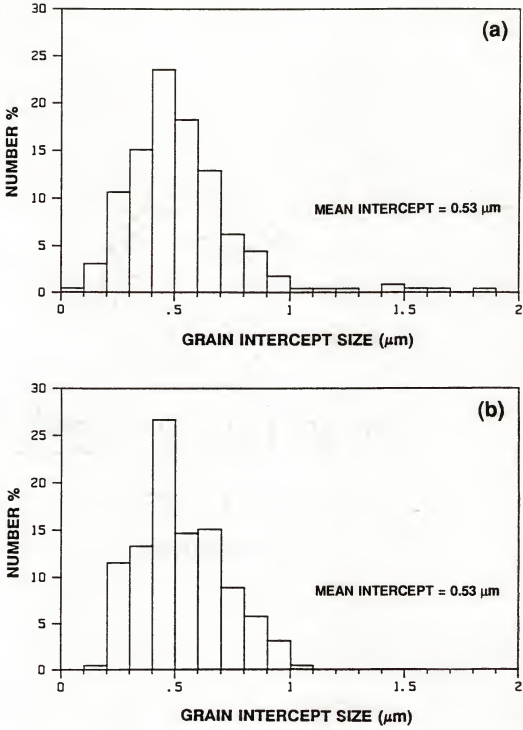

Figure 5.46. Distribution of grain intercept size of zirconia in (a) Y-TZP (3 mol% Y_2O_3) and (b) Y-TZP/Al_2O_3 (3 mol% Y_2O_3 and 15 wt% Al_2O_3) fibers after maintaining at 1500°C for 6 hours in air.

fibers. This indicates that the Al_2O_3 inclusions after 24 hour heat treatment do not retard grain growth of ZrO_2 but do prevent exaggerated grain growth. Heat treating at higher temperatures (1500°C) showed a pronounced effect of the Al_2O_3 inclusions in preventing exaggerated grain growth. After holding at 1500°C for 6 hours, the Y-TZP fibers exhibited an extensive exaggerated grain growth, as shown in Figure 5.46 (a). On the other hand, the Y-TZP/Al_2O_3 fibers showed the same mean grain intercept size as that of the Y-TZP fibers, more uniform distribution of grain sizes and did not show exaggerated grain growth.

Scanning electron micrographs in Figures 5.47 and 5.48 show the surfaces of the fibers tested at 1400° and 1500°C. Exaggerated grain growth in the Y-TZP fibers at these temperatures is shown in Figures 5.47 (a) and 5.48 (a). The large grains appear to grow by coalescence of neighboring grains, as shown in Figure 5.48 (a). In contrast to the Y-TZP fibers, the Y-TZP/Al_2O_3 fibers in Figures 5.47 (b) and 5.48 (b) consist of uniform-sized ZrO_2 grains. The morphology of the Al_2O_3 particles do not change after heat treatment.

It was found in the previous section that the elongated Al_2O_3 particles are not effective in inhibiting growth of small ZrO_2 grains at temperatures above 1400°C. The results shown by distribution of grain intercept sizes and SEM micrographs, however, suggest that the Al_2O_3 particles are effective in suppressing exaggerated growth of ZrO_2 grains when the ZrO_2 grain sizes become comparable to the Al_2O_3 particle sizes, although the Al_2O_3 particles are elongated. During the densification process above 1400°C, the ZrO_2 grain boundary moves fast. When the ZrO_2 grains become large

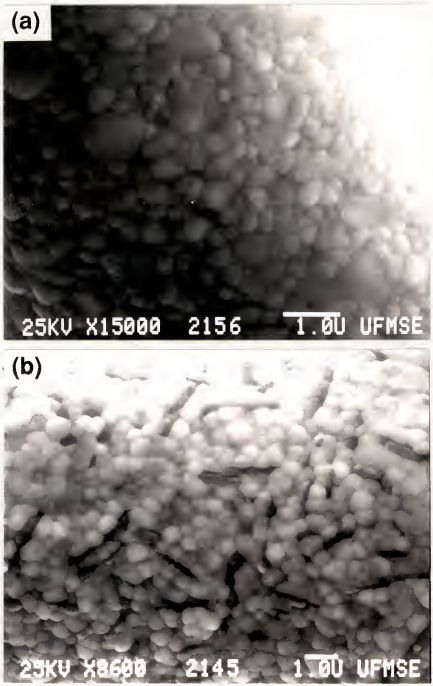

Figure 5.47. Scanning electron micrographs of (a) Y-TZP (3 mol% Y_2O_3) and (b) Y-TZP/Al_2O_3 (3 mol% Y_2O_3 and 15 wt% Al_2O_3) fibers maintained at 1400°C for 24 hours in air.

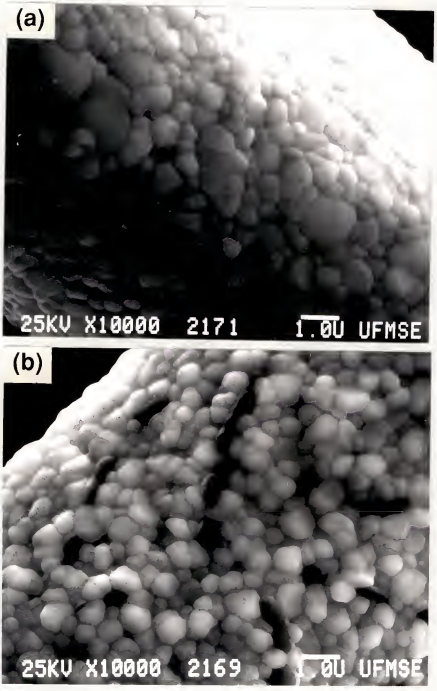

Figure 5.48. Scanning electron micrographs of (a) Y-TZP (3 mol% Y_2O_3) and (b) Y-TZP/Al_2O_3 (3 mol% Y_2O_3 and 15 wt% Al_2O_3) fibers maintained at 1500°C for 6 hours in air.

with increasing heat treatment time, the boundary migration is relatively slow and the Al_2O_3 particles can retard the boundary mobility by particle pinning.

The large grains in the fibers is the cubic ZrO_2 phase which is commonly observed in Y-TZP bulk ceramics [Mat84, Rüh84]. The formation of cubic ZrO_2 in the Y-TZP fibers during high-temperature heat treatment can be attributed to two processes occurring simultaneously and involving the diffusion of yttrium [Cha86,Wha87]. The first process is the partitioning of the Y-TZP into Y_2O_3-rich and Y_2O_3-poor phases throughout the fibers, since the composition of the Y-TZP fiber (3 mol% Y_2O_3) lies close to a two-phase field (tetragonal and cubic ZrO_2 solid solutions) of the ZrO_2-Y_2O_3 phase diagram (Figure 2.15). It should be mentioned that, due to the slow diffusion of cations in ZrO_2, the tetragonal ZrO_2 phase present in the sintered fibers is not in equilibrium and may change to equilibrium phases with increasing heat treatment time. The second process is the non-equilibrium migration of yttrium to the surface which causes a composition change, resulting in a microstructure and phase composition different from the bulk [Cha86, Wha87].

The TEM observations for the TZP/Al_2O_3 fibers suggest that the migration of yttrium is due to a liquid phase at the grain boundaries. Figures 5.49 show a liquid phase at the grain boundaries and triple points in the Y-TZP/Al_2O_3 fibers heat treated at 1500°C for 6 hours. A glassy phase is seen at the grain junction between ZrO_2 grains or between ZrO_2 and Al_2O_3 grains (Figure 5.49 (a)). A thin intergranular film is also observed at the boundary between ZrO_2 and Al_2O_3 grains (Figure 5.49 (b)). The Al_2O_3 particles are elongated due to the excess liquid at the triple joints near

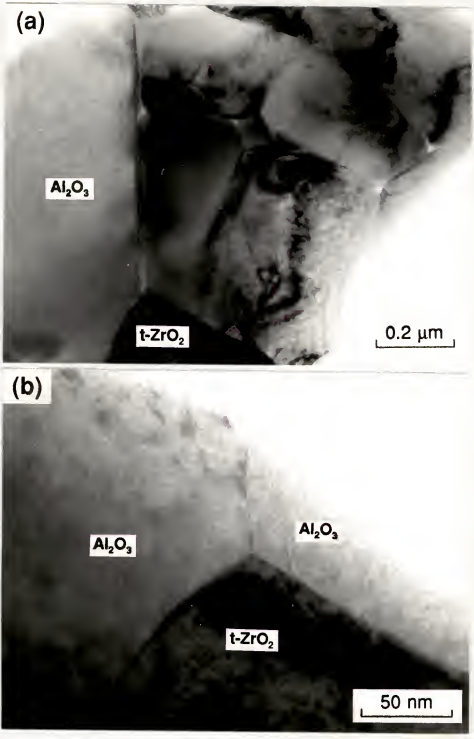

Figure 5.49. Transmission electron micrographs of Y-TZP/Al_2O_3 fibers containing 3 mol% Y_2O_3 and 15 wt% Al_2O_3 after maintaining at 1500°C for 6 hours in air, showing (a) pockets formed between zirconia grains, and zirconia and alumina grains and (b) an intergranular film between zirconia and alumina grains.

faceted Al_2O_3 grain sides (Figure 5.49 (a)), as discussed in the previous section. Whalen et al. [Wha87] have proposed that yttrium, which is dissolved in a glassy phase in a bulk Y-TZP, diffuses back into the grains at the surface, resulting in tetragonal ZrO_2 grains with a high yttrium content close to that of the cubic ZrO_2. The increase in SiO_2 content at the surface of the Y-TZP containing a large quantity of SiO_2 coincided with surface Y_2O_3 enrichment. Chaim et al. [Cha86] also found the surface segregation of an iron-rich silicate from a bulk Y-TZP and reported that the tetragonal to cubic phase transformation resulted from dissolution of tetragonal grains and the subsequent crystallization of cubic grains (large grains grew abnormally by a solution-diffusion-reprecipitation process involving a liquid grain boundary phase). It can be seen that, in the Y-TZP fibers, the large cubic ZrO_2 grains form from the tetragonal grains wet by the liquid phase rich in yttrium which grow into Y_2O_3-rich phase and further grow into large grains by coalescence, as seen in Figures 5.47 (a) and 5.48 (a).

The suppressed exaggerated grain growth of ZrO_2 can be attributed not only to grain boundary pinning, but also to the Al_2O_3 particles hindering dissolution of yttrium in the liquid phase. Butler and Drennan [But82] proposed that Al_2O_3 particles act as scavengers for intergranular SiO_2. They stated that, as ZrO_2 grain boundaries move past the Al_2O_3 particles, the intergranular SiO_2 diffuses rapidly to the Al_2O_3 particles due to the greater affinity of SiO_2 for Al_2O_3 than for ZrO_2, forming SiO_2-rich cusps on the Al_2O_3 inclusions. Thus, more liquid phase is accumulated around the Al_2O_3 particles than the ZrO_2 grains. This leads to the clean grain boundary between ZrO_2

grains, making the solution-precipitation of Y_2O_3 more difficult. However, this effect could not be confirmed unambiguously because the liquid phase was found around the ZrO_2 grains as well as the Al_2O_3 particles.

CHAPTER VI
CONCLUSIONS

1. Rheological properties of a colloidal ZrO_2 sol containing yttrium and aluminum nitrates and PVA were investigated with respect to sol concentration, aging and aluminum nitrate content. Shear viscosities were measured in an attempt to relate them to spinnability. During the evaporation (concentration) process, a small addition of yttrium nitrate (equivalent to 2 mol% Y_2O_3) had little effect on the viscosity of the sol, whereas the addition of aluminum nitrate precursor resulted in a more rapid increase in viscosity than the sols without aluminum nitrate precursor. Aging the sols containing the additives at room temperature did not noticeably change the sol viscosity up to 30 days.

2. Spinnability was obtained by adding 2 wt% PVA (75% hydrolyzed) with low molecular weight (2,000 m.w.) which increases the sol viscosity to a range of optimum values ($1\text{-}6\times10^4$ mPa·s) for centrifugal spinning. As the aluminum nitrate content increased to greater than that equivalent to 16.7 wt% Al_2O_3, the sol lost its spinnability. Flow behavior of the sols progressively changed from Newtonian to shear-thinning with increasing sol concentration. The shear-thinning sols exhibited spinnability.

3. Discontinuous, fine-grained Y-TZP/Al_2O_3 fibers having composite microstructures with >99% relative density were produced by centrifugal spinning and sintering up to 1500°C. The distribution and shape of Al_2O_3 particles in the Y-TZP fibers were determined by the thermal history of the fibers. The Al_2O_3 particles were uniformly distributed in the ZrO_2 matrix at low sintering temperatures (<1400°C). As sintering temperatures increased, the Al_2O_3 particles were elongated due to the presence of a small amount of intergranular liquid phase. The elongated Al_2O_3 particles were ≈0.3 μm wide with an aspect ratio >3 at 1500°C and randomly distributed with a localized grain alignment.

4. The addition of Al_2O_3 in amounts greater than 10 wt% retarded the growth of ZrO_2 crystallites at temperatures ranging up to 1200°C. Alumina was not effective in suppressing the tetragonal to monoclinic transformation of ZrO_2 in Y-TZP fibers containing 2 mol% Y_2O_3. The addition of 15 wt% Al_2O_3 inhibited grain growth of ZrO_2 on the fiber surfaces at temperatures up to 1400°C. Above this, coarsening of the Al_2O_3 particles diminished the effectiveness of the inclusions in inhibiting grain growth of ZrO_2.

5. The grain growth kinetic exponents for the ZrO_2 grains on the surfaces of the fibers at 1400° and 1500°C were found to be approximately 5 for both Y-TZP and Y-TZP/Al_2O_3 fibers.

6. Alumina addition enhanced the high-temperature microstructural stability of the fibers with respect to exaggerated grain growth of ZrO_2. Addition of Al_2O_3 suppressed the formation of large cubic grains on the surfaces of the Y-TZP fibers.

The large cubic ZrO_2 grains were found in the Y-TZP fibers tested above 1400°C and their formation was extensive after heat treating at 1500°C for 6 hours. Whereas, the large cubic ZrO_2 grains were not found in the Y-TZP/Al_2O_3 fibers tested under identical conditions and a more uniform microstructure resulted.

CHAPTER VII
SUGGESTIONS FOR FURTHER WORK

1. The results of FT-IR analysis did not provide a clear indication of interactions between the ZrO_2 sol and the additives. There appeared to be no well-defined differences in FT-IR spectra between the dilute sols and the concentrated spinnable sols. Further work is necessary using either more sensitive FT-IR or NMR.

2. In order to clarify the grain growth mechanisms of ZrO_2, the grain growth kinetics of ZrO_2, including Al_2O_3, should be studied over a wider range of temperatures and using grain sizes from the interior of the fibers to compare with data for bulk samples.

3. The results of TEM study showed the presence of an intergranular liquid phase. However, the formation temperature, amount and composition of the liquid phase could not be determined due to the spacial resolution of the TEM. In order to clearly examine the grain boundary microstructure of the fibers, a high resolution TEM should be used. Since the intergranular liquid phase can influence high-temperature strength, the use of high purity precursors is recommended to eliminate the liquid phase.

4. Although the present research was aimed at the fabrication of discontinuous fibers using centrifugal spinning on a small scale, several attempts were made to

produce continuous fibers from the Y-TZP/Al_2O_3 sols. Preliminary results from these first runs indicate that continuous fibers can be made, but "fine-tuning" of the sol system will be required to fabricate fibers suitable for use in high performance composites.

5. Elongational flow behavior of sols should be considered in continuous fiber fabrication. Processing variables for fiber spinning cannot be understood in terms of shear flow behavior alone since the flow occurring during fiber spinning has an elongational component. A theoretical discussion regarding elongational flow behavior is presented in Appendix A.

6. A testing procedure for measuring room-temperature tensile strength and elastic modulus of single fibers of oxides was developed to aid with the future attempts to evaluate the room- and high-temperature mechanical properties of the Y-TZP/Al_2O_3 fibers. Preliminary test results from the Sumica fibers manufactured by Sumitomo Chemical Co. were in close agreement with reported values. Further improvements to this procedure are necessary to measure high-temperature properties of the fibers. However, before this can be accomplished, continuous fibers of uniform diameter and with fewer forming defects must be fabricated.

APPENDIX A
SHEAR AND ELONGATIONAL FLOW BEHAVIORS

Shear Flow Behavior

Viscosity is the property of the material that resists flow due to internal friction between its molecules. In a steady simple shear flow, a shear stress is required to initiate and maintain laminar flow. When a shear stress is linearly dependent on the velocity gradient or shear rate, the fluid is said to be Newtonian and the viscosity is defined as

$$\eta = \tau/\dot{\gamma}, \tag{A.1}$$

where η is viscosity, τ is shear stress and $\dot{\gamma}$ is shear rate. The flow velocity and stress distribution can be written in the form [Bar89]

$$\partial V_x/\partial y = \dot{\gamma},\ V_y = V_z = 0,$$
$$\sigma_{xz} = \sigma_{zy} = 0,\ \sigma_{xx} - \sigma_{yy} = 0,\ \sigma_{yy} - \sigma_{zz} = 0, \text{ and}$$
$$\sigma_{xy} = \eta\dot{\gamma} = \tau \text{ (constant)}, \tag{A.2}$$

where V_x, V_y, V_z are the velocity components in the x, y and z directions, respectively, and $\dot{\gamma}$ is the shear rate corresponding to the velocity gradient $\partial V_x/\partial y$.

Non-Newtonian fluids in shear flow may be classified as time-independent, time-dependent and viscoelastic fluids.

Time-independent non-Newtonian fluids are described by the form [Tan88]:

$$dV/dy = \eta = f(\dot{\gamma}), \tag{A.3}$$

which implies that the viscosity at any point in the fluid is a function of the shear rate at that point. Such fluids are divided into three distinct types and illustrated as a function of shear stress versus shear rate in Figure A.1.

Shear-thinning (Pseudoplastic) Fluids. The fluid exhibits a decrease in viscosity with increasing shear rate. This behavior is observed in liquids or suspensions when the alignment of anisotropic large molecules and particles or breakdown of the flocculated particles occur under shear stress. This behavior is often described by an empirical power law equation:

$$\eta = K(\dot{\gamma})^{n-1}, \tag{A.4}$$

where K and n are constants (n<1 for a pseudoplastic fluid): K is a measure of the consistency of the fluid, the higher K the more viscous the fluid; n is a measure of the degree of non-Newtonian behavior, and the greater the departure from unity the more pronounced the non-Newtonian behavior.

Shear-thickening (Dilatant) Fluids. These fluids exhibit an increase in viscosity with increasing shear rate are described as shear-thickening. The power-law equation is applicable but in this case the constant n is greater than unity.

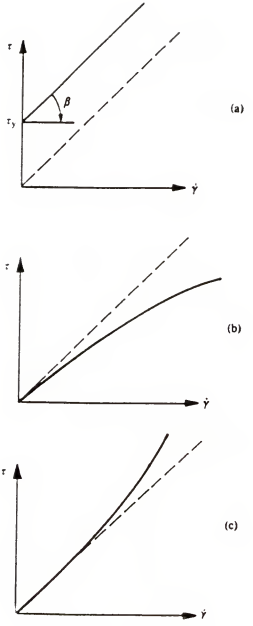

Figure A.1. Schematic plots of shear stress τ versus shear rate $\dot{\gamma}$ for (a) Bingham body, (b) shear-thinning (pseudoplastic) fluid and (c) shear-thickening (dilatant) fluid. Dashed lines show Newtonian behavior. τ_y is a yield stress and the tangent of the slope ß gives the incremental viscosity [Tan88].

Bingham plastics. The Bingham plastics are characterized by the flow which requires a finite stress called a yield stress to initiate the flow and then behaves as a Newtonian fluid. The behavior as shown in Figure A.1 (a) is called ideal plastic flow, a type of flow which is only approximated by real systems. In real systems, the curve near the zero shear rate deviates from linearity. For the linear part of the curve, the flow behavior is described by

$$\tau - \tau_y = \eta_p \dot{\gamma}, \tag{A.5}$$

where τ_y is the yield stress and η_p is the plastic viscosity.

Time-dependent non-Newtonian fluids may be subdivided as follows.

Thixotropic fluids. A gradual decrease of viscosity with increasing shear rate is followed by a gradual recovery of structure when shear stress is removed. Thixotropic behavior is usually observed in shear-thinning and Bingham plastic fluids where the breakdown of some loose structure in a flocculated system progressively occur under applied shear stress and the viscosity decreases with time. Figure A.2 illustrates the thixotropic behavior exhibiting a hysteresis loop.

Rheopectic fluids. Rheopectic fluids exhibit the opposite type of thixotropy, involving a gradual increase in viscosity under stress, followed by recovery of structure.

Viscoelastic fluids. Viscoelastic fluids have characteristics of both elastic solid and viscous fluid and exhibit a partial elastic recovery after deformation.

(a)

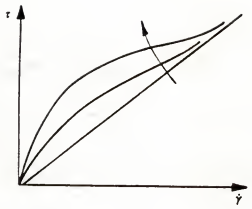

(b)

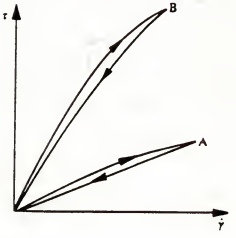

Figure A.2. Schematic illustration of shear stress τ versus shear rate $\dot{\gamma}$ for thixotropic behavior. (a) The curved arrow indicates the direction of increasing time that the sample has been recovering after a large shear rate was applied. The lowest curve was taken immediately after a large shear rate was applied. (b) Hysteresis loops for Newtonian type (curve A) and non-Newtonian type (curve B) of thixotropy. Arrow indicates the direction of the test [Tan88].

Elongational Flow Behavior

Suppose that a rod is being extended along its x-axis, so that the rod is stressed uniformly. Assuming that the elongational rate ($\partial V_x/\partial x$) at each section is independent of x and is a function of time, consideration of mass conservation and axial symmetry gives [Tan88]

$$\partial V_x/\partial x = \dot{\varepsilon},\ \partial V_y/\partial y = \partial V_z/\partial z = -\dot{\varepsilon}/2, \tag{A.6}$$

where V_x, V_y and V_z are the velocity components in x, y and z directions, respectively, and $\dot{\varepsilon}$ is a constant elongational strain rate. For incompressible fluids, the corresponding stress response is defined as

$$\sigma_{xy} = \sigma_{xz} = \sigma_{yz} = 0,\ \sigma_{yy} = \sigma_{zz}, \text{ and}$$
$$\sigma_{xx} - \sigma_{yy} = \dot{\varepsilon}\eta_E(\dot{\varepsilon},t), \tag{A.7}$$

where η_E is the (uniaxial) elongational viscosity. In general, it is a function of the elongational strain rate ($\dot{\varepsilon}$), just as the shear viscosity (η) is a function of shear rate ($\dot{\gamma}$) and time (t) elapsed since the stretching began. In a steady-state, the elongational viscosity is defined by $\eta_E(\dot{\varepsilon})$.

For non-Newtonian fluids, a relation between elongational and shear viscosities has been proposed [Bar89]

$$\eta_E(\dot{\varepsilon})\,|_{\dot{\varepsilon}\to 0} = 3\eta(\dot{\gamma})\,|_{\dot{\gamma}\to 0}\,. \tag{A.8}$$

In particular, for Newtonian fluids, the equation (A.8) is valid for all values of $\dot{\varepsilon}$ and $\dot{\gamma}$, and hence $\eta_E = 3\eta$: the result was obtained by Trouton and is valid for highly viscous Newtonian materials. The Trouton ratio is defined as

$$T_R = \frac{\eta_E(\dot{\varepsilon})}{\eta(\dot{\gamma})} \tag{A.9}$$

but the definition is somewhat ambiguous since the Trouton ratio depends on both $\dot{\varepsilon}$ and $\dot{\gamma}$.

The following definition has been proposed for a non-Newtonian fluid to relate the strain rates in elongation and shear and to estimate viscoelastic effects [Jon87]:

$$T_R(\dot{\varepsilon}) = \frac{\eta_E(\dot{\varepsilon})}{\eta(\sqrt{3}\dot{\varepsilon}).} \tag{A.10}$$

Jones et al. [Jon87] showed that if the flow is inelastic, T_R is 3 for all values of $\dot{\varepsilon}$. Any departure from the value 3 can be associated with viscoelasticity. The behavior of the elongational viscosity is frequently different from that of the shear viscosity. Shear-thinning solutions of highly elastic polymers often exhibit an elongational viscosity which increases dramatically with stress as shown in Figure A.3 [Bar89].

By analogy with shear deformation, three types of elongational flow behavior can be predicted [Bry81]:

(1) A fluid for which the elongational viscosity is independent of tensile stress and equal to three times shear viscosity is said to be Troutonian (or Newtonian).

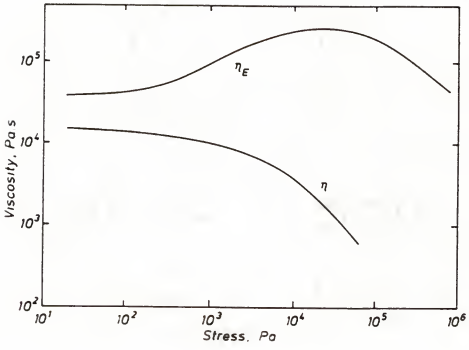

Figure A.3. Elongational viscosity (η_E) and shear viscosity (η) as a function of stress for the low-density polyethylene [Bar89].

(2) A fluid for which elongational viscosity increases with tensile stress is said to be tension-thickening (stiffening). This is analogous to shear-thickening (dilatancy) in shear flow.

(3) A fluid for which elongational viscosity decreases with increasing tensile stress is said to be tension-thinning. This is analogous to shear-thinning (pseudoplasticity) in shear flow. A shear-thinning fluid tends to exhibit tension-thinning in elongation, if viscoelastic effects are negligible or very small [Jon87].

Although the relations between tensile stress and elongational rate are somewhat simpler than for shear stress and shear rate, elongational flow analysis is very complex. The complexity is due to two main reasons. In elongational flow, a steady state situation is not achieved experimentally. Also, elastic components of deformation can make a much larger contribution than the corresponding shear stress deformation to the relationship between tensile stress, elongation and time. The elongational viscosity can be estimated by dividing the measured stress by an average value of the strain rate from fiber spinning experiments [McC88]. It is recognized, however, that the determination of elongational flow curves is not possible due to non-uniformity in flow and stresses along the cross-section of a fluid filament. The elongational viscosity measurements have not shown single-valued flow curves [Bar89].

Despite the difficulty in the meaningful interpretation of elongational viscosity measurements, it can provide a useful insight into spinning behavior. Cogswell [Cog81] has reported the elongational viscosities for two polymers, linear and

branched polyethylene. In Figure A.4 (a), both polymers show more or less Troutonian (Newtonian) behavior at low stress and their elongational viscosities approach asymptotically constant values. At stresses over 10^3 Pa, branched polyethylene shows tension-thickening, while linear polyethylene shows tension-thinning. The tension-thickening in branched polyethylene is attributed to the side branches acting as hooks which increase the resistance to flow when the molecules slide by each other as the liquid elongates. Tension-thickening also is observed in low density polyethylene. Linear polyolefins such as high density polyethylene, polypropylene, etc., show tension-thinning. Most polymers such as poly(methyl methacrylate), polystyrene, polycarbonate, nylon, etc., show Troutonian behavior.

Cogswell [Cog81] explained a filament breakup by considering the effect of an incipient neck which causes a stress concentration. Figure A.4 (b) illustrates the filament breakup behavior. At the incipient neck, the higher stress imposes a higher strain. If the liquid is either Troutonian or tension-thinning, the higher stress at the neck causes further thinning and in turn higher stresses, and so on. Eventially, the non-uniformity becomes progressively more marked and results in failure (necking). If the liquid is tension-thickening, the high local stress increases the elongational viscosity. The increased elongational viscosity compensates the extra stress arising from the neck. In this case, the non-uniformity does not increase and drawing is facilitated.

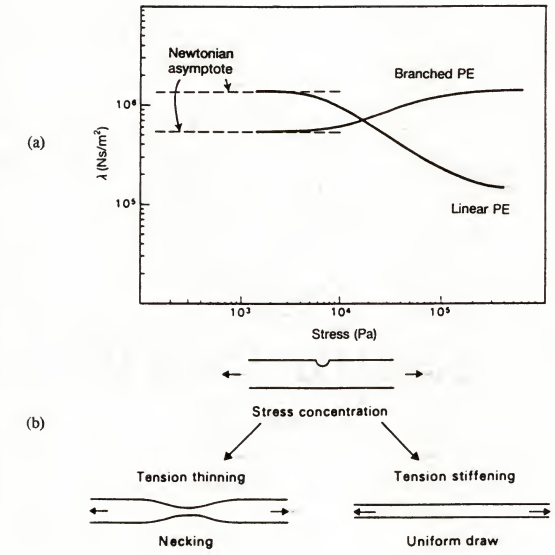

Figure A.4. The elongational flow and spinning behavior for branched and linear polyethylene. (a) The elongational viscosity versus tensile stress. (b) Illustration of the way in which tension-thickening liquids can be drawn without necking [Cog81].

REFERENCES

Abe82 Abe, Y., S. Horikiri, K. Fujimura, and E. Ichiki, "High-Performance Alumina Fiber and Alumina/aluminum Composites," Progress in Science and Engineering of Composites, Proceedings of the Fourth International Conference on Composite Materials, Edited by T. Hayashi, K. Kawate, and S. Umekawa, ICCM-IV, Japan Society for Composite Materials, Tokyo, Japan, 1982, pp. 1427-1434.

Ael50 Aelion, R., A. Loebel, and F. Eirich, "Hydrolysis of Ethyl Silicate," J. Am. Chem. Soc., 72, 5705-712 (1950).

Ash68 Ashby, M.F., and R.M.A. Centamore, "The Dragging of Small Oxide Particles by Migrating Grain Boundaries in Copper," Acta Metall., 16[9] 1081-92 (1968).

Bae76 Baes, C.B., Jr. and R.E. Mesmer, The Hydrolysis of Cations, John Wiley & Sons, Inc., New York, NY., 1976, pp. 112-138.

Bai72 Bailey, J.E., D. Lewis, Z.M. Librant, and L.J. Porter, "Phase Transformations in Milled Zirconia," Trans. J. Brit. Ceram. Soc., 71[1] 25-30 (1972).

Ban75 Bansal, G.K. and A.H. Heuer, "Precipitation in Partially Stabilized Zirconia," J. Am. Ceram. Soc., 58[5-6] 235-38 (1975).

Bar81 Barnes, H.A., Dispersion Rheology: 1980, Royal Soc. of Chem., Industrial Division, London, 1981.

Bar89 Barnes, H.A., J.F. Hutton, and K. Walters, An Introduction to Rheology, Elsevier Science Publishing Co. Inc., New York, NY., 1989.

Bat89 Bateman, C.A., S.J. Bennison, and M.P. Harmer, "Mechanism for the Role of Magnesia in the Sintering of Alumina Containing Small Amounts of a Liquid Phase," J. Am. Ceram. Soc., 72[7] 1241-44 (1989).

Bau69 Bauerle, J.E., "Study of Solid Electrolyte Polarization by a Complex Admittance Method," J. Phys. Chem. Solids, 30[12] 2657-70 (1969).

Bec54 Beck, P.A., "Annealing of Cold Worked Metals," Phil. Mag. Supplement, 3[11], 245-324 (1954).

Ben85 Bennison, S.J. and M.P. Harmer, "Grain Growth Kinetics for Alumina in the Absence of a Liquid Phase," J. Am. Ceram. Soc., 68[1] C-22-C-24 (1985).

Bet84 Better Ceramics Through Chemistry, Mat. Res. Soc. Symp. Proc. Vol. 32, Edited by C.J. Brinker, D.E. Clark, and D.R. Ulrich, Elsevier Science Publishing Co., Inc., New York, NY., 1984.

Bet86 Better Ceramics Through Chemistry II, Mat. Res. Soc. Symp. Proc. Vol. 73, Edited by C.J. Brinker, D.E. Clark, and D.R. Ulrich, Materials Research Society, Pittsburgh, PA., 1986.

Bet88 Better Ceramics Through Chemistry III, Mat. Res. Soc. Symp. Proc. Vol. 121, Edited by C.J. Brinker, D.E. Clark, and D.R. Ulrich, Materials Research Society, Pittsburgh, PA., 1988.

Bir83 Birchall, J.D., "The Preparation and Properties of Polycrystalline Aluminum Oxide Fibres," Trans. J. Br. Ceram. Soc., 82, 143-45 (1983).

Bir85 Birchall, J.D., J.A.A. Bradbury, and J. Dinwoodie, "Alumina Fibres: Preparation, Properties, and Applications," Handbook of Composites, vol. 1, Strong Fibres, Edited by W. Watt and B.V. Perov, Elsevier Science Publishers, Amsterdam, The Netherlands, 1985, pp. 117-154.

Blu58 Blumenthal, W.B., The Chemical Behavior of Zirconium, D. Van Nostrand Co. Inc., Princeton, NJ., 1958.

Bon88 Bond, W.D. and P.F. Becher, "Synthesis of Alumina-Zirconia Powders By Sol-Gel Processing," Ultrastructure Processing of Advanced Ceramics, Edited by J.D. Mackenzie and D.R. Ulrich, John Wiley & Sons, Inc., New York, NY., 1988, pp. 443-452.

Bra84 Bracke, P., H. Schurmans, and J. Verhoest, Inorganic fibers and Composite Materials, A Survey of Recent Developments, Pergamon Press, Oxford, UK, 1984

Brad78 Bradley, D.C., R.C. Mehrotra, and D.P. Gauer, Metal Alkoxides, Academic Press, New York, NY., 1978.

Bri85 Brinker, C.J. and G.W. Scherer, "Sol→Gel→Glass: I. Gelation and Gel Structure," J. Non-Cryst. Solids, 70, 301-322 (1985).

Bro76 Brook, R.J., "Controlled Grain Growth," Treatise on Materials Science and Technology, vol. 9, Ceramic Fabrication Processes, Edited by F.F. Wang, Academic Press, New York, NY., 1976, pp. 331-64.

Bry81 Brydson, J.A., Flow Properties of Polymer Melts, George Godwin Limited, London, 1981, pp. 104-107.

Buc84 Buchanan, R.C. and D. M. Wilson, "Role of Al_2O_3 in Sintering of Submicrometer Yttria-Stabilized ZrO_2 Powders," Advances in Ceramics vol. 12, Science and Technology of Zirconia II, Edited by N. Claussen, M. Rühle, and A.H. Heuer, The American Ceramic Society, Columbus, OH., 1984, pp. 526-540.

But82 Butler, E.P. and J. Drennan, "Microstructural Analysis of Sintered High-Conductivity Zirconia with Al_2O_3 Additions," J. Am. Ceram. Soc., 65[10] 474-78 (1982).

Cas59 Casson. N., "A Flow Equation for Pigment-Oil Suspensions of the Printing Ink Type," Rheology of Disperse Systems, Edited by C.C. Mill, Pergamon Press, New York, NY., 1959, pp. 84-104.

Cha86 Chaim, R., D.G. Brandon, and A.H. Heuer, "A Diffusional Phase Transformation in ZrO_2-4 wt% Y_2O_3 Induced by Surface Segregation," Acta Metall., 34[10] 1933-39 (1986).

Chan79 Chang, J.C. and M.M. Denn, "An Experimental Study of Isothermal Spinning of a Newtonian and a Viscoelastic Liquid," J. Non-Newtonian Fluid Mech., 5, 369-85 (1979).

Cim83 Ciminelli, R.R., Synthesis of Alumina from $Al(NO_3)_3 \cdot 9H_2O$ by Evaporative Decomposition of Solution Process, M.S. Thesis, The Pennsylvania State University, University Park, PA., 1983.

Cla81 Clarke, J. and B. Vincent, "Stability of Non-aqueous Microgel Dispersions in the Presence of Free Polymer," J. Chem. Soc., Faraday Trans. I, 77, 1831-843 (1981).

Cle56 Clearfield, A. and P.A. Vaughan, "The Crystal Structure of Zirconyl Chloride Octahydrate and Zirconyl Bromide Octahydrate," Acta Cryst., 9, 555-558 (1956).

Clo85 Clough, D.J., "ZrO_2 Powders for Advanced and Engineered Ceramics," Ceram. Eng. Sci. Proc., 6[9-10] 1244-60 (1985).

Cob61 Coble, R.L., "Sintering Crystalline Solids: II, Experimental Test of Diffusion Models in Powder Compacts," J. Appl. Phys., 32[5] 793-99 (1961).

Cog81 Cogswell, F.N., Polymer Melt Rheology, George Godwin, London, 1981.

Dah83 Dahar, S., Controlled Viscosity Tetraethyl-Orthosilicate Sols for Fiber Spinning, M.S. Thesis, Alfred University, Alfred, NY., 1983.

Deb86 Debsikdar, J.C., "Thermal Evolution of Alkoxy-Derived "Glass-Like" Transparent Zirconia Gel," J. Non-Cryst. Solids, 87, 343-49 (1986).

Den80 Denn, M.M.,"Continuous Drawing of Liquids to Form Fibers," Ann. Rev. Fluid Mech., 12, 365-87 (1980).

Dhi80 Dhingra, A.K., "Alumina Fiber FP," Philos. Trans. R. Soc. London, A294, 411-17 (1980).

DiC85 DiCarlo, J.A., "Fibers for Structurally Reliable Metal and Ceramic Composites," Journal of Metals, 6, 44-49 (1985).

Doe87 Doeuff, S., M. Henry, C. Sanchez, and J. Livage, "Hydrolysis of Titanium Alkoxides: Modification of the Molecular Precursor By Acetic Acid," J. Non-Cryst. Solids, 89, 206-16 (1987).

Don76 Donald, I.W. and P.W. McMillan, "Review Ceramic-Matrix Composites," J. Mater. Sci., 11, 949-72 (1976).

Dou85 Dou, S., P.D. Pacey, C.R. Masson, and B.R. Marple, "Grain Growth in CaO-Stabilized ZrO_2 in the Presence of a Liquid Phase," J. Am. Ceram. Soc., 68[3] C-80-C-81 (1985).

Dre86 Drennan, J. and R.H.J. Hannink, "Effect of SrO Additions on the Grain-Boundary Microstructure and Mechanical Properties of Magnesia-Partially-Stabilized Zirconia," J. Am. Ceram. Soc., 69[7] 541-46 (1986).

Dwo84 Dworak, U., H. Olapinski, D. Fingerle, and U. Krohn, "ZrO_2 Ceramics for Internal Combustion Engines," Advances in Ceramics vol. 12, Science and Technology of Zirconia II, Edited by N. Claussen, M. Rühle, and A.H. Heuer, The American Ceramic Society, Columbus, OH., 1984, pp. 480-487.

Ein06 Einstein, A., "A New Determination of Molecular Dimension," Ann. Physik, 19, 289-306 (1906).

Ein11 Einstein, A., "Correction in My Work: A New Determination of Molecular Dimension," Ann. Physik, 34, 591-592 (1911).

Eve88 Everitt, G.F., "Stabilized Aluminum Acetate Used for an Alumina Source in Ceramic Fibers," Ultrastructure processing of Advanced Ceramics, Ed. by J.D. Mackenzie and D.R. Ulrich, John Wiley & Sons, Inc., New York, NY., 1988, pp. 463-476.

Fit88 Fitzer, E., "Ceramic and Coated Carbon Fibres for High Temperature Ceramics," Whisker- and Fiber-Toughened Ceramics, Proceedings of an International Conference, Oak Ridge, TN., 1988, Edited by R.A. Bradley, D.E. Clark, D.C. Larsen, and J.O. Stiegler, ASM International,™ pp. 9-52.

Fitz86 Fitzer, E. and R. Gadow, "Fibre Reinforced Composites vis the Sol/Gel Route," Tailoring Multiphase and Composite Ceramics, Mat. Sci. Res. Vol. 20, Edited by R.E. Tressler, G.L. Messing, C.G. Pantano, and R.E. Newnham, Plenum Press, New York, NY., 1986, pp. 571-607.

Gad75 Gadsden, J.A., Infrared Spectra of Minerals and Related Inorganic Compounds, Butterworths & Co Ltd., London, 1975.

Gar65 Garvie, R.C., "The Occurence of Metastable Tetragonal Zirconia as a Crystallite Size Effect," J. Phys. Chem., 69[4] 1238-43 (1965).

Garv84 Garvie, R.C., "Structural Applications of ZrO_2-Bearing Materials, Advances in Ceramics vol. 12, Science and Technology of Zirconia II, Edited by N. Claussen, M. Rühle, and A.H. Heuer, The American Ceramic Society, Columbus, OH., 1984, pp. 465-479.

Garvi75 Garvie, R.C., R.H. Hannink, and R.T. Pascoe, "Ceramic Steel?," Nature, 258, 703-704 (1975).

Ger85 German, R.M., Liquid Phase Sintering, Plenum Press, New York, NY., 1985, pp. 127-155.

Goo87 Goodwin, N.J., "The Rheology of Colloidal Dispersions," Solid/Liquid Dispersions, Edited by Th. Tadros, Academic Press, New York, NY., 1987.

Gui86 Guizard, C., N. Cygankiewicz, A. Labot, and L. Cot, "Sol-Gel Transition in Zirconia Systems Using Physical and Chemical Processes," J. Non-Cryst. Solids, 87, 86-91 (1986).

Gul80 Gulati, S.T., J.D. Helfinstine, and A.D. Davis, "Determination of Some Useful Properties of Partially Stabilized Zirconia and the Application to Extrusion Dies," J. Am. Ceram. Soc., 59[2] 211-19 (1980).

Gulb73 Gulbekian, E.V. and G.E.J. Reynolds, "Polyvinyl Alcohol in Emulsion Polymerization," Polyvinyl Alcohol Properties and Applications, Edited by C.A. Finch, John Wiley & Sons, Inc., London, 1973, pp. 427-460.

Gun89 Gunji, T., Y. Nagao, T. Misuno, and Y. Abe, "Preparation of SiO_2-TiO_2 Fibers From Polytitanosiloxanes," J. Non-Cryst. Solids, 107, 149-54 (1989).

Gup77 Gupta, T.K., J.H. Bechtold, R.C. Kuznickie, L.H. Cadoff, and B.R. Rossing, "Stabilization of Tetragonal Phase in Polycrystalline Zirconia," J. Mater. Sci. 12, 2421 (1977).

Han84 Handbook of Composites, Edited by G. Lubin, Van Nostrand Reinhold Co., New York, NY., 1984, pp. 225-226.

Heu87 Heuer, A.H., "Transformation Toughening in ZrO_2-Containing Ceramics," J. Am. Ceram. Soc., 70[10] 689-98 (1987).

Heue82 Heuer, A.H., N. Claussen, W.M. Kriven, and M. Rühle, "Stability of Tetragonal ZrO_2 Particles in Ceramic Matrices," J. Am. Ceram. Soc., 65[12] 642-50 (1982).

Hil65 Hillert, M., "On the Theory of Normal and Abnoraml Grain Growth," Acta Metall., 13[4] 227-38 (1965).

Hie86 Hiemenz, P.C., Principles of Colloid and Surface Chemistry, Marcel Dekker, Inc., New York, NY., 1986, pp. 169-222.

Hir87 Hiramatsu, T., T. Higuchi, and J. Matsui, ""Torayca" T1000 Ultra High Strength Fibre and Its Composite Properties," Looking Ahead for Materials and Processes, Materials Science Monographs, Vol. 41., Edited by J. DeBossu, G. Briens, and P. Lissac, Elsevier Science Publishers, Amsterdam, The Netherlands, 1987, pp. 1-8.

Hol87 Holtz, A.R. and M.F. Grether, "High Temperature Properties of Three Nextel Ceramic Fibers," presented at 32nd International SAMPE

Symposium and Exhibition at Anaheim Convention Center, April 6-9, 1987.

Hor85 Hori, S., R. Kurita, M. Yoshimura, and S. Somiya, "Suppressed Grain Growth in Final Stage Sintering of Al_2O_3 with Dispersed ZrO_2 Particles," J. Mater. Sci. Lett., 4, 1067-70 (1985).

Hou87 Hou, Y-Y., J-Q. Gao, and H-T. Zhang, "Effect of Al_2O_3 on Retaining Tetragonal Particles in Y-PSZ Ceramic Matrix," J. Mater. Sci. Lett., 6, 246-48 (1987).

Ile79 Iler, R.K., The Chemistry of Silica, John Wiley & Sons, Inc., New York, NY., 1979, pp. 232.

Jad87 Jada, S.S., "Surface Properties of Gel-Derived Zirconia Fibres," J. Mater. Sci., 6, 1368-70 (1987).

Joh87 Johnson, D.D., A.R. Holtz, and M.F. Grether, "Properties of Nextel 480 Ceramic Fibers," Ceram. Eng. Sci. Proc., 8[7-8] 744-54 (1987).

John85 Johnson, D.W., "Sol-Gel Processing of Ceramics and Glass," Am. Ceram. Soc. Bull., 64[12] 1597-1602 (1985).

Jon87 Jones, D.M., K. Walters, and P.R. Williams, "On the Extensional Viscosity of Mobile Polymer Solutions," Rheol. Acta, 26, 20-30 (1987).

Kag84 Kagawa, M., Y. Imamura, S. Usui, and Y. Syono, "Distribution of ZrO_2 and Al_2O_3 in Ultrafine ZrO_2-Al_2O_3 Powders Formed by the Spray-ICP Technique," J. Mater. Sci. Lett., 3, 699-702 (1984).

Kam80a Kamiya, K. and Sakka, S., "TiO_2-SiO_2 Glasses Prepared From Metal Alkoxides," J. Mater. Sci. Lett., 15, 2937-39 (1980).

Kam80b Kamiya, K., S. Sakka, and Y. Tatemichi, "Preparation of Glass Fibres of the ZrO_2-SiO_2 and Na_2O-ZrO_2-SiO_2 Systems From Metal Alkoxides and Their Resistance to Alkaline Solution," J. Mater. Sci., 15, 1765-71 (1980).

Kam86 Kayamia, K., K. Tanimoto, and T. Yoko, "Preparation of TiO_2 Fibres by Hydrolysis and Polycondensation of $Ti(O\text{-}i\text{-}C_3H_7)_4$," J. Mater. Sci. Lett., 5, 402-404 (1986).

Kar77 Karst, K.A. and H.G. Sowman, "Non-Frangible Alumina-Silica Fibers," U.S. Pat. No. 4,047,965, 1977.

Kay87 Kaysser, W. A., M. Sprissler, C.A. Handwerker, and J.E. Blendell, "Effect of a Liquid Phase on the Morphology of Grain Growth in Alumina," J. Am. Ceram. Soc., 70[5] 339-43 (1987).

Kee84 Keefer, K.D., "The Effect of Hydrolysis Conditions on the Structure and Growth of Silicate Polymers," Better Ceramics Through Chemistry, Mat. Res. Soc. Symp. Proc. Vol. 32, Edited by C.J. Brinker, D.E. Clark, and D.R. Ulrich, Elsevier Science Publishing Co., Inc., New York, NY., 1984, pp. 15-24.

Kha88 Khavari, M.E., F.F. Lange, P. Smith, and D.B. Marshall, "Continuous Spinning of Zirconia Fibers: Relations Between Processing and Strength," Better Ceramics Through Chemistry III, Mat. Res. Soc. Symp. Proc. vol. 121, Edited by C.J. Brinker, D.E. Clark, and D.R. Ulrich, Materials Research Society, Pittsburgh, PA., 1988, p. 617-621.

Kin59 Kingery, W.D., "Densification during Sintering in the Presence of a Liquid Phase. I. Theory," J. Appl. Phys., 30[3] 301-306 (1959).

Kin76 Kingery, W.D., H.K. Bowen, and D.R. Uhlmann, Introduction to Ceramics, John Wiley & Sons, New York, NY., 1976.

King59 Kingery, W.D., J. Pappis, M.E. Doty, and D.C. Hill, "Oxygen Ion Mobility in Cubic $Zr_{0.85}Ca_{0.15}O_{1.85}$," J. Am. Ceram. Soc., 42[8] 393-98 (1959).

Klu74 Klug, H.P. and L.E. Alexander, X-Ray Diffraction Procedures, 2nd ed., John Wiley & Sons, Inc., New York, NY., 1974.

Kok83 Kokubo, T., Y. Teranishi, and T. Maki, "Preparation of Amorphous ZrO_2 Fibers by Unidirectional Freezing of Gel," J. Mater. Sci., 56, 411-16 (1983).

Kok88 Kokubo, T., Y. Teranishi, T. Maki, and S. Sakka, "Formation of Zirconia fibres on Unidirectional Freezing of a Gel," J. Mater. Sci., 23, 1126-30 (1988).

Kos84 Kosmac, T, D. Kolar, and M. Trontelj, "Diffusion Processes and Solid-State Reactions in the Systems Al_2O_3-ZrO_2 (Stabilizing Oxide)(Y_2O_3, CaO, MgO)," Advances in Ceramics vol. 12, Science and Technology of Zirconia II, Edited by N. Claussen, M. Rühle, and A.H. Heuer, The American Ceramic Society, Columbus, OH., 1984, pp. 546-552.

Koz88 Kozuka, H., H. Kuroki, and S. Sakka, "Flow Characteristics and Spinnability of Sols Prepared from Silicon Alkoxide Solution," J. Non-Cryst. Solids., 100, 226-30 (1988).

Kri72 Krieger, I.M., "Rheology of Monodispersed Latices," Adv. Colloid Interface Sci., 3, 111-36 (1972).

Krie59 Krieger, I.M. and T.J. Dougherty, "Mechanism for non-Newtonian Flow in Suspensions of Rigid Spheres," Trans. Soc. Rheol., 3, 137-152, 1959.

Kuk73 Kuklina, V.N., "Phase Composition and Particle Size of Decomposition Products of Aluminum Nitrate Nanohydrate," Kinetics and Catalysis, 14 [3] 626 (1973).

LaC84 LaCourse, W.C., "Strength of Gel-Derived SiO_2 Fibers," Better Ceramics Through Chemistry, Mat. Res. Soc. Symp. Proc. vol. 32, Edited by C.J. Brinker, D.E. Clark, and D.R. Ulrich, Elsevier Science Publishing Co., Inc., New York, NY., 1984, pp. 53-58.

LaC88 LaCourse, W.C., "Continuous Filament Fibers by the Sol-Gel Process," Sol-Gel Technology for Thin Films, Fibers, Preforms, Electronics, and Specialty Shapes, Edited by L.C. Klein, Noyes Publications, Park Ridge, NJ., 1988, pp. 184-198.

LaCo86 LaCourse, W.C. and S. Kim, "Use of Mixed Titanium Alkoxides for Sol-Gel Processing," Science of Ceramic Chemical Processing, Edited by L.L. Hench and D.R. Ulrich, John Wiley & Sons, Inc., New York, NY., 1986, pp. 305-310.

Lan82a Lange, F.F., "Transformation Toughening, Part 1, Size Efects Associated with the Thermodynamics of Constrained Transformations," J. Mater. Sci., 17, 225-34 (1982).

Lan82b Lange, F.F., "Transformation Toughening, Part 3, Experimental Observations in the ZrO_2-Y_2O_3 System," J. Mater. Sci., 17, 240-246 (1982).

Lan87 Lange, F.F. and M.M. Hirlinger, "Grain Growth in Two-Phase Ceramics: Al_2O_3 Inclusions in ZrO_2," J. Am. Ceram. Soc., 70[11] 827-30 (1987).

Lang79 Lange, R.W. and H.G. Sowman, "Shaped and Fired Articles of TiO_2," U.S. Pat. No. 4,166,147, 1979.

Lei81 Leiser, D.B., M. Smith, and H.E. Goldstein, "Developments in Fibrous Refractory Composite Insulation," Am. Ceram. Soc. Bull., 60[11] 1201-204 (1981).

Ler84 Leroy, E., C. Robin-Brose, and J.P. Torre, "Fabrication of Zirconia Fibers From Sol-Gels," Ultrastructure Processing of Ceramics, Glasses, and Composites, Edited by L.L. Hench and D.R. Ulrich, John Wiley & Sons, Inc., New York, NY, 1984, pp. 219-31.

Lev75 Levin, E.M. and H.F. McMurdie, Figure 4370, Phase Diagrams for Ceramists, 1975 Supplement, The American Ceramic Society, Columbus, OH., 1975.

Levi64 Levin, E.M., C.R. Robbins, and H.F. McMurdie, Figure 2586, Phase Diagrams for Ceramists, Edited by M.K. Reser, The American Ceramic Society, Columbus, OH., 1964.

Liu80 Liu, L.G., "New High Pressure Phases of ZrO_2 and HfO_2," J. Phys. Chem. Solids, 41, 331-34 (1980).

Liv68 Livage, J., K. Doi, and C. Mazieres, "Nature and Thermal Evolution of Amorphous Hydrated Zirconium Oxide," J. Am. Ceram. Soc., 51[6] 349-53 (1968).

Mah87 Mah, T-I., M.G. Mendiratta, A.P. Katz, and K.S. Mazdiyasni, "Recent Developments in Fiber-Reinforced High Temperature Ceramic Composites," Am. Ceram. Soc. Bull., 66[2] 304-308 (1987).

Mahl80 Mahler, W. and M.F. Bechtold, "Freeze-Formed Silica Fibers," Nature, 285[1] May, 27-28 (1980).

Mahl84 Mahler, W. and U. Chowdhry, "Morphological Consequences of Freezing Gels," Ultrastructure Processing of Ceramics, Glasses, and Composites, Edited by L.L. Hench and D.R. Ulrich, John Wiley & Sons, Inc., New York, NY, 1984, pp. 207-217.

Mak86 Maki, T. and S. Sakka, "Formation of Alumina Fibers by Unidirectional Freezing of Gel," J. Non-Cryst. Solids, 82, 239-45 (1986).

Mak88 Maki, T. and S. Sakka, "Preparation of Alumina Fibers by Sol-Gel Method," J. Non-cryst. Solids, 100, 303-308 (1988).

Mar87 Marshall, D.B., F.F. Lange, and P.D. Morgan, "High Strength Zirconia Fibers," J. Am. Ceram. Soc., 70[8] C-187-C-188 (1987).

Marv38 Marvel, C.S. and C.E. Denoon, Jr., "The Structure of Vinyl Polymers. II. Polyvinyl Alcohol," J. Am. Chem. Soc., 60, 1045-51 (1938).

Mas80 Masuda, Y. and R. Watanabe, "Ostwald Ripening Processes," Sintering Process, Materials Science Reseach vol. 13, Edited by G.C. Kuczynski, Plenum Press, New York, NY., 1980, pp. 3-21.

Mat84 Matsui, M., T. Soma, and I. Oda, "Effect of Microstructure on the Strength of Y-TZP Components," Advances in Ceramics vol. 12, Science and Technology of Zirconia II, Edited by N. Claussen, M. Rühle, and A.H. Heuer, The American Ceramic Society, Columbus, OH., 1984, pp. 371-81.

McC88 McCrum, N.G., C.P. Buckley, and C.B. Bucknall, Principles of Polymer Engineering, Oxford University Press, Oxford, 1988, pp. 268-272.

Mec87 Mecartney, M.L, "Influence of an Amorphous Second Phase on the Properties of Yttria-Stabilized Tetragonal Zirconia Polycrystals (Y-TZP)," J. Am. Ceram. Soc., 70[1] 54-58 (1987).

Meh88 Mehrotra, R.C., "Polymetallic Alkoxides-Precursors for Ceramics," in Better Ceramics Through Chemistry III, Mat. Res. Soc. Symp. Proc. Vol. 121, Edited by C.J. Brinker, D.E. Clark, and D.R. Ulrich, Materials Research Society, Pittsburgh, PA., 1988, pp. 81-92.

Men69 Mendelson, M.I., "Average Grain Size in Polycrystalline Ceramics," J. Am. Ceram. Soc., 52[8] 443-46 (1969).

Mil89 Miller, K.T. and F.F. Lange ,"The Morphological Stability of Polycrystalline Fibers," Acta Metall., 37[5] 1343-47 (1989).

Mill84 Miller, W.C., "Refractory Fibers," Handbook of Composites, Edited by G. Lubin, Van Nostrand Reinhold Co., New York, NY., 1984, pp. 1069-81.

Mit74 Mitsuhashi, T., M. Ichihara, and U. Tatsuke, "Characterization and Stabilization of Metastable Tetragonal ZrO_2," J. Am. Ceram. Soc., 57[2] 97-101 (1974).

Mor87 Morley, J.G., High-Performance Fibre Composites, Academic Press, New York, NY., 1987, pp. 21-88.

Morr84 Morrissey, H.J., K.K., Czanderna, C.B. Carter, and R.P. Merrill, "Growth of α-Al_2O_3 Within a Transition Alumina Matrix," J. Am. Ceram. Soc., 67[5] C-88-C-90 (1984).

Mul58 Mullins, W.W., "The Effect of Thermal Grooving on Grain Boundary Motion," Acta Met., 6, 414-27 (1958).

Mur86 Murase, Y., E. Kato, and K. Daimon, "Stability of ZrO_2 Phases in Ultrafine ZrO_2-Al_2O_3 Mixtures," J. Am. Ceram. Soc., 69[2] 83-87 (1986).

Nak70 Nakamoto, K., Infrared Spectra of Inorganic and Coordination Compounds, John Wiley & Sons, Inc., New York, NY., 1970.

Nap77 Napper, D.H., "Steric Stabilization," J. Colloid Interface Sci., 58[2] 390-407 (1977).

Nic66 Nichols, F.A., "Theory of Grain Growth in Porous Compacts," J. Appl. Phys., 37[13] 4599-602 (1966).

Nor73 Noro, K., "Hydrolysis of Polyvinyl Acetate to Polyvinyl Alcohol," Polyvinyl Alcohol Properties and Applications, Edited by C.A. Finch, John Wiley & Sons, Inc., London, 1973, pp. 91-120.

Ose85 Osendi, M.I., J.S. Moya, C.J. Serna, and J. Soria, "Metastability of Tetragonal Zirconia Powders," J. Am. Ceram. Soc., 68[3] 135-39 (1985).

Ove52 Overbeek, J.Th.G., "The Interaction Between Colloidal Particles," Colloidal Science, Edited by H.R. Kruyt, Elsevier, Amsterdam, 1952, pp. 245-271.

Pap89 Papet, P., N. Le Bars, J.F. Baumard, A. Lecomte, and A. Dauger, "Transparent Monolithic Zirconia Gels: Effects of Acetylacetone Content on Gelation," J. Mater. Sci., 24, 3850-54 (1989).

Pen85 Pena, P., P. Miranzo, J.S. Moya, and S. De Aza, "Multicomponent Toughened Ceramic Materials Obtained by Reaction Sintering Part 1 ZrO_2-Al_2O_3-CaO System," J. Mater. Sci., 20[6] 2011-22 (1985).

Pet79 Petrie, C.J.S., Elongational Flows, Pitman, London, 1979.

Pug86 Pugar, E.A. and P.E.D. Morgan, "Coupled Grain Growth Effects in Al_2O_3/10 vol% ZrO_2," J. Am. Ceram. Soc., 69[6] C-12-C-123 (1986).

Pys89 Pysher, D.J., K. C. Goretta, R. S. Hodder, Jr., and R. E. Tressler, "Strengths of Ceramic Fibers at Elevated Temperatures," J. Am. Ceram. Soc., 72[2] 284-88 (1989).

Rad79 Radford, K.C. and R. J. Bratton, "Zirconia Electrolyte Cells part Sintering Studies," J. Mater. Sci., 14, 59-65 (1979).

Ray78 Ray, N.H., Inorganic Polymers, Academic Press, New York, NY., 1978, pp. 145-154.

Ree73 Reed-Hill, R.E., Physical Metallurgy Principles, 2nd ed., D. Van Nostrand Co., New York, NY., 1973, pp. 315-316.

Rho66 Rhodes, W.H. and R.E. Carter, "Cationic Self-Diffusion in Calcia-Stabilized Zirconia," J. Am. Ceram. Soc., 49[5] 244-49 (1966).

Ric84 Rice, R.W., J.R. Span, D. Lewis, and W. Coblenz, "The Effect of Ceramic Fiber Coatings on the Room Temperature Mechanical Behavior of Ceramic-Fiber Composites," Ceram. Eng. Sci. Proc., 5[7-8] 614-24 (1984).

Rie76 Rieth, P.H., J.S. Reed, and A.W. Naumann, "Fabrication and Flexural Strength of Ultra-Fine Grained Yttrai-Stabilized Zirconia," Bull. Am. Ceram. Soc., 55, 717 (1976).

Rij70 Rijnten, H.Th., "Formation, Preparation and Properties of Hydrous Zirconia," Physical and Chemical Aspects of Adsorbents and Catalysts, Edited by B.G. Linsen, Academic Press, New York, NY., 1970, pp. 315-372.

Rom87 Romine, J.C., "New High-Temperature Ceramic Fiber," Ceram. Eng. Sci. Proc., 8[7-8] 755-65 (1987).

Ros72 Ross. S.D., Inorganic Infrared and Raman Spectra, McGraw-Hill, London, 1972, pp. 166-168.

Ruh84 Ruh, R., K.S. Mazdiyasni, P.G. Valentine, and H.O. Bielitein, "Phase Relations in the System ZrO_2-Y_2O_3 at Low Y_2O_3 Contents," J. Am. Ceram. Soc., 67[9] C-190-C-192 (1984).

Rüh84 Rühle, M., N. Claussen, and A.H.Heuer, "Microstructural Studies of Y_2O_3-Containing Tetragonal ZrO_2 Polycrystals (Y-TZP)," Advances in Ceramics vol. 12, Science and Technology of Zirconia II, Edited by N. Claussen, M. Rühle, and A.H. Heuer, The American Ceramic Society, Columbus, OH., 1984, pp. 352-370.

Rut62 Rutgers, R., "Relative Viscosity and Concentration," Rheol. Acta, 2, 305-348 (1962).

Sac86 Sacks, M.D. and R. S. Sheu, "Rheological Characterization During the Sol-Gel Transition," Science of Ceramic Chemical Processing, Edited by L. L. Hench and D. R. Ulrich, John Wiley & Sons, Inc., New York, NY., 1986, pp. 100-107.

Sak88 Sakka, S., "Fibers From the Sol-Gel Process," Sol-Gel Technology for Thin Films, Fibers, Preforms, Electronics, and Specialty Shapes, Ed. by L.C. Klein, Noyes Publications, Park Ridge, NJ., 1988, pp. 140-161.

Sakk82 Sakka, S. and K. Kamiya, "The Sol-Gel Transition in the Hydrolysis of Metal Alkoxides in Relation to the Formation of Glasses, Fibers and Films," J. Non-cryst. Solids, 48, 31-46 (1982).

Sakka88 Sakka, S. and H. Kozuka, "Rheology of Sols and Fiber Drawing," J. Non-Cryst. Solids., 100, 142-53 (1988).

Saw87 Sawyer, L.C., M.Jamieson, D.Brikowski, M.I.Haider, and R.T.Chen, "Strength, Structure, and Fracture Properties of Ceramic Fibers Produced from Polymeric Precursors: I, Base-Line Studies," J. Am. Ceram. Soc., 70[11] 798-810 (1987).

Sch84 Schubert, H., N. Claussen, and M. Rühle, "Preparation of Y_2O_3-Stabilized Tetragonal ZrO_2 Polycrystals (Y-TZP) from Different Powders," Advances in Ceramics vol. 12, Science and Technology of Zirconia II, Edited by N. Claussen, M. Rühle, and A.H. Heuer, The American Ceramic Society, Columbus, OH., 1984, pp. 766-773.

Sci86 Science of Ceramic Chemical Processing, Edited by L.L. Hench and D.R. Ulrich, John Wiley & Sons, Inc., New York, NY., 1986.

Sco75 Scott, H.G., "Phase Relationships in the Zirconia-Yttria System," J. Mater. Sci., 10, 1527-35 (1975).

Seu74 Seufert, L.E., "Alumina Fiber," U.S. Pat. No. 3,808,015, 1974.

Sha87 Shaw, T.M., "Which Grain Boundaries are Penetrated by Liquid?," Am. Ceram. Soc. Bull., 66[3] 514 (1987).

Sil81 Silverstein, R.M., G.C. Bassler, and T.C. Morrill, Spectrometric Identification of Organic Compounds, John Wiley & Sons, Inc., New York, NY., 1981, pp. 120-121.

Sis80 Sisler, H.H., R.D. Dresdner, and W.T. Mooney, Jr., Chemistry: A Systematic Approach, Oxford University Press, Oxford, 1980, pp. 667-674.

Smi48 Smith, C.S., Trans. AIME, 175, 15 (1948).

Sow85 Sowman, H.G. and D.D. Johnson, "Ceramic Oxide Fibers," Ceram. Eng. Sci. Proc., 6[9-10] 1221-30 (1985).

Sow88a Sowman, H.G., "A New Era in Ceramic Fibers via Sol-Gel Technology," Am. Ceram. Soc. Bull., 67[12] 1911-16 (1988).

Sow88b Sowman, H.G., "Alumina-Boria-Silica Ceramic Fibers from the Sol-Gel Process," in Sol-Gel Technology for Thin Films, Fibers, Preforms, Electronics, and Specialty Shapes, Edited by L.C. Klein, Noyes Publications, Park Ridge, NJ., 1988, pp. 162-183.

Sta88 Stacey, M.H., "Developments in Continuous Alumina-Based Fibres," Br. Ceram. Trans. J., 87, 168-72 (1988).

Ste86 Stevens, R., An Introduction to Zirconia, Magnesium Elektron Ltd., Twickenham, UK., 1986, pp. 37.

Stu78 Stubican, V.S., R.C. Hink, and S.P. Ray, "Phase Equilibria and Ordering in the System ZrO_2-Y_2O_3," J. Am. Ceram. Soc., 61[1-2] 17-21 (1978).

Sum83 "Sumitomo's Alumina Fiber," Sumitomo Chemical Company, Ltd., Data Sheet, Osaka, Japan, 1983.

Tan88 Tanner, R.I., Engineering Rheology, Clarendon Press, Oxford, 1988.

Tie63 Tien, T.Y. and E.C. Subbarao, "Grain Growth in $Ca_{0.16}Zr_{0.84}O_{1.84}$," J. Am. Ceram. Soc., 46[10] 489-92 (1963).

Tor84 Torralvo, M.J., M.A. Alario, and J. Soria, "The Glow Phenomenon in Zirconium Oxide," J. Catal., 86, 473-76 (1984).

Toy73 Toyoshima, K., "General Properties of Polyvinyl Alcohol in Relation to its Applications," Polyvinyl Alcohol Properties and Applications, Edited by C.A. Finch, John Wiley & Sons, London, 1973, pp. 17-65.

Tsu84 Tsukuma, K., Y. Kubota, and T. Tsukidate, "Thermal and Mechanical Properties of Y_2O_3-Stabilized Tetragonal Zirconia Polycrystals," Advances in Ceramics vol. 12, Science and Technology of Zirconia II, Edited by N.

Claussen, M. Rühle, and A.H. Heuer, The American Ceramic Society, Columbus, OH., 1984, pp. 382-390.

Tsu87 Tsukuma, K. and T. Takahata, "Mechanical Property and Microstructure of TZP and TZP/Al_2O_3 Composites," Advanced Structural Ceramics, Edited by P.F. Becher, M.W. Swain, and S. Somiya, Materials Research Society, Pittsburgh, PA., 1987, pp. 123-35.

Tsuk85 Tsukuma, K., K. Ueda, K. Matsushita, and M.Shimada, "High-Temperature Strength and Fracture Toughness of Y_2O_3-Partially-Stabilized ZrO_2/Al_2O_3 Composites," J. Am. Ceram. Soc., 68[2] C-56-C-58 (1985).

Uhl84 Uhlmann, D.R., B.J.J. Zelinski, and G.E. Wnek, "The Ceramist as Chemist - Opportunities for New Materials," Better Ceramics Through Chemistry, Mat. Res. Soc. Symp. Proc. Vol. 32, Edited by C.J. Brinker, D.E. Clark, and D.R. Ulrich, Elsevier Science Publishing Co., Inc., New York, NY., 1984, pp. 59-70.

Ult84 Ultrastructure Processing of Ceramics, Glass, and Composites, Edited by L.L. Hench and D.R. Ulrich, John Wiley & Sons, Inc., New York, NY., 1984.

Ult88 Ultrastructure Processing of Advanced Ceramics, Edited by J.D. Mackenzie and D.R. Ulrich, John Wiley & Sons, Inc., New York, NY., 1988.

Van84 Vander Voort, G.F., Metallography Principles and Practice, McGraw-Hill Co., New York, NY., 1984.

van85 van de Graaf, M.A.C.G., J.H.H. Ter Maat, and A.J. Burggraaf, "Microstructure and Sintering Kinectics of Highly Reactive ZrO_2-Y_2O_3 Ceramics," J. Mater. Sci., 20, 1407-18 (1985).

vanO77 van Olphen, H., An Introduction to Clay Colloid Chemistry, John Wiley & Sons, Inc., New York, NY., 1977, pp. 1-2.

Wai65 Wainer, E., B.C. Raynes, and A.L. Cunningham, "Liquid Polymers, Solid Articles Made Therefrom, and Methods of Preparing Same," U.S. Pat. No. 3,180,741, 1965.

Wha87 Whalen, P.J., F. Reidinger, S.T. Correale, and J. Marti, "Yttria Migration in Y-TZP During High-Temperature Annealing," J. Mater. Sci., 22, 4465-69 (1987).

Wol63 Wolten, G.M., "Diffusionless Phase Transformation in Zirconia and Hafnia," J. Am. Ceram. Soc., 46[9] 418-22 (1963).

Wu84 Wu, S., E. Gilbart, and R.J. Brook, "Soild-State Sintering: The Attainment of High Density," Advances in Ceramics, vol. 10, Structure and Properties of MgO and Al_2O_3 Ceramics, , Edited by W.D. Kingery, The American Ceramic Society, Inc., Columbus, OH., 1984, pp. 574-582.

Yer84 Yermolenko, I.N., T.M. Ulyanova, P.A. Vityaz, and I.L. Fyodorova, "Synthesis and Sintering of ZrO_2 Fibers," Advances in Ceramics vol. 12, Science and Technology of Zirconia II, Edited by N. Claussen, M. Rühle, and A.H. Heuer, The American Ceramic Society, Columbus, OH., 1984, pp. 826-832.

Yol75 Yoldas, B.E., "Alumina Sol Preparation from Alkoxides," Am. Ceram. Soc. Bull., 54, 289-90 (1975).

Yol82 Yoldas, B.E., "Effect of Variations in Polymerized Oxides on Sintering and Crystalline Transformations," J. Am. Ceram. Soc., 65[8] 387-93 (1982).

Zar82 Zarzycki, J., M. Prassas, and J. Phalippou, "Synthesis of Glasses From Gels: The Problem of Monolithic Gels," J. Mater. Sci., 17, 3371-79 (1982).

Zia67 Ziabicki, A., "Physical Fundamentals of the Fiber-Spinning Processes," Man-Made Fibers Science and Technology vol. 1, Edited by H.F. Mark, S.M. Atlas, and E. Cernia, Interscience Publishers, John Wiley & Sons, Inc., New York, NY., 1967, pp. 13-94.

BIOGRAPHICAL SKETCH

Soo-Man Sim was born on March 8, 1953, in Pusan, Korea. He and his wife Kwang-Ja Kim Sim have one child, Minjin.

After graduating from Kyungnam High School in Pusan, he attended Seoul National University where he was awarded a Bachelor of Science in ceramic engineering in February, 1980. During a his college career, he served in the army for three years. He joined the Department of Materials Science and Engineering at The Pennsylvania State University with a Korean Government Scholarship and received a Master of Science in the Ceramic Science Section in 1984. Since that time, he has been enrolled as a doctoral candidate in materials science and engineering at the University of Florida.

He is a member of the American Ceramic Society, Sigma Xi and Keramos.

I certify that I have read this study and that in my opinion it conforms to acceptable standards of scholarly presentation and is fully adequate, in scope and quality, as a dissertation for the degree of Doctor of Philosophy.

David E. Clark, Chair
Professor of Materials Science and Engineering

I certify that I have read this study and that in my opinion it conforms to acceptable standards of scholarly presentation and is fully adequate, in scope and quality, as a dissertation for the degree of Doctor of Philosophy.

Robert T. DeHoff
Professor of Materials Science and Engineering

I certify that I have read this study and that in my opinion it conforms to acceptable standards of scholarly presentation and is fully adequate, in scope and quality, as a dissertation for the degree of Doctor of Philosophy.

Joseph H. Simmons
Professor of Materials Science and Engineering

I certify that I have read this study and that in my opinion it conforms to acceptable standards of scholarly presentation and is fully adequate, in scope and quality, as a dissertation for the degree of Doctor of Philosophy.

Ellsworth Dow Whitney
Professor of Materials Science and Engineering

I certify that I have read this study and that in my opinion it conforms to acceptable standards of scholarly presentation and is fully adequate, in scope and quality, as a dissertation for the degree of Doctor of Philosophy.

James M. Boncella
Assistant Professor of Chemistry

This dissertation was submitted to the Graduate Faculty of the College of Engineering and to the Graduate School and was accepted as partial fulfillment of the requirements for the degree of Doctor of Philosophy.

December 1990

for Winfred M. Phillips
Dean, College of Engineering

Madelyn M. Lockhart
Dean, Graduate School